Wind Energ. Sci., 9, 555–583, 2024
https://doi.org/10.5194/wes-9-555-2024

eawe european academy of wind energy
Open Access WIND ENERGY SCIENCE

Seasonal variability of wake impacts on US mid-Atlantic offshore wind plant power production

David Rosencrans[1,2], Julie K. Lundquist[1,2,3], Mike Optis[2,4], Alex Rybchuk[2], Nicola Bodini[2], and Michael Rossol[2]

[1]Department of Atmospheric and Oceanic Sciences, University of Colorado, Boulder, CO 80303, USA
[2]National Renewable Energy Laboratory, Golden, CO 80401, USA
[3]Renewable and Sustainable Energy Institute, Boulder, CO 80303, USA
[4]Veer Renewables, Courtenay, V9N 9B4, Canada

Correspondence: David Rosencrans [redacted]@colorado.edu)

Received: 7 April 2023 – Discussion started: 4 May 2023
Revised: 23 January 2024 – Accepted: 1 February 2024 – Published: 14 March 2024

Abstract. The mid-Atlantic will experience rapid wind plant development due to its promising wind resource located near large population centers. Wind turbines and wind plants create wakes, or regions of reduced wind speed, that may negatively affect downwind turbines and plants. We evaluate wake variability and annual energy production with the first yearlong modeling assessment using the Weather Research and Forecasting model, deploying 12 MW turbines across the domain at a density of 3.14 MW km^{-2}, matching the planned density of 3 MW km^{-2}. Using a series of simulations with no wind plants, one wind plant, and complete build-out of lease areas, we calculate wake effects and distinguish the effect of wakes generated internally within one plant from those generated externally between plants. We also provide a first step towards uncertainty quantification by testing the amount of added turbulence kinetic energy (TKE) by 0 % and 100 %. We provide a sensitivity analysis by additionally comparing 25 % and 50 % for a short case study period. The strongest wakes, propagating 55 km, occur in summertime stable stratification, just when New England's grid demand peaks in summer. The seasonal variability of wakes in this offshore region is much stronger than the diurnal variability of wakes. Overall, yearlong simulated wake impacts reduce power output by a range between 38.2 % and 34.1 % (for 0 %–100 % added TKE). Internal wakes cause greater yearlong power losses, from 29.2 % to 25.7 %, compared to external wakes, from 14.7 % to 13.4 %. The overall impact is different from the linear sum of internal wakes and external wakes due to non-linear processes. Additional simulations quantify wake uncertainty by modifying the added amount of turbulent kinetic energy from wind turbines, introducing power output variability of 3.8 %. Finally, we compare annual energy production to New England grid demand and find that the lease areas can supply 58.8 % to 61.2 % of annual load. We note that the results of this assessment are not intended to make nor are they suitable to make commercial judgments about specific wind projects.

1 Introduction

The US offshore wind industry is flourishing, with a target capacity of 30 GW by 2030 (FACT SHEET, 2023). New England features the highest population density in the United States and commensurate utility usage, making offshore wind an attractive regional electricity source. A total of 27 active lease areas now span the mid-Atlantic Outer Continental Shelf (OCS). The OCS features low turbulence (Bodini et al., 2019) and fast winds, with 100 m winds averaging 10 m s^{-1} (Musial et al., 2016). Consequently, large wind plants will be constructed to harness the ample wind resource.

Meteorological conditions and construction challenges constrain siting options for large wind plants. Because the average wind direction is southwesterly (Bodini et al., 2019), a southwest-to-northeast wind plant orientation mitigates ex-

ternal waking from neighboring plants. Further, preserving efficient vessel transit, upholding common fishery practices, and prioritizing safe Coast Guard search-and-rescue operations necessitate 1×1 nm corridors (W.F. Baird & Associates, 2019). Considering these constraints, wind plants will be densely packed into clusters.

Densely packed clusters produce wakes that adversely affect downwind turbines (Nygaard, 2014; Platis et al., 2018; Lundquist et al., 2019; Schneemann et al., 2020). Wakes are plumes downwind of turbines with slower wind speeds and increased turbulence. Mid-Atlantic wakes induced by large wind plants could impose wind speed deficits up to $2\,\mathrm{m\,s^{-1}}$ (Pryor et al., 2021; Golbazi et al., 2022). Wind speed deficits can be replenished by wake recovery in which turbulence entrains momentum from aloft into the waked zone (Stevens et al., 2016; Gupta and Baidya Roy, 2021). However, stably stratified conditions suppress mixing for wake recovery (Fitch et al., 2013; Vanderwende et al., 2016; Porté-Agel et al., 2020). Under certain conditions, mid-Atlantic wakes could propagate 100 km or more (Pryor et al., 2021; Golbazi et al., 2022; Stoelinga et al., 2022).

Wake characteristics have been evaluated using physics-based models of varying complexity. High-fidelity methods include computational fluid dynamics models solving Reynolds-averaged Navier–Stokes equations (Antonini et al., 2020); large-eddy simulations resolving the turbine rotor as an actuator disk (Mirocha et al., 2014; Aitken et al., 2014; Shapiro et al., 2019; Arthur et al., 2020); and mesoscale models parameterizing a hub-height momentum sink, sometimes including a turbulence source (Fitch et al., 2013; Volker et al., 2015; Archer et al., 2020; Gupta and Baidya Roy, 2021), as reviewed by Fischereit et al. (2022). Pryor et al. (2021) characterized mid-Atlantic wake impacts using mesoscale modeling of 55 simulation days. They examined modified wind plant layouts of 15 MW turbines under different flow scenarios, considering power densities between 2.1 and $4.34\,\mathrm{MW\,km^{-2}}$. Stoelinga et al. (2022) estimated wake impacts using 15 MW turbines and 16 simulation days under typical southwesterly flow. Golbazi et al. (2022) considered summertime wakes with three scales of turbines to consider surface impacts. Finally, Rybchuk et al. (2022) addressed the sensitivity to wake characteristics under idealized conditions by varying planetary boundary layer (PBL) schemes.

In this work, we assess intra-plant and inter-plant wakes throughout the mid-Atlantic OCS using a yearlong mesoscale modeling study. The results of this assessment are not intended to make nor are they suitable to make commercial judgments about specific wind projects. The simulations use the Weather Research and Forecasting (WRF) model version 4.2.1 (Skamarock et al., 2019). One set of simulations runs with no wind farms (NWF) as a control, validated with lidar measurements, while the others use the Fitch wind farm parameterization (WFP) (Fitch et al., 2012, with updates described by Archer et al., 2020) to incorporate turbine effects. Our simulations incorporate 12 MW turbines and a power density of $3.14\,\mathrm{MW\,km^{-2}}$. Simulations employ different wind plant layouts, including one representative lease area alone (ONE) within the Rhode Island–Massachusetts (RIMA) block, all lease areas (LA), and the lease areas plus the call areas (CA), to assess different waking scenarios (Table 1). WFP simulations run separately by added turbulent kinetic energy (TKE) amount, including 0 % added TKE (TKE_0) and 100 % added TKE (TKE_100) to quantify the full range of uncertainty. NWF, ONE, and LA simulations run from 1 September 2019 to 1 September 2020 to capture a full year with available lidar measurement data. Due to computational costs, CA simulations focus on the summertime stable period from 1 September to 31 October 2019 and 1 July to 31 August 2020 (Table 1). This time period highlights wake impacts during months with presumed frequent stable stratification and high electricity demands (Livingston and Lundquist, 2020) as a worst-case scenario.

The remainder of this article is structured as follows. Section 2 introduces the model setup and configuration, model validation, and the analysis methods. Section 3 discusses variability in stratification, wakes, and power production. Section 4 concludes the work and offers recommendations for future work.

2 Methods

2.1 WRF modeling setup

We assess the effects of wakes and power production across the mid-Atlantic OCS using numerical weather prediction simulations with WRF version 4.2.1 and the WFP (Fitch et al., 2012). Version 4.2.1 allows for modifying the amount of TKE produced by wind turbines and ensures turbulence advection (Archer et al., 2020). Two nested domains comprise 6 and 2 km horizontal resolutions (Pronk et al., 2022; Xia et al., 2022; Bodini et al., 2023; Redfern et al., 2023), respectively, and the inner nest begins 20 grid cells into the parent domain (Fig. 1). This same domain and period of study have been used to explore interactions between power production and sea breezes (Xia et al., 2022). Fine vertical resolution (10 m) near the surface stretches aloft, with 17 levels within the lowest 200 m as recommended by Tomaszewski and Lundquist (2020). We choose an 18 s time step in the outer domain, 54 vertical levels, a 5000 Pa top, simple diffusion, and damping 6000 m below the model top to prevent gravity wave reflection. Hourly 30 km initial and boundary conditions are provided by the European Centre for Medium-Range Weather Forecasts (ECMWF) fifth-generation reanalysis (ERA5) data set (Hersbach et al., 2020). Sea surface temperature is provided by the UK Met Office Operational Sea Surface Temperature and Sea Ice Analysis (OSTIA) data set (Donlon et al., 2012). We choose the Noah land surface model (Niu et al., 2011), the Mellor–Yamada–Nakanishi and Niino level 2.5 PBL and surface layer (Nakanishi and Niino, 2006), new Thompson microphysics (Thompson et al.,

Table 1. Summary of WRF simulations.

Simulation type	Abbreviation	Turbine type	Period	Added TKE amount	No. of turbines
No wind farms	NWF	n/a	Sep 2019–Sep 2020	n/a	0
One wind farm only	ONE	12 MW	Sep 2019–Sep 2020	0 % and 100 %	177
Lease areas	LA	12 MW	Sep 2019–Sep 2020	0 % and 100 %	1418
Call areas	CA	12 MW	Sep 2019–Nov 2019 Jul 2020–Sep 2020	100 %	3219

n/a: not applicable

2008), and the rapid radiative transfer model longwave and shortwave radiative transfer (Iacono et al., 2008) schemes. The Kain–Fritsch cumulus scheme parameterizes cloud microphysics in the outer domain only (Kain, 2004).

2.2 Wind turbine layouts

Wind turbines are sited within lease areas offshore of the US East Coast (Fig. 1) as defined by the Bureau of Ocean Energy Management (Bureau of Ocean Energy Management, 2023). Following realistic deployment strategies, we site individual turbines 1 nm, or 8.6 rotor diameters, apart and an additional 0.5 nm from lease area boundaries (W.F. Baird & Associates, 2019; Beiter et al., 2020; Walter Musial, personal communication, September 2020). This layout provides a power density of 3.14 MW km^{-2}. Lower power densities in US waters reflect wake concerns in Europe and the need to increase turbine spacing for wake replenishment. Areas that had already been approved for development are denoted as the lease areas. Areas where competitive interest was yet to be determined are denoted as the call areas. Both lease areas and call areas are filled to spatial capacity with turbines (Fig. 1), recognizing renewable energy targets (218th Legislature, 2018).

2.3 Wind turbine characteristics

For our simulations, we parameterize 12 MW turbines which are scaled by Beiter et al. (2020) from a 15 MW reference turbine with a 138 m hub height and 215 m rotor diameter. The power and thrust coefficient curves were held constant from the 15 MW machine. The rotor diameter was scaled to maintain a specific power of 332 W m^{-2}, which is the same as the reference 15 MW turbine. Then, the hub height was determined such that a 30 m gap was maintained between the lower bound of the rotor tip and the sea surface. No power is produced in region 1 of the power curve, from 0 m s^{-1} to cut-in wind speed (3 m s^{-1}). In region 2 of the power curve, power production increases between cut-in wind speed and rated speed (11 m s^{-1}). In region 3, between rated and cut-out wind speed (30 m s^{-1}), an increase in wind speed no longer yields additional power production (Beiter et al., 2020) (Fig. 2a).

2.4 Wind farm parameterization

We use the WFP (Fitch et al., 2012) to incorporate the effects of wind turbines on the 2 km grid. Horizontal wind speed reduction from turbine drag (Eq. 1), power production (Eq. 2), and turbulence generation (Fitch et al., 2012; Archer et al., 2020) (Eq. 3) are calculated in the WFP from the following:

$$\frac{\delta |V|_{ijk}}{\delta t} = -\frac{N_{ij} C_{\mathrm{T}}\left(|V|_{ijk}\right) |V|_{ijk}^{2} A_{ijk}}{2(z_{k+1} - z_k)}, \tag{1}$$

$$\frac{\delta P_{ijk}}{\delta t} = \frac{N_{ij} C_{\mathrm{P}}\left(|V|_{ijk}\right) |V|_{ijk}^{3} A_{ijk}}{2(z_{k+1} - z_k)}, \tag{2}$$

$$\frac{\delta \mathrm{TKE}_{ijk}}{\delta t} = \frac{N_{ij} C_{\mathrm{TKE}}\left(|V|_{ijk}\right) |V|_{ijk}^{3} A_{ijk}}{2(z_{k+1} - z_k)}, \tag{3}$$

where i, j, and k represent Cartesian model coordinates; $C_{\mathrm{T}}\left(|V|_{ijk}\right)$ is the wind-speed-dependent thrust coefficient; $|V|$ is the wind speed at turbine hub height; ρ is the air density; A_{ijk} is the rotor-swept area; N_{ij} is the number density of turbines in grid cell ij; $C_{\mathrm{P}}\left(|V|_{ijk}\right)$ is the wind-speed-dependent power coefficient; z_k is the height of vertical model level k; and C_{TKE} is the fraction of energy converted to TKE (Fitch et al., 2012). These values are calculated at each model level, as the use of a rotor-equivalent wind speed generally exerts a minor effect (Redfern et al., 2019).

The thrust and power coefficients (C_{T} and C_{P}, respectively) vary with wind speed as defined by wind turbine manufacturers (Fig. 2b). The thrust coefficient C_{T} is the non-dimensionalized thrust force exerted by wind on the rotor-swept plane (Burton et al., 2011).

The power coefficient, C_{P}, governs the fraction of rotor kinetic energy converted into electrical power. This conversion is not perfectly efficient due to electrical and mechanical losses (Fitch et al., 2012; Archer et al., 2020). The leftover fraction of energy (Eq. 4) from the difference between C_{T} and C_{p} is transformed into turbulence, C_{TKE}.

$$C_{\mathrm{TKE}} = C_{\mathrm{T}} - C_{\mathrm{P}} \tag{4}$$

Because electromechanical losses are not represented by the WFP, all leftover energy converts to TKE, so the TKE may be overestimated (Fitch et al., 2012; Archer et al., 2020). Some

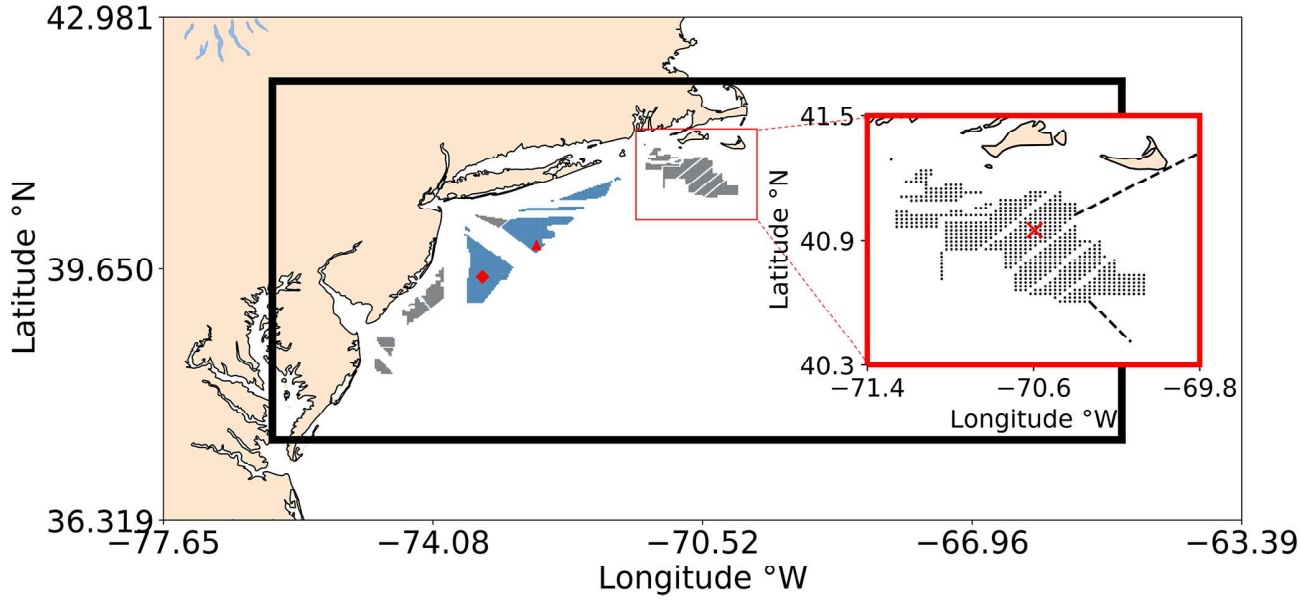

Figure 1. Simulation Domain 1 includes the entire region, and Simulation Domain 2 is outlined by the black rectangle. Each dot represents a wind turbine. Wind energy lease areas are shown in gray and call areas in blue. The red square zooms in on the Rhode Island–Massachusetts block of lease areas. The E05 (triangle) and E06 (diamond) floating lidars are shown in red. Atmospheric stratification is assessed at the red X. Wake propagation distances are assessed along the dashed black lines.

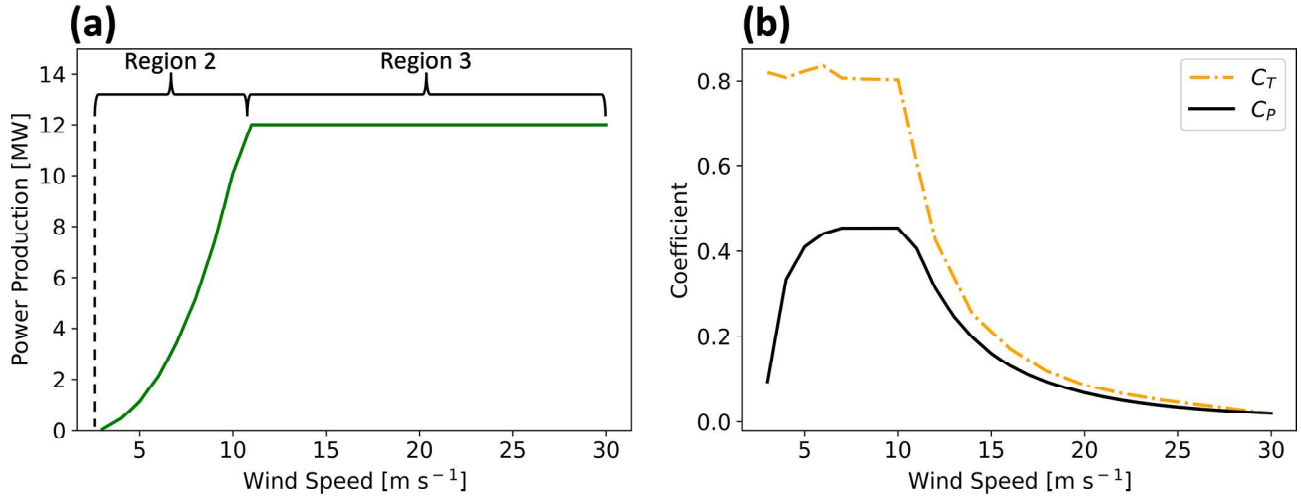

Figure 2. Characteristics of the 12 MW scaled turbine used herein. **(a)** The power curve and **(b)** curves showing the thrust coefficients (C_T; dashed orange) and the power coefficients (C_P; solid black) with wind speed across the x axis.

researchers suggest this TKE term is unnecessary (Volker et al., 2015), although comparisons to large-eddy simulations (Vanderwende et al., 2016) and observations (Siedersleben et al., 2020) suggest the turbine-produced TKE is critical to include. Any overestimation of TKE would enhance turbulent mixing, thereby exaggerating turbulent transport of momentum that causes wake recovery and overestimating power production. Therefore, Archer et al. (2020) propose reducing C_{TKE} to 25 %. For these simulations, we bound this uncertainty by carrying out simulations with 100 % and 0 % added TKE (Fig. A1). TKE advection is turned on.

2.5 Observations

We compared the NWF simulation to observations of offshore wind profiles. Two buoy-mounted meteorological ocean observing systems, denoted E05 and E06, are located within the Hudson North and Hudson South call areas of the New York Bight (Fig. 3). Each buoy system samples line-of-

sight boundary layer wind speed and wind direction using the ZephIR ZX300M light detection and ranging (lidar) instrument. The lidars are mounted 2 m above the sea surface and take measurements at 20 m intervals up to 200 m, providing 10 min averages of wind speed and direction, which the New York State Energy Research and Development Authority (NYSERDA) has made publicly available (DNV, 2019). We use floating lidar data to validate simulations for 1 September 2019 to 1 September 2020.

2.6 Stability classification

Different methods can be used to identify stratification, or atmospheric stability. Stable stratification can occur in coastal regions when warm air advects over a cooler sea surface, thereby suppressing buoyancy and turbulent mixing. Likewise, unstable stratification can occur when cool air advects over a warmer sea surface. Some observations suggest more frequent unstable stratification, based on the Obukhov length (Archer et al., 2016). The sign of the Obukhov length depends on the sign of heat flux and can be a useful metric for determining stability conditions. Other observations suggest that minimal turbulence and strong veer can be characteristic of stable conditions (Bodini et al., 2019). Wind veer increases in stable stratification as the influence of buoyant-turbulence-induced friction decreases. Thus, winds turn to approach quasi-geostrophic flow at a quicker rate, which can be further exaggerated by the presence of a low-level jet.

We calculate the Obukhov length (Monin and Obukhov, 1954) (L), representative of the height at which buoyant production of turbulence first dominates mechanical shear production of turbulence:

$$L = -\frac{u_*^3 \overline{\theta_\mathrm{v}}}{\kappa g \left(\overline{w'\theta_\mathrm{v}'}\right)}, \tag{5}$$

where u_* is the friction velocity (UST from WRF output), θ_v is the virtual potential temperature, κ is the von Karman constant of 0.4, g is gravitational acceleration, and $\overline{w'\theta_\mathrm{v}'}$ is the vertical turbulent heat flux (HFX from WRF output). Lengths between 0 and −500 m are characterized as unstable stratification, and lengths between 0 and 500 m are categorized as stable stratification (Muñoz-Esparza et al., 2012). Lengths approaching negative or positive infinity are neutral. Each timestamp from the NWF run is assigned a stability for the 1 September 2019 to 1 September 2020 period at a grid point centered on the RIMA block (Fig. 1).

2.7 Model validation

We validate the NWF model by comparing wind speed estimated by the turbine-free simulations with observations from E05 and E06 lidars. Model output is obtained from the grid cells containing the lidars in 20 m intervals from 60 to 200 m following Pronk et al. (2022). Wind speeds and directions are compared using a suite of metrics recommended by Optis et al. (2020) for wind resource assessment, including the correlation coefficient (r), centered root-mean-square error (cRMSE), and bias:

$$r = \frac{\sum_i^N (V_{\mathrm{W}_i} - \overline{V_\mathrm{W}})(V_{\mathrm{L}_i} - \overline{V_\mathrm{L}})}{N \sigma_\mathrm{W} \sigma_\mathrm{L}}, \tag{6}$$

$$\mathrm{cRMSE} = \sqrt{\frac{\sum_i^N \left(\left(V_{\mathrm{W}_i} - \overline{V_\mathrm{W}}\right) - \left(V_{\mathrm{L}_i} - \overline{V_\mathrm{L}}\right)\right)^2}{N}}, \tag{7}$$

$$\mathrm{Bias} = \frac{\sum_i^N \left(V_{\mathrm{W}_i} - V_{\mathrm{L}_i}\right)}{N}, \tag{8}$$

where V is the wind speed, N is the total number of values, σ is the standard deviation, and subscripts "W" and "L" indicate WRF and lidar, respectively. Earth mover's distance (EMD), or the Wasserstein metric, is calculated with a SciPy function (Virtanen et al., 2020) as in other wind resource evaluations (Hahmann et al., 2020). Each of these metrics provides different insights into the performance of the model. For instance, the correlation coefficient illuminates how well the model captures the timing of weather systems and diurnal variability. EMD emphasizes the difference between distributions but not the timing. Bias captures the difference between measured and modeled values. Finally, cRMSE describes the random component of error.

The circularity of wind direction must be accounted for in statistical calculations. For example, computing the average between 359 and 1°, using a typical arithmetic mean, would result in 180°. However, the mean wind direction between those two values should be 360°. The SciPy (Virtanen et al., 2020) and Astropy (Price-Whelan et al., 2022) Python packages offer convenient functions which allow the user to calculate statistics for a circular variable by passing in the lower and upper bounds, in this case 0 and 360°. We calculate the mean and standard deviation of wind direction using the SciPy circmean and circstd functions, respectively, and the correlation coefficient using the Astropy circcorrcoef function. The cRMSE for wind direction is then calculated following

$$\mathrm{cRMSE} = \sqrt{\mathrm{circmean}\left(180° - \left|\left|\left(D_{\mathrm{W}_i} - \overline{D_\mathrm{W}}\right) - \left(D_{\mathrm{L}_i} - \overline{D_\mathrm{L}}\right)\right| - 180°\right|\right)^2}, \tag{9}$$

where D is wind direction, and $\overline{D}$ is the circular mean of wind direction. Bias is calculated similarly to Eq. (8), except that differences between NWF and lidar values that are less than −180° have 360° added and differences greater than 180° have 360° subtracted:

$$x = \begin{cases} x + 360° & \text{for } x < -180° \\ x - 360° & \text{for } x > 180° \end{cases}, \tag{10}$$

where x is the $(D_{\mathrm{WRF}_i} - D_{\mathrm{Lidar}_i})$ difference.

Time stamps in which the lidar returns NaN values are removed from WRF data sets during comparison (Table 2). Doing so removes 8.1 % of wind speed data at 140 m at E05,

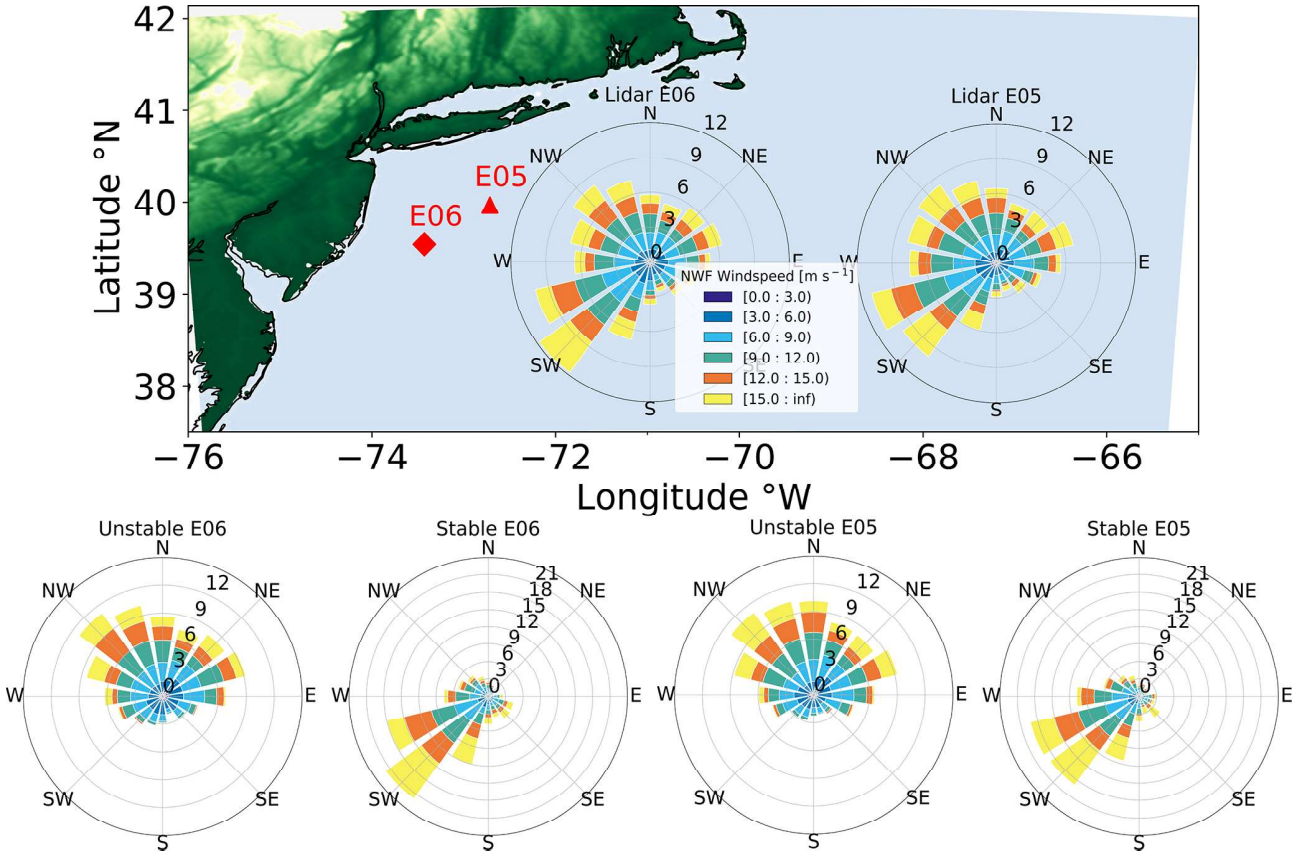

Figure 3. Hub-height wind roses for the NYSERDA Hudson North (E05) and Hudson South (E06) floating lidars during the 1 September 2019 to 1 September 2020 period. The location of E06 is shown as the red diamond and E05 as the red triangle. The bottom row shows wind roses segregated by atmospheric stratification.

Table 2. Percentage of data removed at 140 m due to not-a-number (NaN) values.

	Unstable	Stable	Neutral
E05	1.35 %	6.44 %	0.33 %
E06	3.64 %	9.48 %	0.62 %

made up by 1.22 %, 5.76 %, and 1.13 % in unstable, stable, and neutral stratification, respectively. Similarly, 13.7 % of wind speed data are removed at E06 and are made up by 3.20 %, 9.38 %, and 1.15 % in unstable, stable, and neutral stratification, respectively. An r^2 value of 1 indicates a perfect correlation between NWF and lidar values. A value of 0 for cRMSE indicates that all values, with model bias removed, lie on the 1 : 1 regression line. A cRMSE value greater than 0 indicates the distance of residual points from the regression line. Negative biases indicate an underestimation from WRF, while positive biases indicate overestimation. A value of 0 for EMD indicates that probability density functions from each data source are equivalent. A positive EMD indicates that the NWF wind speed distribution must shift towards lower values to match the lidar distribution.

NWF wind speed profiles are compared with lidar observations for the 1 September 2019 to 1 September 2020 period to assess model skill (Fig. 4). Note that Pronk et al. (2022) provide validation metrics against the E05 lidar profile during the same period of study and find similar results. Negative biases (Eq. 8) increase in magnitude with height between 0 and $-0.5\,\mathrm{m\,s^{-1}}$ (Fig. 4a), showing the model underestimates the wind speed. Strengths of variation (Eq. 6) among WRF output and the lidars range between 0.82 and 0.86 (Fig. 4b). Centered RMSE (Eq. 7) increases with height around $2\,\mathrm{m\,s^{-1}}$ (Fig. 4c). Finally, EMD values originate around $0.2\,\mathrm{m\,s^{-1}}$ at 60 m and increase with height (Fig. 4d). Comparing lidars E05 and E06, WRF performs better at E06 with a smaller bias by $0.04\,\mathrm{m\,s^{-1}}$, lower cRMSE by $0.08\,\mathrm{m\,s^{-1}}$, better correlation by 0.003, and smaller EMD by $0.05\,\mathrm{m\,s^{-1}}$.

We further assess the NWF performance, partitioned by stability conditions. In unstable stratification, WRF wind speeds have a negative bias that gradually increases in magnitude with height from $-0.5\,\mathrm{m\,s^{-1}}$ at 60 m (Fig. 5a). In sta-

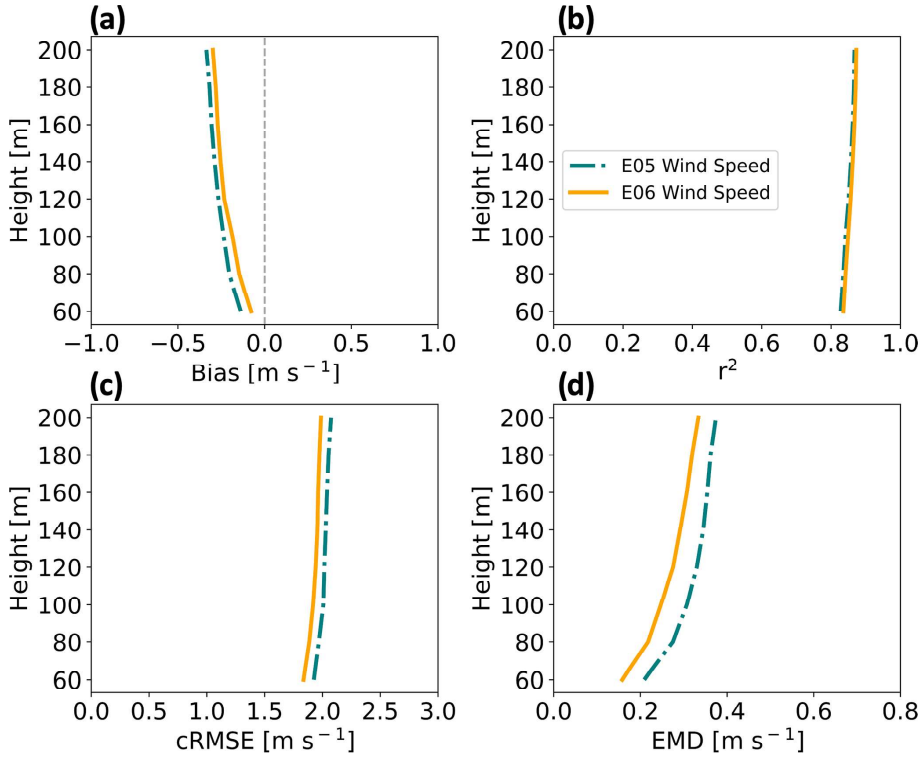

Figure 4. Vertical profiles for wind speed comparative metrics at the E05 (teal) and E06 (orange) lidars from 1 September 2019 to 1 September 2020. Shown are **(a)** bias, **(b)** correlation, **(c)** cRMSE, and **(d)** EMD.

ble conditions, WRF overestimates wind speeds by roughly 0.4 m s^{-1} at 60 m with biases approaching 0.0 m s^{-1} further aloft (Fig. 5a). In neutral conditions, WRF overestimates wind speeds by up to 0.3 m s^{-1} near the surface and underestimates wind speeds further aloft. Comparing between mean E05 and E06 profiles, WRF performs better at the E06 lidar location by 0.08 m s^{-1} in unstable conditions, 0.04 m s^{-1} in stable conditions, and 0.1 m s^{-1} in neutral conditions.

NWF and lidar wind speeds correlate well. Correlation remains the largest in unstable conditions for all heights (Fig. 5b). The worst strength of relationship occurs in stable stratification, although there is improvement aloft, and by 160 m, correlation between stable and neutral conditions is largely equivalent (Fig. 5b). On average, WRF performance between lidar locations is the same in unstable and stable conditions and better at E06 by 0.02 in neutral conditions.

Centered RMSE profiles change with stratification. In unstable conditions, cRMSE increases somewhat with height originating from greater than 1.5 m s^{-1} at 60 m (Fig. 5c). In stable stratification, the cRMSE profile begins at roughly 2.3 m s^{-1} at 60 m and increases with height. In neutral conditions, cRMSE increases with height from around 2 m s^{-1}. As before, WRF performs better at E06. On average, cRMSE is lower at E06 by 0.1 m s^{-1} in unstable conditions, by a negligible amount in stable conditions, and by 0.1 m s^{-1} in neutral conditions.

Earth mover's distance has more variability with height. It is the largest in unstable stratification, increasing with height from roughly 0.5 m s^{-1} at 60 m (Fig. 5d). In stable conditions, EMD decreases with height and originates at around 0.35 m s^{-1} at 60 m. In neutral stratification, EMD decreases with height from about 0.2 m s^{-1}. On average, WRF performs better at E06 by 0.07 m s^{-1} in unstable conditions, by 0.04 m s^{-1} in stable conditions, and by 0.06 m s^{-1} in neutral conditions.

Next, we show metrics to compare WRF output wind direction profiles with lidar measurements. Bias is negative, or counterclockwise, at both E05 and E06 lidar locations. NWF output resolves wind directions better at E06 with a mean bias of −7.8° with height as compared to −11.1° at E05 (Fig. 6a). Correlation coefficients at both locations are strong, at 0.83 and 0.82 for E06 and E05, respectively (Fig. 6b). Mean cRMSE (Eq. 9) is similar between lidar locations, at 5.9 and 6.2° for E06 and E05, respectively (Fig. 6c). Finally, EMD is lower at E06, increasing with height with an average of 3.3° (Fig. 6d). EMD is larger at E05, increasing with height with an average of 4.8° (Fig. 6d). Overall, WRF performs better at E06 with lower absolute bias by 3.3°, lower RMSE by 0.3°, higher correlation by 0.01, and lower EMD by 1.48°.

We use the same metrics to validate WRF against lidar-reported wind directions by stratification and begin with bias

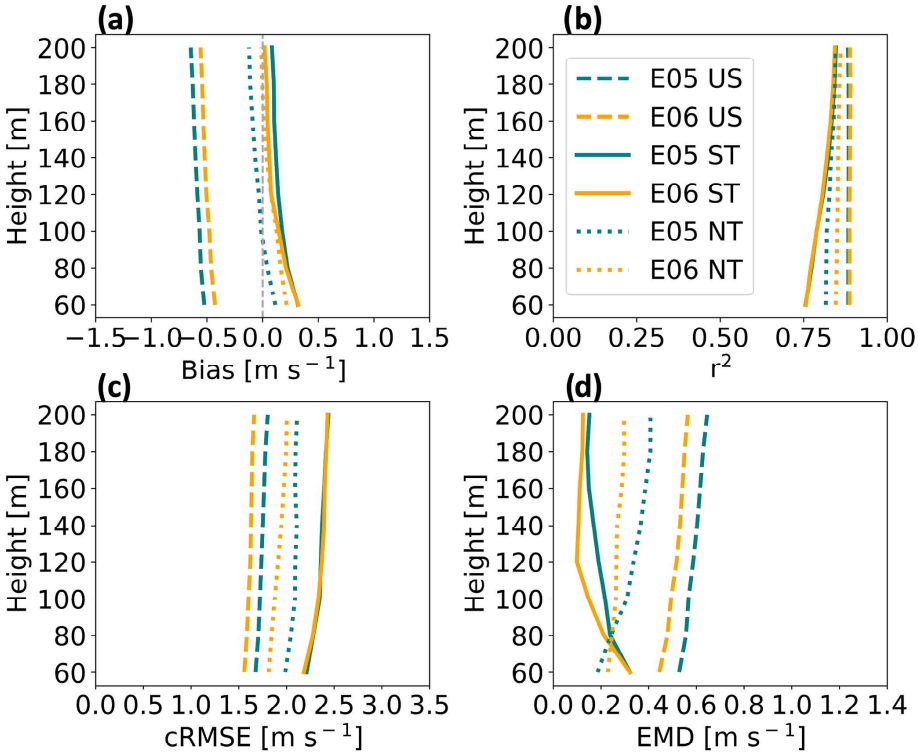

Figure 5. Vertical profiles for wind speed comparative metrics at the E05 (teal) and E06 (orange) lidar locations subset by stratification (US – unstable, ST – stable, NT – neutral) from 1 September 2019 to 1 September 2020. Shown are **(a)** bias, **(b)** correlation, **(c)** cRMSE, and **(d)** EMD.

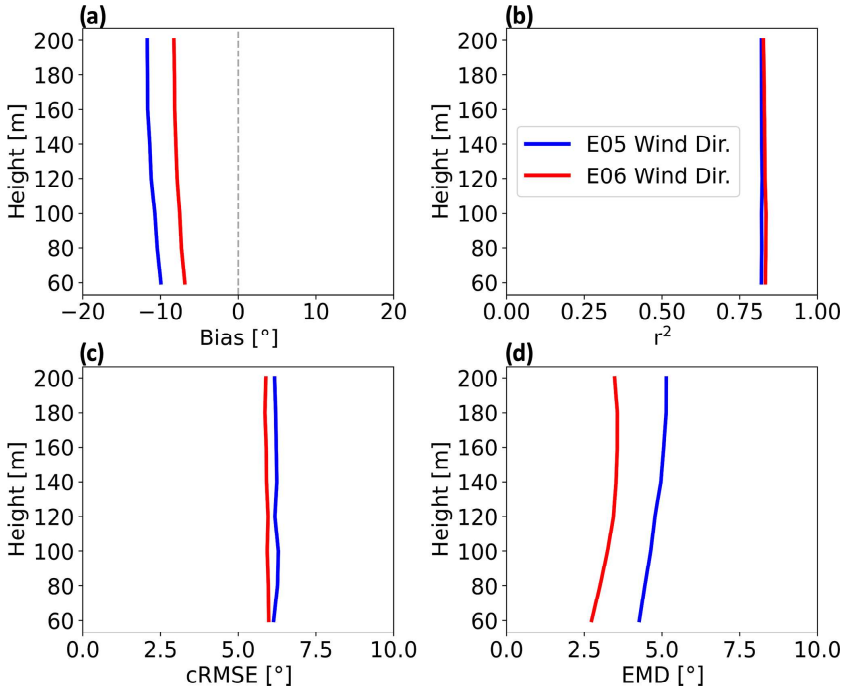

Figure 6. Vertical profiles for wind direction comparative metrics at the E05 (blue) and E06 (red) lidar locations from 1 September 2019 to 1 September 2020. Shown are **(a)** bias, **(b)** correlation, **(c)** cRMSE, and **(d)** EMD.

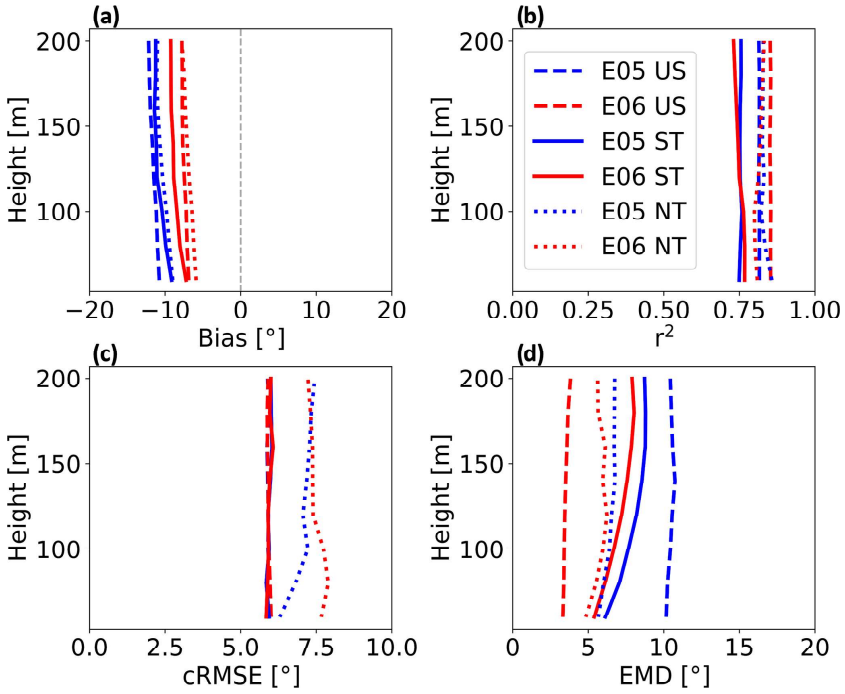

Figure 7. Vertical profiles for wind direction comparative metrics at the E05 (blue) and E06 (red) lidar locations subset by stratification (US – unstable, ST – stable, NT – neutral) from 1 September 2019 to 1 September 2020. Shown are **(a)** bias, **(b)** correlation, **(c)** cRMSE, and **(d)** EMD.

(Fig. 7a). In unstable conditions, mean biases are −7.4° at E06 and −11.5° at E05. In stable stratification, bias profiles are more similar between lidar locations, reaching −8.6° at E06 and −10.7° at E05. Bias is the smallest in neutral conditions at both locations, with mean values of −6.8° at E06 and −10.2° at E05. Overall, WRF performs better at the E06 lidar location by 4.1° in unstable conditions and by 2.0° in stable conditions and better at the E05 lidar location by 3.4° in neutral conditions.

The correlation between WRF-derived lidar-measured wind directions is strong in all stability conditions at both lidar locations (Fig. 7b). The strength of relation in unstable conditions is 0.85 at E06 and 0.81 at E05. In stable conditions, the mean correlation is 0.75 at both E06 and E05. In neutral conditions, the strengths of relation are 0.81 at E06 and 0.83 at E05. Overall, WRF performs better at E06 by 0.03° in unstable conditions and by 0.003° in stable conditions and better at E05 by 0.01° in neutral conditions.

Profiles for cRMSE are similar in unstable and stable conditions, with worse performance in neutral conditions (Fig. 7c). In both unstable and stable conditions, mean cRMSE is 5.9° at both E05 and E06. In neutral conditions, mean cRMSE is 7.5° at E06 and 7.0° at E05. WRF performs the same at both lidar locations in unstable and stable conditions and is better at E05 by 0.4° in neutral conditions.

Large variability exists for EMD between lidar locations in WRF (Fig. 7d). Unstable stratification features the largest spread between lidar locations, with EMD values of 3.5° at E06 and 10.4° at E05. In stable conditions, EMD is 7.0° at E06 and 7.9° at E05. In neutral stratification, mean EMD values are 5.7° at E06 and 6.4° at E05. On average, WRF performs the best at the E06 lidar location: 6.9° in unstable conditions, 0.8° in stable conditions, and 0.7° in neutral conditions.

Wind speed time series are collected and averaged for the full yearlong period from the grid cells housing lidars E05 and E06 in NWF and from the lidar measurements. The shear exponent is calculated as

$$a = \frac{\log(V_2) - \log(V_1)}{\log(z_2) - \log(z_1)}, \tag{11}$$

where V_1 and V_2 are the mean wind speeds at heights z_1 and z_2, respectively. We hold V_1 and z_1 constant at a reference height of 60 m and substitute V_2 and z_2 with values from 80 to 200 m at 20 m intervals.

Wind speed shear exponents (Eq. 11) differ between NWF and the lidar measurements. The average exponents from lidars E05 and E06 are 0.117 and 0.122, respectively, and are in good agreement with the annual average of 0.12 for both measured and modeled results in the mid-Atlantic (Viselli et al., 2018). The average exponents from WRF at grid cells housing E05 and E06 are 0.099 and 0.106, respectively. NWF-derived exponents correctly capture a decrease with height and lower coefficients at the E05 lidar. However, the exponents are smaller than those calculated from lidar measurements by −0.018 and −0.016 at E05 and E06, respec-

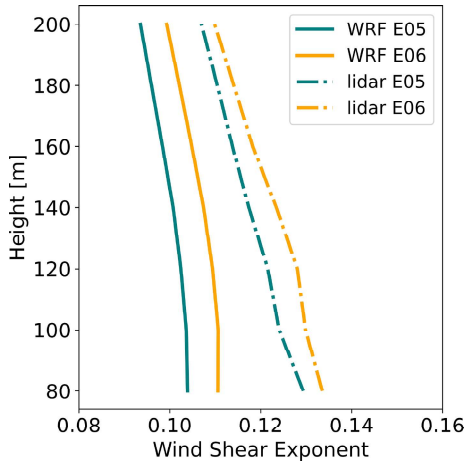

Figure 8. Mean wind speed shear exponent by height from NWF (solid) and from lidar measurements (dashed) from 1 September 2019 to 1 September 2020. E05 is shown in blue, and E06 is shown in orange.

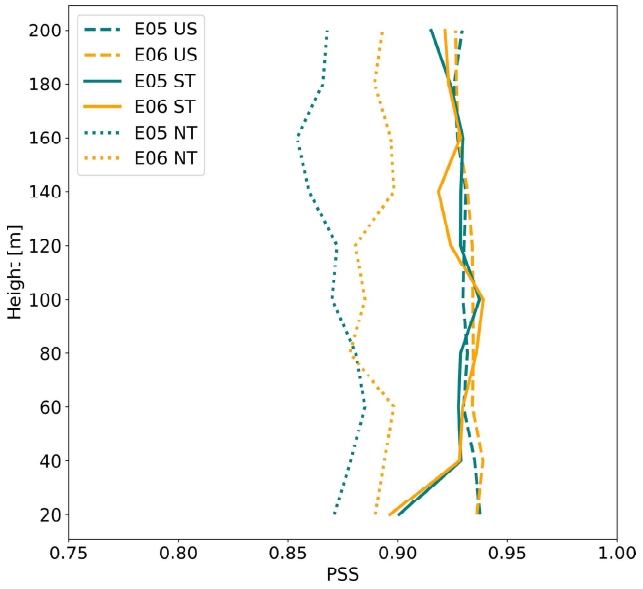

Figure 9. Vertical profiles of the Perkins skill score by stratification at the E05 (teal) and E06 (orange) lidars subset by stratification (US – unstable, ST – stable, NT – neutral).

tively. Smaller exponents in NWF may result from overestimated mixing or misrepresentation of wave-induced roughness.

We calculate profiles of the Perkins skill score (PSS) (Perkins et al., 2007) between NWF and lidar wind speeds. Wind speeds are considered at 20 m height intervals from 20 to 200 m. Each wind speed time series is subset by all time stamps with unstable, stable, and neutral stratification. After subsetting, time stamps where lidar observations return NaN are removed from both lidar and NWF time series. At each height, the probability distribution functions of wind speeds are binned at 0.2 m s^{-1} intervals and normalized such that the frequencies add to unity. The minimum frequency between modeled and observed values for each bin is stored, and the resulting stored values are summed to calculate the following score:

$$\mathrm{PSS} = \sum_{i=1}^{n} \min\left(C_{\mathrm{W}}(z), C_{\mathrm{L}}(z)\right), \tag{12}$$

where n is the number of bins, C is the count of normalized values in a bin, and z is the height. A PSS of 1.0 suggests perfect overlap of the two distributions.

Profiles of PSS (Eq. 12) between NWF and lidar observations of wind speed vary by location and stratification. Performance is generally best in unstable conditions at both E05 and E06 lidar locations with a mean value of 0.93. Performance is the second best in stable conditions, starting around 0.90 at the surface and increasing to 0.93 at 120 m at E05. At E06 in stable conditions, PSS reaches a maximum value of 0.93 at 100 m. Neutral conditions exhibit worse PSS and larger spread by location. AT E05, PSS minimizes at 0.85 at 160 m and maximizes around 0.88 at 60 m. At E06, PSS scores minimize at 0.87 at 80 m and maximize at 0.89 at 140 m.

2.8 Wake identification

The wake delineates the region downwind of turbines with a velocity deficit and turbulence enhancement. We identify the wind speed wake deficit by subtracting NWF wind speeds from WFP wind speeds at the hub height. Averaging across all times during the 1 September 2019 to 1 September 2020 period identifies the overall mean wake wind speed. Because wakes typically propagate to the northeast during stable conditions (Fig. 3), we calculate the propagation distance of wakes along a line extending northeast of the RIMA block (Fig. 1) and report the distance along the line where wake wind speeds reach a threshold. In unstable conditions the prevailing wind direction is northwesterly (Fig. 3), so we assess the wake propagation distance to the southeast instead. The threshold of -0.5 m s^{-1} is chosen following Golbazi et al. (2022) and Rybchuk et al. (2022). Finally, we define the areal extent of wakes as the area with a wind speed deficit less than -0.5 m s^{-1}.

2.9 Grid balancing

We compare model output energy production to New England grid demand. Demand data are provided hourly (NEISO, 2019). For comparison, we compute hourly averages of WFP power production from each set of simulations. We compare those averages to the national energy supply by acquiring the total from the U.S. Energy Information Administration (EIA, 2023).

2.10 Power variability

Assessing power variability is essential for addressing temporally changing grid demands. We assess the differences in electricity generation for each deployment scenario by separately collecting power output from grid cells containing wind turbines from ONE, LA, and CA simulations. Power is summed across grid cells containing turbines and averaged at 1, 7, and 30 d intervals for comparison. We address seasonal and diurnal variability by further separating and averaging power production totals at each time step into bins by month and hour of day. Power losses from the total, internal, and external wake effects are calculated from the following:

$$\mathrm{Loss_{tot}} = 100\,\% - \left(\frac{P_{\mathrm{LA,CA}}}{P_{\mathrm{NWF}}}\right) \times 100\,\%, \tag{13}$$

$$\mathrm{Loss_{int}} = 100\,\% - \left(\frac{P_{\mathrm{ONE}}}{P_{\mathrm{NWF}}}\right) \times 100\,\%, \tag{14}$$

$$\mathrm{Loss_{ext}} = 100\,\% - \left(\frac{P_{\mathrm{LA,CA}}}{P_{\mathrm{ONE}}}\right) \times 100\,\%, \tag{15}$$

$$\mathrm{Loss_{ext}} = \mathrm{Loss_{tot}} - \mathrm{Loss_{int}}, \tag{16}$$

where $P_{\mathrm{LA,CA}}$ is the power production at ONE grid cells in the presence of wakes by either the LA or the CA, P_{ONE} is the power production in the presence of internal wakes from ONE, and P_{NWF} is the power production from coupling hub-height wind speeds to the power curve. These methods are performed separately by added TKE amount. We note that the upwind conditions change in a LA or CA scenario due to external wakes, which can modify the internal losses in the numerator of Eq. (15). Thus, we provide an alternative method for calculating the external power losses as the difference between the total losses and the internal losses in Eq. (16).

Cluster-induced power deficits at ONE occur due to external wakes from the upwind lease and call areas. Power output from ONE, LA, and CA simulations are averaged in hourly windows at grid cells containing ONE turbines to reduce the effects of numerical noise (Appendix F). The resulting power averages from LA and CA simulations are divided by the averages from ONE at each time stamp. The hour of day and month of year categorize each time stamp, and percentages are placed into bins accordingly. Within each bin the percentages are averaged. Only power production totals greater than 9.9 MW are considered when calculating power losses. This threshold represents the power production total when all turbines within ONE begin operating at the cut-in wind speed. For reference, the total power production for ONE at rated power is 2124 MW. This method is repeated separately for TKE_0 and TKE_100 runs.

Individual wind turbines generate internal wakes within the ONE plant that adversely affect power production. To quantify internal wake effects at ONE, we collect NWF wind speeds at the hub height in each cell containing ONE turbines. Wind speeds are convolved with the power curve and scaled by the number of turbines per cell at 0.01 m s^{-1} intervals. This method returns the amount of power that ONE would produce in the absence of wakes. Hourly power averages are obtained from both NWF and ONE runs and considered only if power production exceeds 9.9 MW. ONE power totals are divided by the NWF power estimations from the power curve. Again, each time stamp is categorized by hour of day and month of year, and percentages are binned for averaging. These steps are repeated for both TKE_0 and TKE_100 runs.

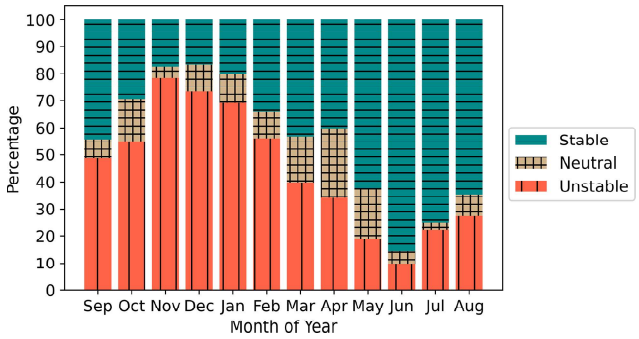

Figure 10. Stability classification using the Obukhov length for the 1 September 2019 to 1 September 2020 period at the RIMA block from NWF. The tan crosshatch represents neutral stratification, teal horizontal lines are stable stratification, and red vertical lines are unstable stratification.

3 Results

3.1 Year-round NWF stratification

The predominance of NWF stability conditions changes throughout the year (Figs. 10, 11) as assessed using the Obukhov length (Eq. 5) centered on the RIMA block.

The winter features predominant unstable stratification, whereas the summer features frequent stable stratification (Bodini et al., 2019; Optis et al., 2020) (Figs. 10, 11). The strong stability in summer is caused by nearby surface-heated air advecting over the colder OCS. These dynamics reverse during winter when cold air from land advects over warmer water. Overall, stratification is most frequently unstable during November and stable during June. April features the greatest percentage of neutral conditions as the springtime transition from cooler to warmer air reduces the air–sea temperature gradient. The same pattern occurs elsewhere throughout the OCS because diurnal variability in stratification is weaker than the seasonal cycle (Fig. 11). The mean unstable, stable, and neutral percentages of occurrence at the RIMA block are 44.3 %, 44.4 %, and 11.2 %, respectively, for the 1 September 2019 to 1 September 2020 period. Stability calculations from the model grid cells that house lidars E05 and E06 reveal similar results (Fig. B1). However, L may not always represent conditions aloft (Fig. C1).

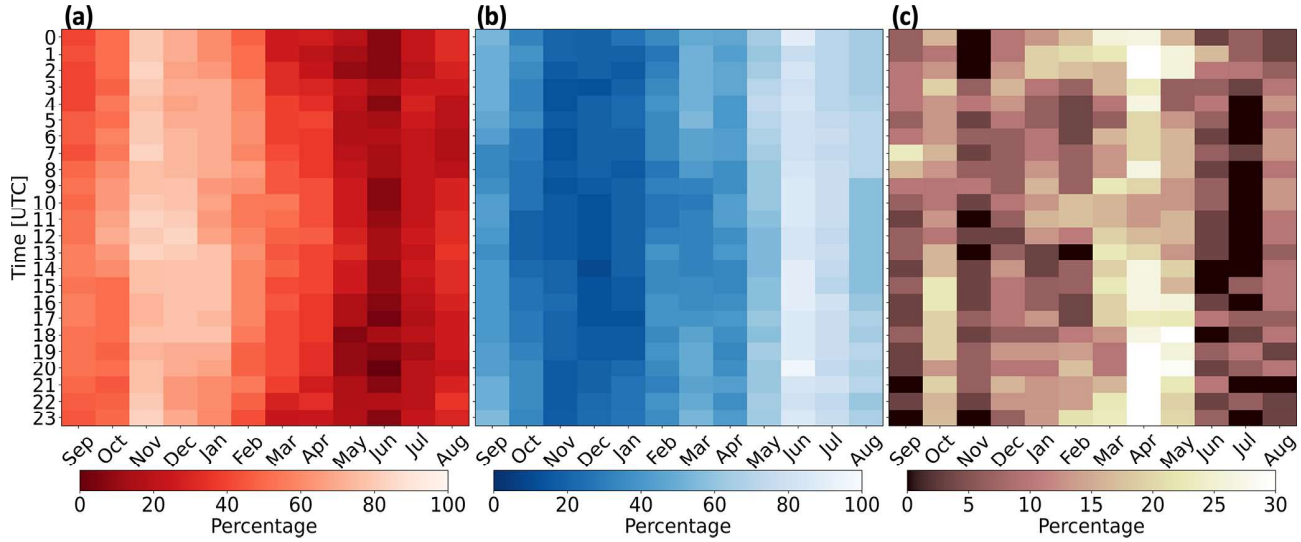

Figure 11. Percentages of occurrence for **(a)** unstable stratification, **(b)** stable stratification, and **(c)** neutral stratification from 1 September 2019 to 1 September 2020.

3.2 Wake variability

Here, we categorize wakes by the maximum wind speed deficit in space, the spatial extent, and the downwind propagation distance. While wakes remain relatively unchanged between TKE_0 and TKE_100, they drastically vary by stratification. The maximum average wake wind speed deficit occurs within the wind plant areas and intensifies from -1.5 to $-2.8\,\mathrm{m\,s^{-1}}$, moving from unstable to stable conditions for TKE_100 (Fig. 12a, c). Normalized with mean NWF hub-height wind speeds of $9.2\,\mathrm{m\,s^{-1}}$ (unstable) and $11.2\,\mathrm{m\,s^{-1}}$ (stable), the corresponding mean wind speed deficits are 16 % and 25 %. Similarly, the maximum average wind speed deficit intensifies from -1.8 to $-3.1\,\mathrm{m\,s^{-1}}$, a normalized reduction of 19 % and 27 %, moving from unstable to stable at TKE_0 (Fig. 12b, d). Thus, reducing TKE from 100 % to 0 % has a smaller impact on wake strength than increasing stability.

The areal extent of wakes changes by stability and added TKE. Wake deficits stronger than the $-0.5\,\mathrm{m\,s^{-1}}$ cutoff in unstable stratification at TKE_100 (Fig. 12a) cover a total area of $7208\,\mathrm{km^2}$ and represent the best-case scenario where wakes impact the smallest area. In stable stratification at TKE_100 (Fig. 12c), wakes cover a larger area of $15\,948\,\mathrm{km^2}$, or 2.2 times larger. A similar increase occurs using TKE_0, although areal coverage of the wake is larger due to weaker turbulence-induced wind speed replenishment from aloft. At TKE_0 in unstable conditions (Fig. 12b), wakes stronger than $-0.5\,\mathrm{m\,s^{-1}}$ cover an area of $7780\,\mathrm{km^2}$. In stable stratification, the area increases to $15\,636\,\mathrm{km^2}$ (Fig. 12d), a factor of 2. The spatial extent of strong wakes spreading furthest throughout the region, representing the worst-case scenario, occurs in stable conditions at TKE_100. Wakes interact between immediate wind plant neighbors for all scenarios.

Stratification exerts a stronger effect on wake propagation distance than TKE does. For instance, wakes extending 3.7 km downwind in unstable conditions reach 55.4 km in stable conditions at TKE_100 (Fig. 12a, c), similar to the estimate of 50 km from Golbazi et al. (2022). Likewise, wake deficits reaching 5.9 km downwind in unstable stratification reach 55.4 km downwind in stable stratification at TKE_0 (Fig. 12b, d). The same pattern exists for CA wakes (Fig. D1). Overall, altering the added TKE amount has a small impact on the propagation distance of wakes relative to stratification, and combining stable stratification with TKE_0 results in the strongest wakes.

Yearly averaged wakes show similar trends with TKE and stability (Table 4). The maximum wake strength intensifies from -2.2 to $-2.5\,\mathrm{m\,s^{-1}}$ moving from TKE_100 to TKE_0 (Fig. 12e, f). Reducing TKE also increases the spatial coverage of wakes from $13\,040\,\mathrm{km^2}$ using TKE_100 (Fig. 12e) to $13\,268\,\mathrm{km^2}$ using TKE_0 (Fig. 12f). Downwind propagation distances remain similar over the yearlong period with wakes reaching 43.4 km at TKE_100 and 41.3 km at TKE_0.

Reduced TKE limits turbulence-induced momentum transport from aloft, thereby increasing wake strength. Counterintuitively, longer-lasting wakes in TKE_100 develop from a larger reduction in momentum from wake recovery above the turbines (Fitch et al., 2012; Siedersleben et al., 2020), leaving less momentum available for replenishment downwind.

Table 3. Wake wind speed reduction by stratification and TKE amount.

	Unstable TKE_100	Stable TKE_100	Unstable TKE_0	Stable TKE_0
Wind speed deficit	$-1.5\,\mathrm{m\,s^{-1}}$	$-2.8\,\mathrm{m\,s^{-1}}$	$-1.8\,\mathrm{m\,s^{-1}}$	$-3.1\,\mathrm{m\,s^{-1}}$
Normalized deficit	16 %	25 %	19 %	27 %

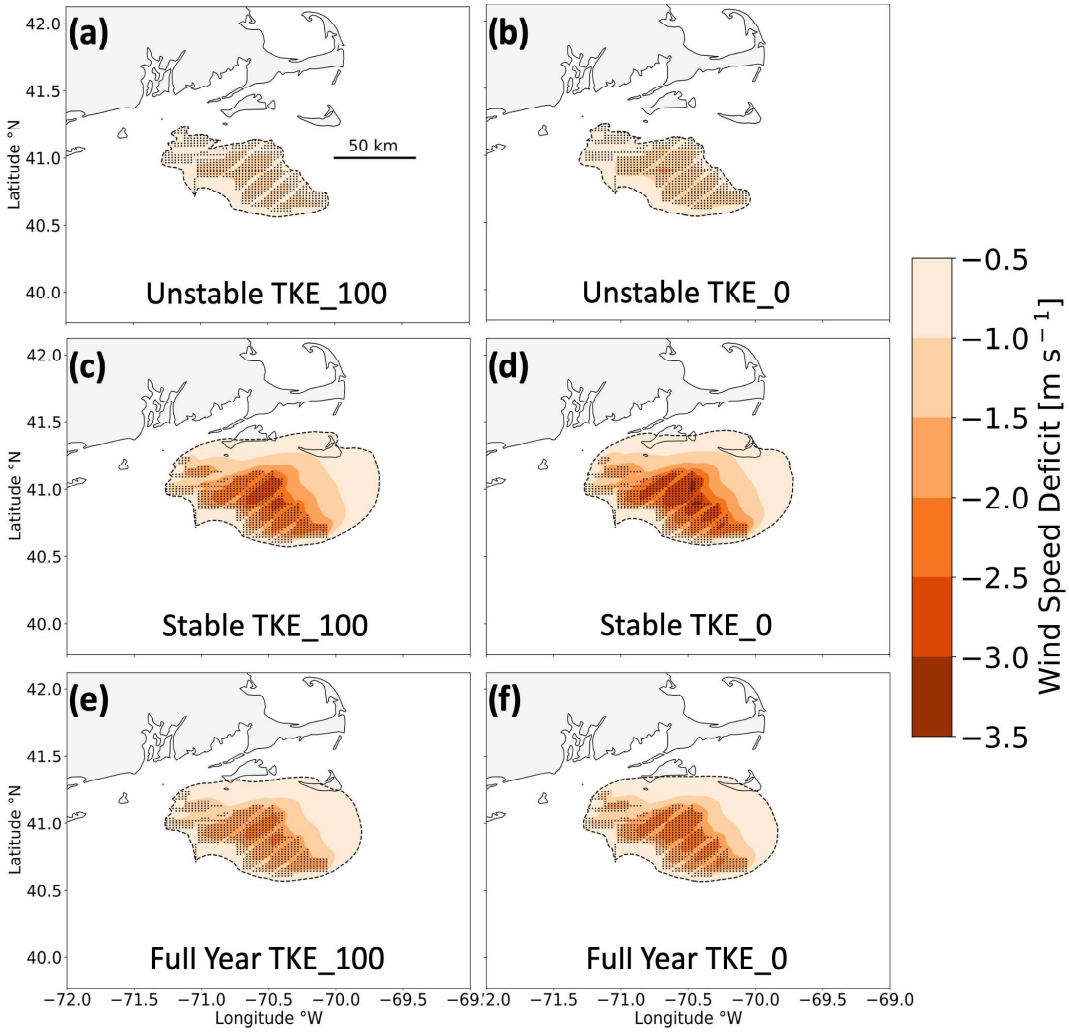

Figure 12. Average wake wind speeds among the lease areas during **(a, b)** unstable stratification, **(c, d)** stable stratification, and **(e, f)** the full 1 September 2019 to 1 September 2020 period. Wakes are simulated with 100 % added TKE **(a, c, e)** or 0 % added TKE **(b, d, f)**. Wind speed deficits are shown by the colored contouring, and turbines are shown as the black dots. The $-0.5\,\mathrm{m\,s^{-1}}$ threshold is outlined by the dashed black line.

3.3 Power deficits

3.3.1 External wake losses

ONE experiences power deficits due to external wakes from the LA and the CA. Considering external wakes from the LA at TKE_0 (Eq. 15), the average yearlong power deficit at ONE is 14.7 % (Fig. 13a) and increases to 15.7 % considering only the 4 stable CA months. When ONE is waked by the LA at TKE_100, the average yearlong power deficit reduces to 13.4 % (Fig. 13b) because increased turbulence supports faster replenishment. During the 4 months only, the deficit is 14.4 %. When incorporating wakes from the CA (at TKE_100), the mean ONE power deficit (over 4 months) is 14.3 % (Fig. 13c). By calculating the external power losses as the difference between total and internal losses (Eq. 16) instead, the deficits are 8.97 % and 8.43 % for the LA at TKE_0 and TKE_100, respectively. However, power losses vary as

Table 4. The wake wind speed deficit, spatial extent, and downwind propagation distance by added TKE amount.

	Wind speed deficit	Spatial extent	Propagation distance
TKE_100	$-2.2\,\mathrm{m\,s^{-1}}$	$13\,040\,\mathrm{km^2}$	43.4 km
TKE_0	$-2.5\,\mathrm{m\,s^{-1}}$	$13\,268\,\mathrm{km^2}$	41.3 km

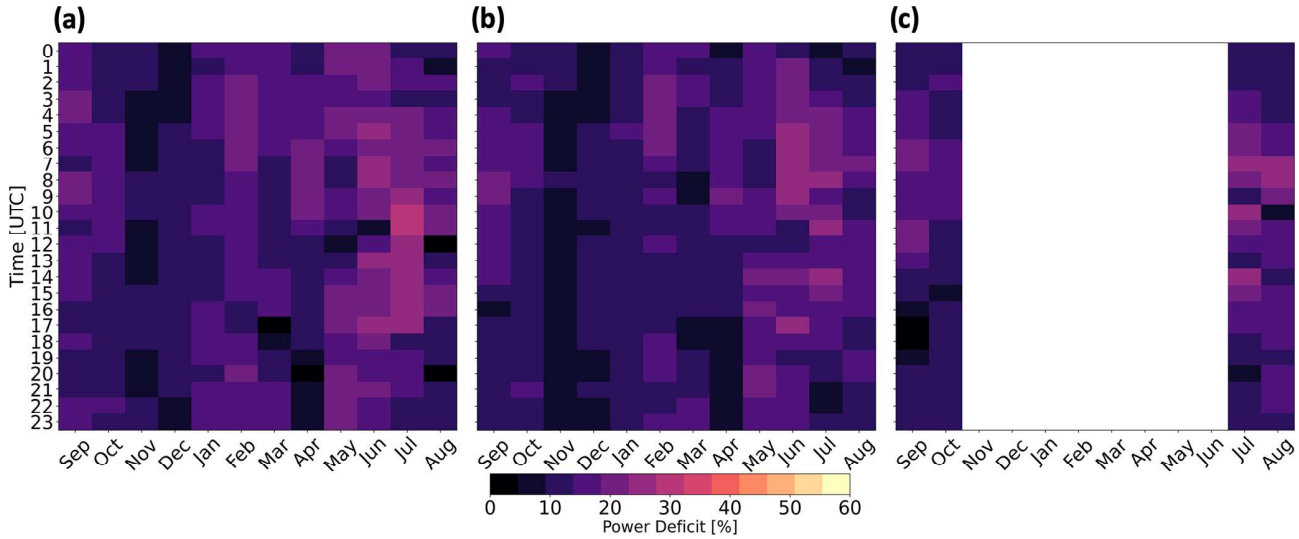

Figure 13. The power deficit at ONE when waked by **(a)** the LA at TKE_0, **(b)** the LA at TKE_100, and **(c)** the CA at TKE_100. The white space reflects the simulation period. The color bar is broad to facilitate comparison with losses in Fig. 14.

larger reductions from external wakes occur during summer, whereas smaller reductions occur during winter.

External wake-induced losses vary both diurnally and seasonally. Larger power deficits occur more often during summer due to stable stratification (Figs. 10, 11a). Smaller power deficits occur during winter (Fig. 13), with faster winds that exceed rated wind speed and unstable conditions that erode wakes faster. Larger power deficits correspond with stable stratification in June and July. Conversely, smaller power deficits occur with unstable stratification throughout November and December. These patterns occur because colder air advects over warmer water in winter, which causes unstable conditions that erode wakes faster. Conversely, warmer air advects over colder water during the summer, inducing stable conditions that limit turbulent wake recovery. While wake-induced losses vary somewhat across the diurnal cycle, there is no discernible pattern. The ocean's large heat capacity suppresses daytime heating, which limits changes in stratification and, by extension, the magnitude of changes in wake losses.

3.3.2 Internal wake losses

Internal power deficits (Eq. 14) at ONE are at least 25 % stronger than externally induced power deficits but experience similar variability with stability and TKE amount (Fig. 14). Internal waking induces weaker deficits during winter and stronger deficits during summer. As with external wakes, a clear diurnal pattern fails to emerge. Yearlong internal wakes from TKE_0 and TKE_100 induce power losses of 29.2 % and 25.7 %, respectively. During the 4 stable months only, the deficits increase to 36.9 % and 32.9 %, respectively. Using different PBL schemes with similar turbine spacing under steady-state idealized conditions, Rybchuk et al. (2022) find similar internal losses to capacity factor, up to 31.6 %.

The average yearlong power deficits (Eq. 13) at ONE considering internal wakes and external wakes from the LA range between 38.2 % (TKE_0) and 34.1 % (TKE_100). These results concur with wake-induced losses found by Pryor et al. (2021) of 35.3 % among the LA, based on 11 periods of different flow scenarios spanning 5 d. Observations of wake-induced power losses have large variability over the year, ranging from as low as 5 % to as high as 40 % (Lee and Fields, 2021). Overall, external wakes produce yearly averaged power losses of 14.1 %, whereas internal wakes induce larger losses of 27.4 %. Thus, we stress the importance of resolving region-specific and time-varying wakes for accurate energy prediction estimates.

3.4 Annual energy production

Predictions of energy supply are critical for planning, operations, and diversification of renewables. Without internal

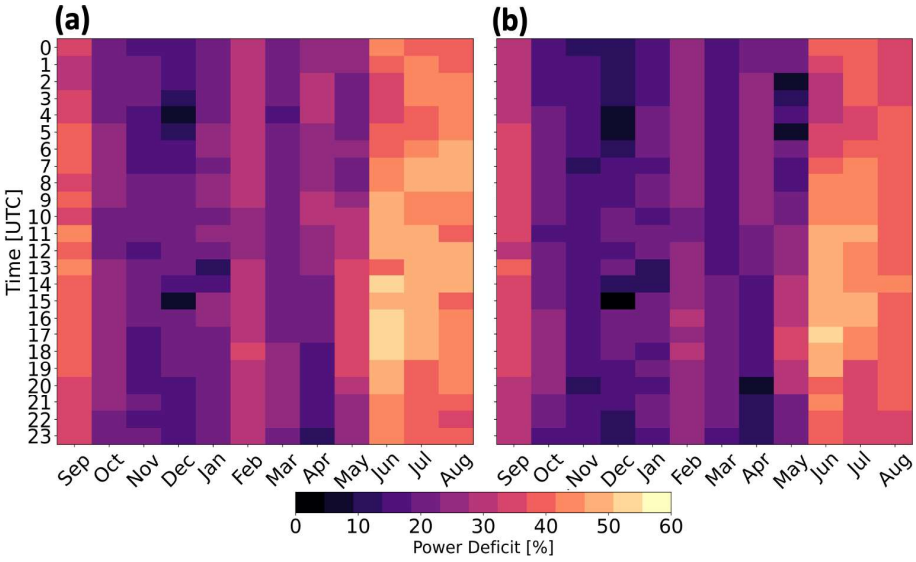

Figure 14. The percentage of power loss at ONE from internal wakes at **(a)** TKE_0 and **(b)** TKE_100.

or external wake effects, ONE would produce 11.61 TW h and meet 10.02 % of New England's average demand. Annual energy production (AEP) from ONE, considering just internal wakes, reduces to 9.19 TW h (TKE_0) or 9.55 TW h (TKE_100), which could meet 7.94 % to 8.24 % of New England's demand. Including both internal and external wakes from the LA, ONE would produce 8.19 TW h (TKE_0) or 8.65 TW h (TKE_100), meeting 7.07 % to 7.47 % of demand.

Increasing the number of wind turbines increases the demand fulfilled; AEP from the LA is 68.12 TW h (TKE_0) or 70.9 TW h (TKE_100), supplying 58.82 % to 61.22 % of New England's demand. On an hourly basis, the LAs fulfill demand only 24.6 % (TKE_0) and 26.5 % (TKE_100) of the time, highlighting the necessity for resolving accurate wake losses across the OCS. Previous work (Livingston and Lundquist, 2020) assuming a constant 20 % wake loss, shown here to be underestimated, has suggested that 2000 turbines of 10 MW could meet New England's demand 37 % of the time. All in all, the LA, with 1418 turbines of 12 MW, supplies 68 and 71 TW h yr^{-1}, or 1.72 % (TKE_0) to 1.65 % (TKE_100) of the nation's energy supply.

3.5 Power variability by TKE amount

3.5.1 Temporal power variability

While differences in wake strength between TKE amounts alter power production, wind speed exerts a larger influence. Maximum power is produced during spring with the least amount of power produced during summer (Fig. 15a) for both TKE_0 and TKE_100 because spring features faster wind speeds (Fig. 15b). Power production responds to hub-height wind speeds (Fig. 15) more than stability conditions (Figs. 10, 11). Reduced power production during summer may be problematic as New England's top-10 utility demand days since 1997 have all occurred in July or August (NEISO, 2023).

Total power production varies slightly between TKE_100 and TKE_0. Due to weaker replenishment within the rotor-swept area, TKE_0 wakes are stronger, so TKE_0 produces less total power than TKE_100 (Fig. 15a). Over the year, TKE_0 runs produce 96.2 % (ONE) and 96.1 % (LA) of the power of TKE_100. This difference does not arise from extreme outliers, as TKE_0 runs produce less power more frequently, at 71.3 % (ONE) or 81.2 % (LA) of the time.

3.5.2 Power variability by wind speed

Differences in power production (TKE_100 − TKE_0) vary by NWF hub-height wind speed (Fig. 16). These differences are small at slow wind speeds because little momentum is available for wake recovery and at faster wind speeds within region 3 of the power curve (11–30 m s^{-1}) where wind speed changes do not affect power production (Fig. 2a). Differences in wind speed within region 3 should have no effect on power production and are caused by numerical noise propagating through wind plant areas (Fig. F1). The largest differences in power production occur in region 2 and around rated wind speed where the power curve is steep (Figs. 2a, 16). Additionally, large differences in power production can occur in specific meteorological conditions such as frontal propagation.

Comparison of power production between TKE amounts by other meteorological variables lacked significant trends. For example, we additionally analyzed differences in power production by wind direction, following the hypothesis that northerly wind directions could transport more turbulence offshore because land has a higher roughness length than the

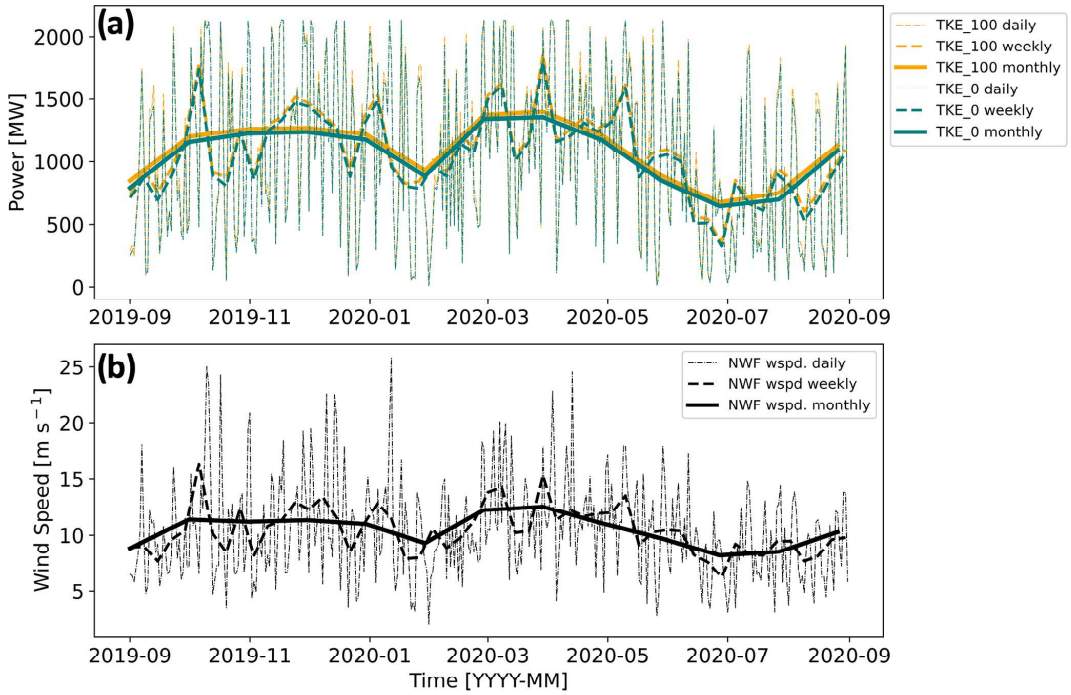

Figure 15. **(a)** Total power production at ONE by TKE amount. TKE_100 power output is shown in orange and TKE_0 output in teal. **(b)** Hub-height NWF wind speed at a point centered on the RIMA block. The dotted lines represent the daily average, dashed lines the 7 d average, and solid lines the 30 d average.

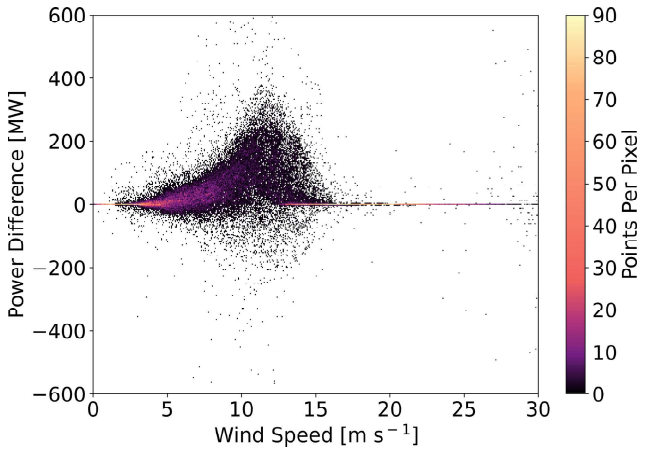

Figure 16. The difference in power production (TKE_100-TKE_0) at ONE as a function of wind speed. The colored contouring depicts the density of scattered points per pixel. Wind speeds are obtained every 10 m from a point centered on ONE at hub height.

ocean. TKE_100 runs may harness this mechanical turbulence more for wake replenishment. Analysis of differences in power production by PBL height also failed to show significant patterns. We assumed that higher PBL heights indicated a greater reservoir of turbulence from which TKE_100 runs could replenish the wake, resulting in greater power production. Further analysis concluded by comparing power differences with the aforementioned variables' rates of change. However, we reached the same conclusions, as higher densities of scattered points existed around frequently occurring conditions such as southwesterly wind directions.

Wake strength varies spatiotemporally between TKE_0 and TKE_100 runs. While the mean difference in wind speed at hub height between TKE_100 and TKE_0 runs indicates that TKE_0 produces stronger wakes, this averaging may obscure the actual spatiotemporal variability. For example, a wind plant may have greater TKE_100 wake wind speeds, while its nearby neighbor has greater TKE_0 wake wind speeds at the same point in time. Additionally, a specific wind plant may not consistently produce stronger wakes under one TKE setting. A wind plant may fluctuate between producing stronger wakes in TKE_100 runs and TKE_0 runs throughout time. This finding suggests that other boundary layer dynamics play a role in wake strength, and the variability of power production must be explored.

We note that wind speed and numerical noise are not the only contributors to power differences. One case study analysis shows that TKE_0 and TKE_100 separately produce more power within respective 99th percentiles over a short period of time in September (Fig. 17c). Investigation reveals that a cold front propagated through the ONE wind plant from the northwest to the southeast during this period. The cold front is identified by a lenticular band of upward vertical motion at the frontal head followed by turbulent vertical

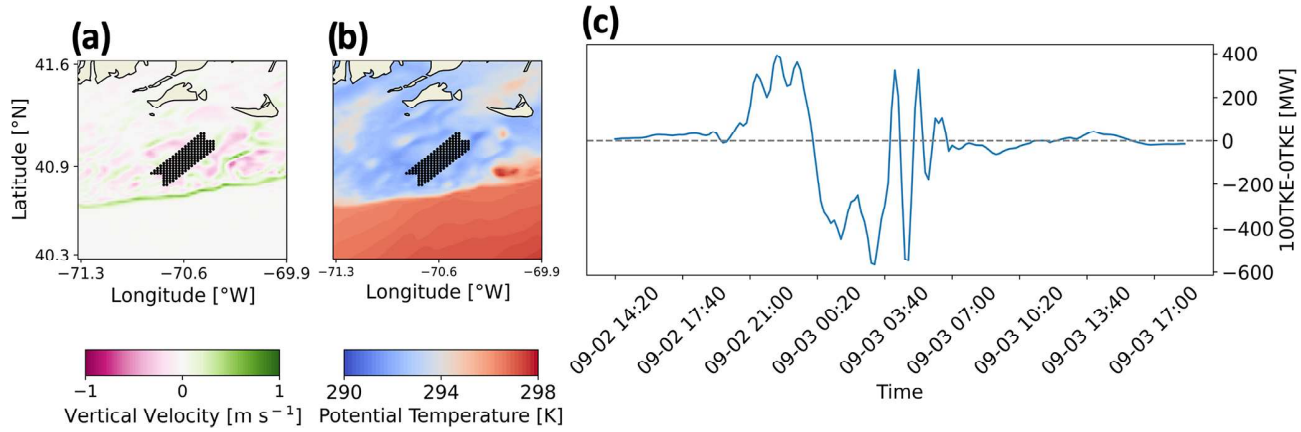

Figure 17. Propagation of a cold front through the ONE wind plant. **(a)** NWF vertical wind speed is shown as the colored contour with upward vertical velocities in greens and downward vertical velocities in purples. **(b)** NWF potential temperature is shown with lower temperatures in blues and higher temperatures in reds. In both **(a)** and **(b)**, the black dots indicate wind turbine locations in ONE TKE_0 and TKE_100. **(c)** The difference in power production between TKE_100 and TKE_0 is shown in MW, with positive values indicating that TKE_100 produces more power.

motion (Fig. 17a) in addition to advection of lower potential temperatures (Fig. 17c). As the cold front approaches, more power is produced by the TKE_100 simulation and is within the 99th percentile. When the frontal head first interacts with Vineyard Wind, more power is produced by the TKE_0 simulation and is within the 99th percentile. Conversely, TKE_100 produces more power following the frontal head. Frontal propagation can induce Kelvin–Helmholtz instabilities, the turbulence of which may aid wake recovery by vertically mixing momentum (Jiang, 2021). Increased turbulence in the TKE_100 simulation can harness more downward vertical transport of momentum from Kelvin–Helmholtz instabilities aft of the frontal head, increase wake replenishment, and produce more power.

4 Conclusions

This modeling study assesses the variability of wake effects across the mid-Atlantic OCS based on yearlong simulations, including a first step towards uncertainty quantification and approaches for distinguishing internal and external wake effects. In addition to a simulation without wind plants (NWF), validated by comparison to floating lidar observations, three wind plant layouts are explored, including a representative wind plant alone (ONE), all lease areas (LA), and the lease areas plus the call areas (CA). Modifying the added TKE amount (TKE_0 or TKE_100) by turbines provides uncertainty quantification in power production estimates.

The OCS is characterized by more frequent unstable stratification during winter and stable stratification during summer (Bodini et al., 2019; Optis et al., 2020; Debnath et al., 2021). In stable conditions, wakes are stronger and propagate further downwind, (Fitch et al., 2013; Vanderwende et al., 2016; Porté-Agel et al., 2020). In the worst-case scenario where downwind wake recovery diminishes during stable stratification, mean wakes propagate 55 km downwind. While wakes may not reach downwind clusters on average, inter-cluster waking occurs intermittently. While TKE_0 produces stronger wakes than TKE_100, the downwind propagation distances do not differ.

Reduced wake wind speeds, as compared to the NWF simulation, affect power production. Yearly averaged wake losses induce power deficits at ONE from 38.2 % (TKE_0) to 34.1 % (TKE_100). This deficit comprises both internal and external waking. External wakes induce yearly averaged power losses of 14.7 % (TKE_0) or 13.4 % (TKE_100), whereas wakes from the CA induce similar losses of 14.3 % over 4 months. Using an alternative method, external wakes induce losses of 8.97 % and 8.43 % for the LA at TKE_0 and TKE_100, respectively. Internal wakes at ONE promote larger power losses of 29.2 % (TKE_0) or 25.7 % (TKE_100). Wake-induced power losses vary seasonally with smaller diurnal variability. Larger power deficits occur during summer, where frequent stable conditions limit wake erosion. Although upwind clusters may generate strong external wakes among the LA, wind plant orientation with respect to prevailing winds can reduce adverse impacts from nearby neighbors. Ample distance for replenishment of external wakes by the CA moderates the negative effects. Internal wake losses remain larger due to shorter distances with limited wake recovery. Both external and internal wake-induced losses grow in summer stably stratified conditions. These losses similarly increase in strength for TKE_0 simulations from inhibited recovery.

Resolving precise wake losses and AEP are crucial for stakeholders and grid operators. In the absence of wakes, ONE could supply 10.02 % of New England's demand. Operating alone, ONE's supply reduces to 7.94 % (TKE_0) or

8.24 % (TKE_100). Adding external wakes from the LA, ONE's annual supply lessens to 7.07 % (TKE_0) or 7.47 % (TKE_100). Although wakes are stronger among the LA, the greater number of turbines can meet 58.82 % (TKE_0) and 61.22 % (TKE_100) of New England's demand, or roughly 1.72 % and 1.65 % of national demand. However, the LA only satisfies demand about 25 % of the time on an hourly basis. Overall, spring features maximum power production with the fastest hub-height wind speeds. Wind speeds are slower in summer, reducing power production during July and August, which have featured New England's top-10 utility demand days since 1997 (NEISO, 2023).

Variable TKE amounts marginally impact power generation. TKE_0 simulations average 3.8 % less production than TKE_100 throughout the year, as reduced turbulence in TKE_0 limits momentum transport into the waked zone. Although differences in power production are small, both simulations exhibit large variability at short temporal periods. Improving WFP accuracy by accounting for wind shear throughout the rotor-swept region (Redfern et al., 2019) and dynamic air density may increase the variability in power production further (Wu et al., 2022). Further, different sizes of turbines may be installed in some of these regions, and the size of the turbine can influence the impacts of the turbine (Golbazi et al., 2022).

Future wind resource assessments may neglect differences between TKE_0 and TKE_100 because the power production offset is minor, although we identify a strong outlier during a frontal passage when differences in power production between TKE_100 and TKE_0 are large. While power production differences are minor, effects on other atmospheric variables may be more significant (Fig. A1). Variability may be influenced by other meteorological conditions. Successive analyses should consider yearlong CA simulations to identify the full range of external wake impacts. Although we infer that the effects of CA wakes on ONE are small relative to LA wakes, yearlong estimates may show otherwise. Notably, we find that internal wakes have larger impacts on power production than those generated externally.

Appendix A

To assess the sensitivity of simulations to the amount of parameterized TKE, we conducted a set of 2 d test runs from 11 to 13 July 2017. This time period was chosen for its predominance of southwesterly winds, which represent typical conditions across the OCS, and for the availability of Air–Sea Interaction Tower lidar observations for wind profile validation of the NWF simulations. Test runs consist of 0 % (TKE_0), 25 % (TKE_25), 50 % (TKE_50), and 100 % (TKE_100) added TKE with the WFP.

Hub-height wind speeds vary by simulation type and added TKE amount (Fig. A1a). Mean WFP wind speeds are always slower than NWF wind speeds due to the momentum sink introduced by wind turbines, by 2.9 m s^{-1}. Larger variations between wind speeds (Fig. A1a) correspond with larger spreads in power output by TKE amount (Fig. A1c). The sequencing of power production driven by TKE amount remains consistent, namely that the differences progress from TKE_0 to TKE_25, TKE_50, TKE_75, and TKE_100. Because power production totals for TKE_25 and TKE_50 are typically bounded by the totals for TKE_0 and TKE_100, production simulations incorporate TKE_0 and TKE_100 only to account for the full range of uncertainty throughout a full yearlong period from 1 September 2019 to 1 September 2020.

Although subtle, several important meteorological quantities from the model grid cell at the center of the RIMA block vary by the added TKE amount. For example, wind speeds are slower on 12 July between 12:00 and 16:00 UTC (Fig. A1a). The wind speed reduction during this time period causes a corresponding decrease in turbulent transport of moisture. The mean difference in moisture fluxes throughout the full period between TKE_100 and TKE_0 is 2.84×10^{-6} kg m^{-2} s^{-1} (Fig. A1b). Note that the surface moisture flux remains negative throughout the period. While maritime moisture profiles typically exhibit a decrease in concentration with height, corresponding with a positive flux, mixing from the turbines reduces the near-surface concentration and reverses the gradient.

Heat flux exhibits large variability. The mean difference in heat flux throughout the full period between TKE_100 and TKE_0 is 3.61 W m^{-2} (Fig. A1d). The wind speed decrease between 12:00 and 16:00 UTC reduces surface stresses and turbulent transport of heat. The reduction in heat flux during this time period causes 2 m temperatures to decrease and exhibit less variability by TKE amount, with a mean difference of 0.26 K between TKE_100 and TKE_0 (Fig. A1f).

The reduction in turbulent mixing lowers the PBL, regardless of TKE amount, to shallow heights between 30 to 80 m at 13:00 UTC (Fig. A1e). The near-surface PBL height suppresses the small variations in turbulent mixing across test runs and causes fluxes to equalize. PBL heights differ the most by added TKE amount and may result from changes in weighting between two separate height determination methods present in the MYNN physics driver (Fig. A1c).

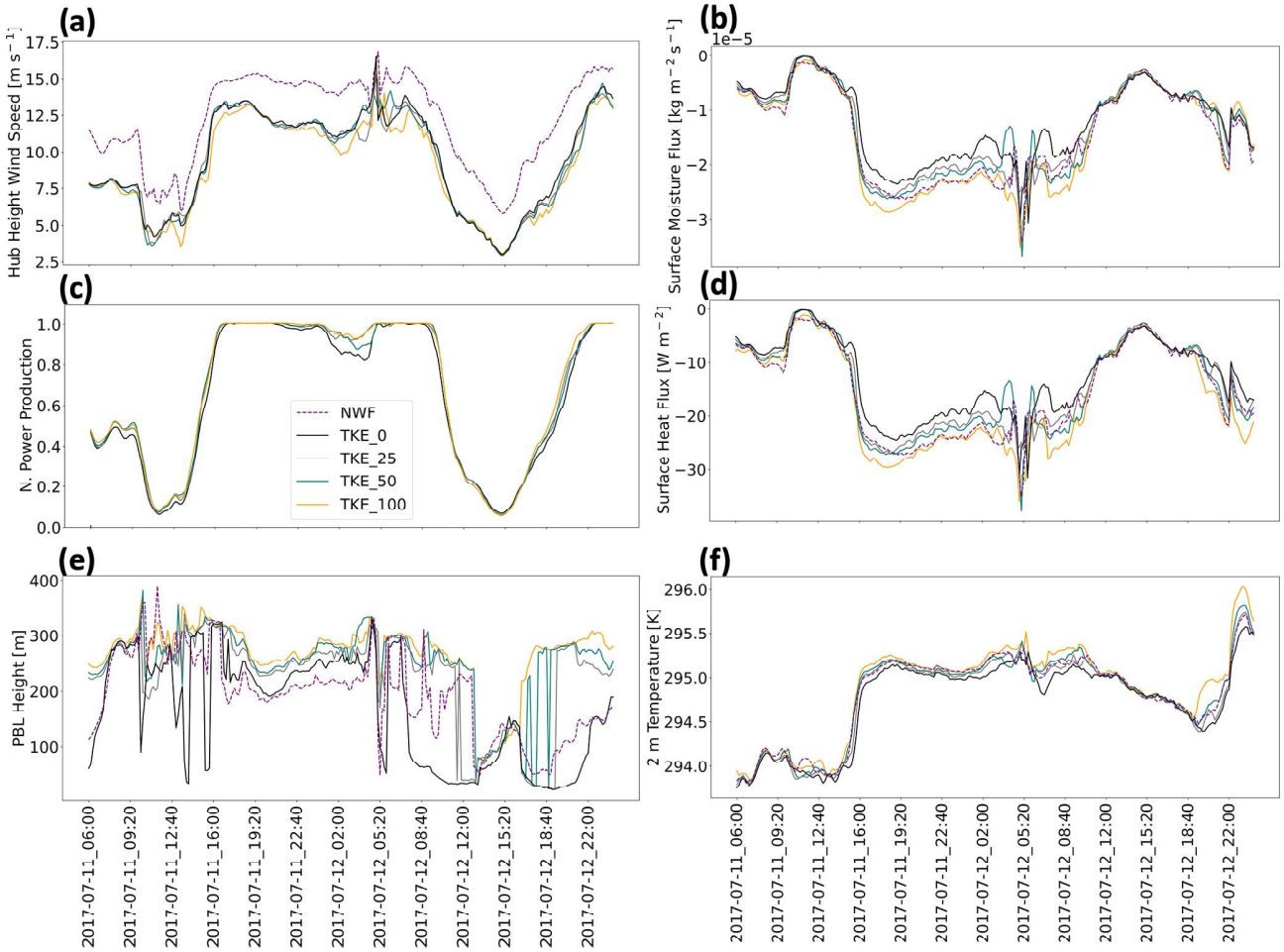

Figure A1. The effects of modifying the amount of turbulent kinetic energy (TKE) during test runs. Panels show **(a)** hub-height wind speed, **(b)** surface moisture flux, **(c)** normalized power production, **(d)** surface heat flux, **(e)** planetary boundary layer (PBL) height, and **(f)** 2 m temperature. Values are collected from a point centered on the RIMA block. Power production is the sum of all cells containing wind turbines. TKE_100 is shown in orange, TKE_50 in blue, TKE_25 in gray, TKE_0 in black, and NWF in purple dashes.

Appendix B

Stratification at the E05 and E06 lidars (Fig. B1) exhibits similar seasonal variability to the RIMA block (Fig. 10). The winter months feature predominant unstable stratification caused by cold air advecting over a warm sea surface. In the spring and early summer, stratification transitions to more common stable conditions as warm air advects over a cooler sea surface. Stratification is most commonly unstable in November and stable in May.

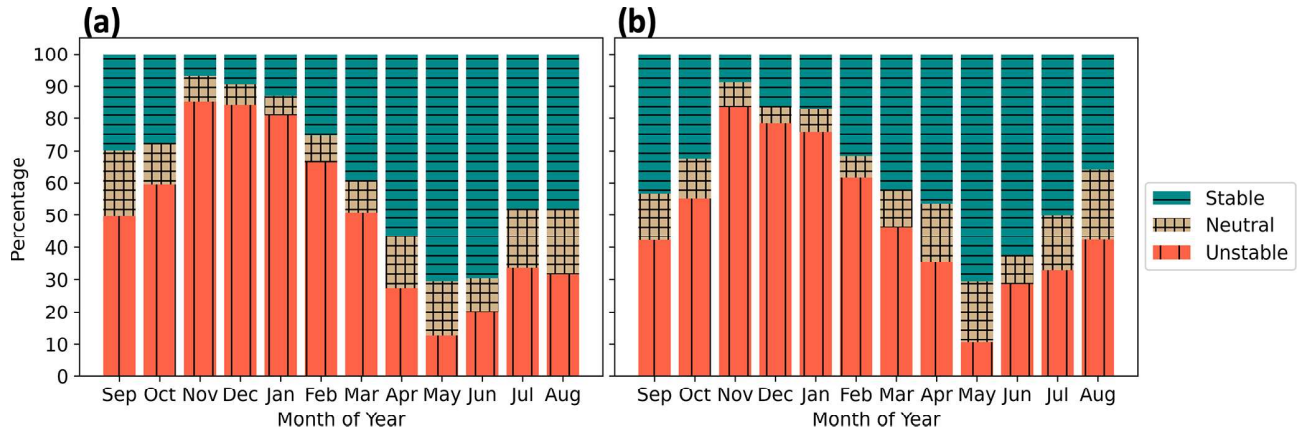

Figure B1. Stability classification using the Obukhov length for the 1 September 2019 to 1 September 2020 period at the **(a)** E05 and **(b)** E06 lidars from NWF. The tan crosshatches are neutral stratification, blue horizontal bars are stable stratification, and red vertical bars are unstable stratification.

Appendix C

Surface estimates of L may not represent stability aloft (Fig. C1) and may overestimate unstable conditions. When considering monthly averaged potential temperature profiles through the rotor layer, only November and December appear unstably stratified. While September and October appear predominantly unstable based on surface estimates, potential temperature gradients within the rotor-swept area suggest slightly stable conditions, supporting inferences that offshore conditions are stable during late summer. Therefore, our limited set of CA simulations focus on 1 September to 31 October 2019 and 1 July to 31 August 2020 for its presumed abundance of stable stratification.

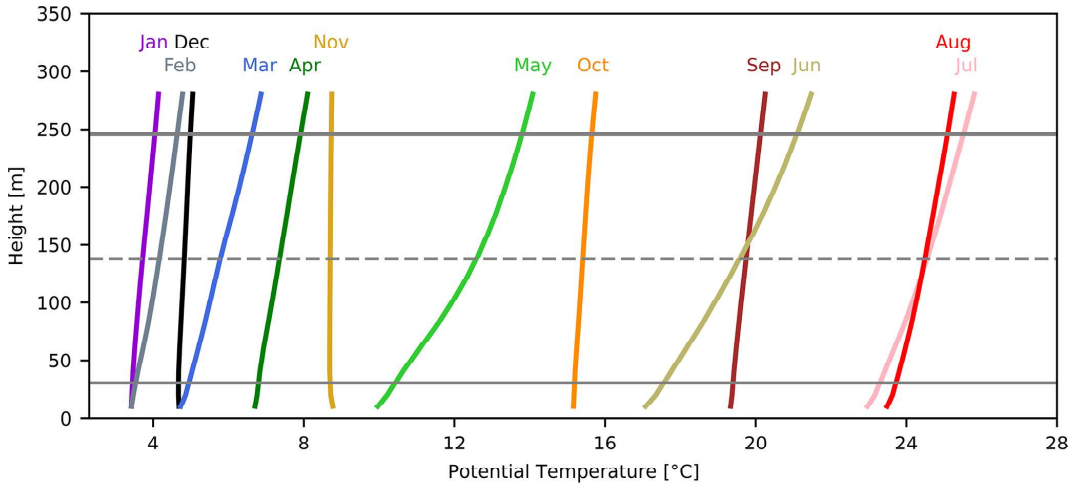

Figure C1. Monthly averaged WRF-simulated potential temperature profiles at a point centered on the RIMA block. Horizontal gray lines indicate the levels of the hub height (dashed) and the rotor-swept area (solid).

Appendix D

Wakes in the simulations with CA show similar dependence on stratification (Fig. D1). Note that we simulate the CA for 4 months only (1 September to 31 October 2019 and 1 July to 31 August 2020) at one TKE level only (TKE_100) due to computational costs. The maximum wake strength intensifies from -1.6 to $-3.2\,\mathrm{m\,s^{-1}}$ moving from unstable to stable stratification (Fig. D1b, c).

Wake propagation distance for the call area simulation is also affected by stratification. During the 4 months considered, unstable, stable, and neutral conditions occur 38.2 %, 53.4 %, and 8.3 % of the time, respectively. As such, there is essentially an even split between the percentage of occurrence of unstable and stable conditions. In unstable conditions, wakes from the two southernmost lease areas fail to reach neighboring downwind clusters on average, and no wakes stronger than this threshold reach the RIMA block (Fig. D1e). In stable stratification, wakes from each cluster reach downwind clusters, including the RIMA block (Fig. D1f). Averaged over all 4 months, wakes between LA and the CA along the New Jersey and New York bights affect each other, but no wakes reach the RIMA block. Wakes may still interact with downwind plants at individual times and affect power production.

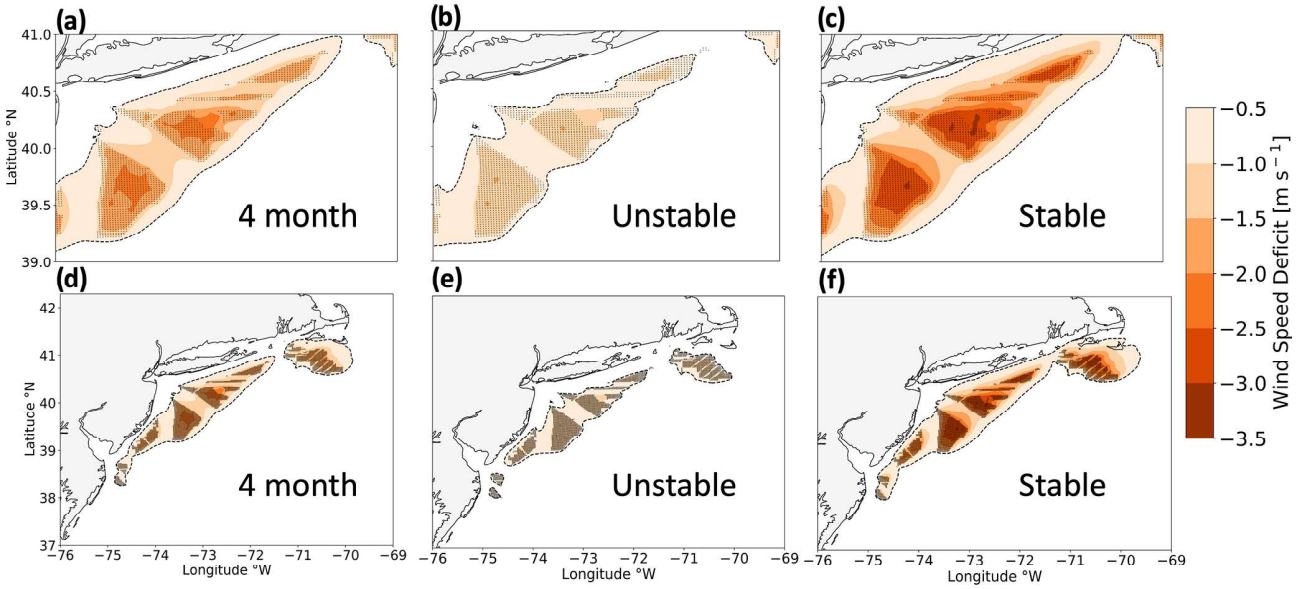

Figure D1. Average wake wind speed deficits among the call areas **(a, d)** for the combined 4-month period, 1 September to 31 October 2019 and 1 July to 31 August 2020, **(b, e)** during unstable stratification and **(c, f)** during stable stratification. All panels show 100 % added TKE. Wake wind speed deficits are shown by the colored contour, and turbines are shown as black dots. The upper row is zoomed in to increase granularity.

Appendix E

Here, we characterize the (WFP-NWF) TKE differences by maximum value and by spatial extent. The maximum average TKE additions remain similar by stratification at TKE_100, reaching 1.00, 1.01, and 1.00 $m^2\,s^{-2}$ during unstable conditions, stable conditions, and the full year, respectively (Fig. E1a, c, e). The amount of added TKE is not homogeneous across the wind plants in TKE_100, as the greatest contributions occur in grid cells containing more wind turbines. Some TKE is introduced in TKE_0 due to wind speed shear, although the amounts are over an order of magnitude smaller. The maximum average TKE amounts for TKE_0 are 0.05, 0.03, and 0.03 $m^2\,s^{-2}$ during unstable conditions, stable conditions, and the full year, respectively. Being purely shear induced, regions experiencing the most TKE in TKE_0 correspond more with the maximum wake wind speed deficits (Fig. 12b, d, f).

We further characterize added TKE amounts by their spatial extent. We report the area encompassed by added TKE amounts greater than a threshold of 0.005 $m^2\,s^{-2}$ because a cutoff of 0 $m^2\,s^{-2}$ includes noise throughout the domain (Fig. F1), and the spatial extent is not realistic. In TKE_100, the spatial extents are 10 724, 10 064, and 9608 km^2 in unstable stratification, stable stratification, and for the full year, respectively (Fig. E1a, c, e). In TKE_0, the spatial extents are 13 888, 10 724, and 11 332 km^2 in unstable stratification, stable stratification, and for the full year, respectively (Fig. E1b, d, f).

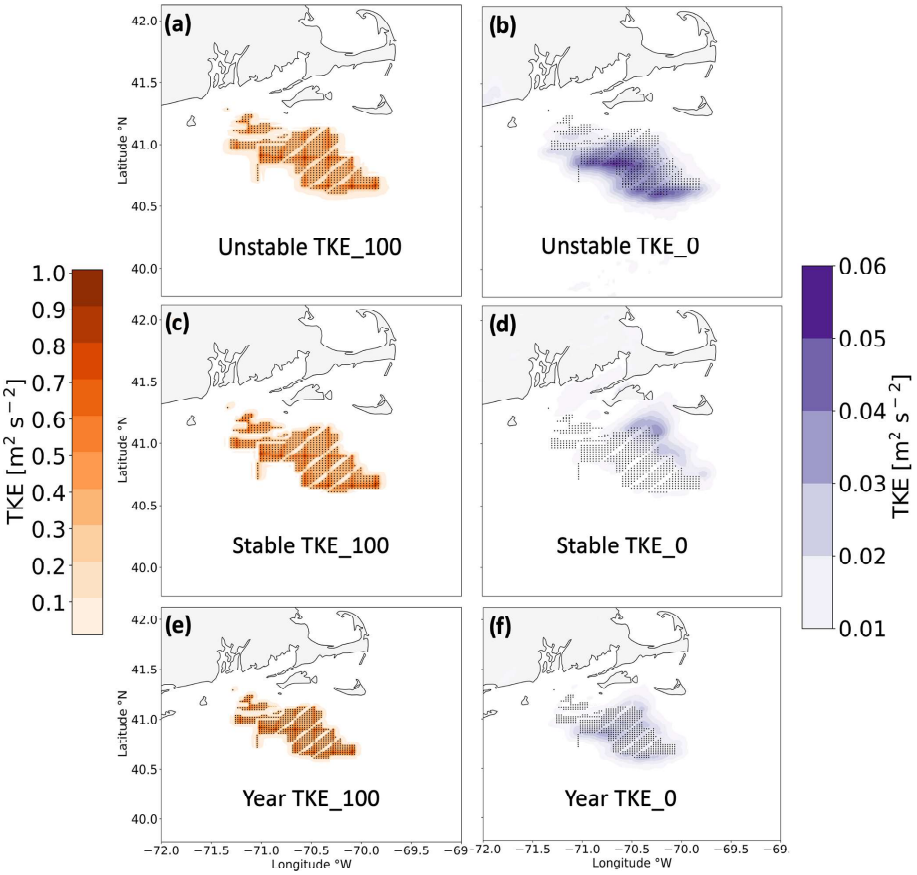

Figure E1. Average hub-height (WFP-NWF) TKE difference among the lease areas during **(a, b)** unstable stratification, **(c, d)** stable stratification, and **(e, f)** the full 1 September 2019 to 1 September 2020 period. Panels show 100 % added TKE **(a, c, e)** or 0 % added TKE **(b, d, f)**. The TKE amount is shown by the colored contouring, and turbines are shown as the black dots.

Appendix F

Results can show evidence of numerical noise, which emerges when simulations incorporate the WFP (Ancell et al., 2018; Lauridsen and Ancell, 2018). In our simulations, these brief periods of numerical noise emerge and decay, often coincident with precipitation. While we expect differences in wake wind speed immediately downwind of power plants, it is unlikely that these differences could advect to the southeast corner of the domain, roughly 600 km southeast of the RIMA block (Fig. F1a). If this numerical noise occurred in grid cells with turbines, then this noise would introduce error in power estimations.

We explored several approaches to mitigate the numerical noise, none of which succeeded. First, we increased the floating-point accuracy of numerical calculations by enabling double precision in WRF. Double precision limits the growth of rounding error to smaller magnitudes (Ancell et al., 2018). This attempt aimed to confine perturbations to smaller orders of magnitude that take longer periods of time to become substantial. To prevent "runaway" error growth after long periods of time, we submit simulation restarts each month.

In observing a spatial correlation of numerical noise with convective precipitation during test runs, we reran test simulations with a more complex microphysics scheme. The Thompson microphysics scheme, used throughout, is double moment with respect to cloud ice only. We substituted the Morrison microphysics scheme, which is fully double moment with respect to cloud droplets and rain, cloud ice, snow, and graupel (Morrison et al., 2009). The use of Morrison microphysics did not improve numerical noise, so its computational cost could not be justified.

Next, we introduced a filter for shortwave numerical noise by prohibiting upgradient diffusion. Doing so requires setting the parameter diff_6th_opt to 2 in the namelist, as certain combinations of advection and diffusion orders are conducive to mitigating noise around heavy precipitation (Kusaka et al., 2005). While Kusaka et al. (2005) found the combination of fifth-order advection and sixth-order diffusion to perform best, we had previously attempted this combination because default advection in WRF is fifth order. Thus, we attempted the next best recommendation – combining sixth-order advection and diffusion. Again, this combination did not improve results.

We made a final attempt at noise reduction by running an ensemble of three members using a stochastic kinetic energy backscatter scheme. Ensemble members contain seeds with variable time steps that randomly inject kinetic energy into grid cells (Berner, 2013). These stochastic supplements replenish the kinetic energy sink from unresolvable subgrid-scale processes. We followed recommendations to perturb the stream function and potential temperature backscatter rates by 1×10^{-5} and 1×10^{-6}, respectively. Again, while subtle differences emerged between the simulations, little improvement was found.

We saw little improvement from the aforementioned preprocessing efforts. Given this lack of improvement and a need to conserve computational resources, we employed averaging during postprocessing to alleviate the effects of noise. Modifying averaging periods impacts the range of numerical noise in the wind speed field (Fig. F1b). Noise occurring in grid cells containing turbines could undermine power estimation accuracy, and we observed noise occurring in the southeastern portion of the domain. Subtraction of wind speeds between simulations with variable TKE amounts should only show differences within the wake, and such differences are a result of noise. Averaging periods provide greater relief. While 2 and 4 h averaging periods deliver the best results, these temporal scales can hide important diurnal variability. Conversely, a 30 min averaging period can improve results, but local extrema occasionally reach magnitudes similar to the magnitudes of the raw noise. Thus, hourly averaging can mitigate noise without masking important variability. As a final note, other researchers have benefitted by employing grid nudging within this domain above the PBL (Maryam Golbazi, personal communication, September 2022).

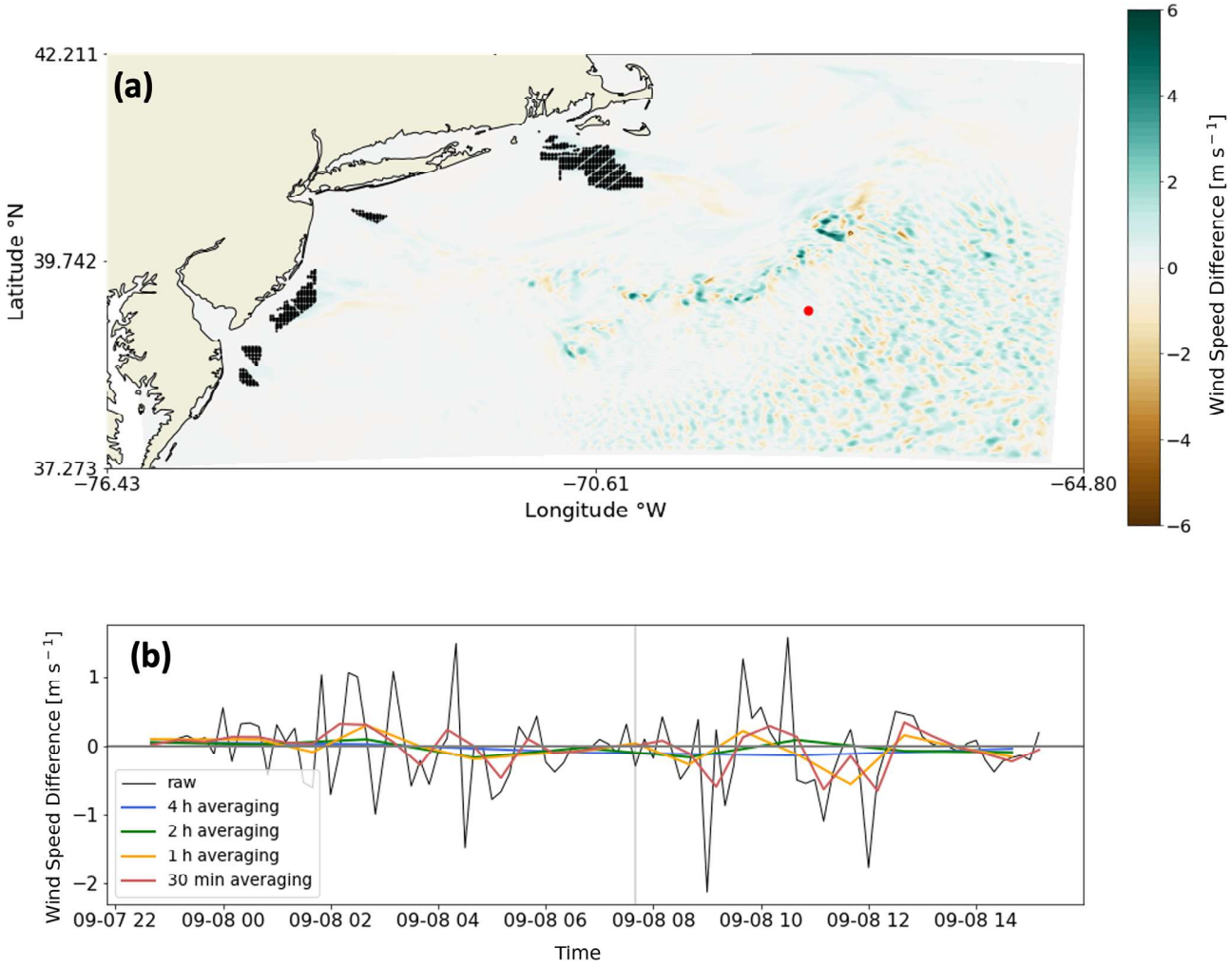

Figure F1. **(a)** The wind speed difference between TKE_100 and TKE_0 at the hub height from LA runs. Wind turbines are shown as black dots. The blue contouring indicates TKE_100 produced faster wind speeds and vice versa. **(b)** Wind speeds obtained at the red circle in **(a)** are shown as a time series. The raw difference in wind speeds and averaging periods are shown as different line colors in the time series. The vertical gray line shows the time stamp of the map.

Code and data availability. The data and files that support this work are publicly available. The ERA5 boundary conditions can be downloaded from the ECMWF Climate Data Store at https://doi.org/10.24381/cds.bd0915c6 (Hersbach et al., 2023). Shapefiles including the bounding extents of the lease and call areas are available at https://www.boem.gov/renewable-energy/mapping-and-data/renewable-energy-gis-data (Bureau of Ocean Energy Management, 2023). Individual turbine coordinates and their power and thrust curves are provided at https://doi.org/10.5281/zenodo.7374283 (Rosencrans, 2022). WRF namelists for NWF and WFP simulations can be obtained at https://doi.org/10.5281/zenodo.7374239 (Rosencrans, 2021). The simulation output data will be available in HDF5 format at https://doi.org/10.25984/1821404 (National Renewable Energy Laboratory, 2020).

Author contributions. Conceptualization: JKL and MO. Methodology: DR, JKL, and MO. Software: DR, AR, and MR. Validation: DR. Formal analysis: DR. Investigation: DR and JKL. Resources: MO and NB. Writing (original draft): DR and JKL. Writing (review and editing): all co-authors. Visualization: DR. Supervision: JKL, MO, and NB. Project administration: MO and NB. Funding acquisition: MO and NB.

Competing interests. At least one of the (co-)authors is a member of the editorial board of *Wind Energy Science*. The peer-review process was guided by an independent editor. Furthermore, Mike Optis co-authored the submitted manuscript while he was an employee of the National Renewable Energy Laboratory. He has since founded Veer Renewables, which recently released a wind modeling product, WakeMap, which is based on a similar numerical weather prediction modeling framework as the one described in this paper. Data from WakeMap are sold to wind energy stakeholders for profit. Public content on WakeMap include a website (https://veer.eco/wakemap/, last access: 18 March 2023), a white paper (https://veer.eco/wp-content/uploads/2023/02/WakeMap_White_Paper_Veer_Renewables.pdf, last access: 18 March 2023), and several LinkedIn posts promoting WakeMap. Mike Optis is the founder and president of Veer Renewables, a for-profit consulting company. Mike Optis is a shareholder of Veer Renewables and owns 92 % of its stock.

Disclaimer. The views expressed in the article do not necessarily represent the views of the DOE or the U.S. Government. The U.S. Government and the publisher, by accepting the article for publication, acknowledge that the U.S. Government retains a nonexclusive, paid-up, irrevocable, worldwide license to publish or reproduce the published form of this work, or allow others to do so, for U.S. Government purposes. Neither NYSERDA nor OceanTech Services/DNV have reviewed the information contained herein and the opinions in this report do not necessarily reflect those of any of these parties.

Publisher's note: Copernicus Publications remains neutral with regard to jurisdictional claims made in the text, published maps, institutional affiliations, or any other geographical representation in this paper. While Copernicus Publications makes every effort to include appropriate place names, the final responsibility lies with the authors.

Acknowledgements. This work was supported by an agreement with NREL under APUP UGA-0-41026-125. This work was authored (in part) by the National Renewable Energy Laboratory, operated by the Alliance for Sustainable Energy, LLC, for the US Department of Energy (DOE) under contract no. DE-AC36-08GO28308. A portion of computation used the Blanca condo computing resource at the University of Colorado Boulder. Blanca is jointly funded by computing users and the University of Colorado Boulder. A portion of computation used the Summit supercomputer, which is supported by the National Science Foundation (awards ACI-1532235 and ACI-1532236), the University of Colorado Boulder, and Colorado State University. The Summit supercomputer is a joint effort of the University of Colorado Boulder and Colorado State University. A portion of this research was performed using computational resources sponsored by the DOE's Office of Energy Efficiency and Renewable Energy and located at NREL.

Financial support. Funding was provided by the US Department of Energy's Office of Energy Efficiency and Renewable Energy and the Wind Energy Technologies Office and by the National Offshore Wind Research and Development Consortium (grant no. CRD-19-16351).

Review statement. This paper was edited by Andrea Hahmann and reviewed by three anonymous referees.

References

218th Legislature: NJ Renewable Portfolio Standards, https://pub.njleg.gov/bills/2018/A4000/3723_I1.PDF (last access: 10 August 2022), 2018.

Aitken, M. L., Kosoviæ, B., Mirocha, J. D., and Lundquist, J. K.: Large eddy simulation of wind turbine wake dynamics in the stable boundary layer using the Weather Research and Forecasting Model, J. Renew. Sustain. Ener., 6, 033137, https://doi.org/10.1063/1.4885111, 2014.

Ancell, B. C., Bogusz, A., Lauridsen, M. J., and Nauert, C. J.: Seeding Chaos: The Dire Consequences of Numerical Noise in NWP Perturbation Experiments, B. Am. Meteorol. Soc., 99, 615–628, https://doi.org/10.1175/BAMS-D-17-0129.1, 2018.

Antonini, E. G. A., Romero, D. A., and Amon, C. H.: Optimal design of wind farms in complex terrains using computational fluid dynamics and adjoint methods, Appl. Energ., 261, 114426, https://doi.org/10.1016/j.apenergy.2019.114426, 2020.

Archer, C. L., Colle, B. A., Veron, D. L., Veron, F., and Sienkiewicz, M. J.: On the predominance of unstable atmospheric conditions in the marine boundary layer offshore of the U.S. northeastern coast, J. Geophys. Res.-Atmos., 121, 8869–8885, https://doi.org/10.1002/2016JD024896, 2016.

Archer, C. L., Wu, S., Ma, Y., and Jiménez, P. A.: Two Corrections for Turbulent Kinetic Energy Generated by Wind Farms

in the WRF Model, Mon. Weather Rev., 148, 4823–4835, https://doi.org/10.1175/MWR-D-20-0097.1, 2020.

Arthur, R. S., Mirocha, J. D., Marjanovic, N., Hirth, B. D., Schroeder, J. L., Wharton, S., and Chow, F. K.: Multi-Scale Simulation of Wind Farm Performance during a Frontal Passage, Atmosphere, 11, 245, https://doi.org/10.3390/atmos11030245, 2020.

Beiter, P., Musial, W., Duffy, P., Cooperman, A., Shields, M., Heimiller, D., and Optis, M.: The Cost of Floating Offshore Wind Energy in California Between 2019 and 2032, NREL/TP-5000-77384, https://doi.org/10.2172/1710181, 2020.

Berner, J.: WRF Implementation Details and Version history of a Stochastic Kinetic-Energy Backscatter Scheme (SKEBS), National Center for Atmospheric Research Tech. Note, https://www2.mmm.ucar.edu/wrf/users/docs/skebs_in_wrf.pdf (last access: 22 July 2023), 2013.

Bodini, N., Lundquist, J. K., and Kirincich, A.: U.S. East Coast Lidar Measurements Show Offshore Wind Turbines Will Encounter Very Low Atmospheric Turbulence, Geophys. Res. Lett., 46, 5582–5591, https://doi.org/10.1029/2019GL082636, 2019.

Bodini, N., Optis, M., Redfern, S., Rosencrans, D., Rybchuk, A., Lundquist, J. K., Pronk, V., Castagneri, S., Purkayastha, A., Draxl, C., Krishnamurthy, R., Young, E., Roberts, B., Rosenlieb, E., and Musial, W.: The 2023 National Offshore Wind data set (NOW-23), Earth Syst. Sci. Data Discuss. [preprint], https://doi.org/10.5194/essd-2023-490, in review, 2023.

Bureau of Ocean Energy Management: Renewable Energy GIS Data, Bureau of Ocean Energy Management [data set], https://www.boem.gov/renewable-energy/mapping-and-data/renewable-energy-gis-data, last access: 4 April 2023.

Burton, T., Jenkins, N., Sharpe, D., and Bossanyi, E.: Wind Energy Handbook, John Wiley & Sons, 784 pp., 2011.

Debnath, M., Doubrawa, P., Optis, M., Hawbecker, P., and Bodini, N.: Extreme wind shear events in US offshore wind energy areas and the role of induced stratification, Wind Energ. Sci., 6, 1043–1059, https://doi.org/10.5194/wes-6-1043-2021, 2021.

DNV: NYSERDA Floating LiDAR Buoy Data, Resource Panorama Public Data [data set], https://oswbuoysny.resourcepanorama.dnv.com/download/f67d14ad-07ab-4652-16d2-08d71f257da1 (last access: 6 July 2021), 2019.

Donlon, C. J., Martin, M., Stark, J., Roberts-Jones, J., Fiedler, E., and Wimmer, W.: The Operational Sea Surface Temperature and Sea Ice Analysis (OSTIA) system, Remote Sens. Environ., 116, 140–158, https://doi.org/10.1016/j.rse.2010.10.017, 2012.

EIA: Frequently Asked Questions (FAQs) – U.S. Energy Information Administration (EIA), https://www.eia.gov/tools/faqs/faq.php (last access: 4 April 2023), 2023.

FACT SHEET: Biden Administration Jumpstarts Offshore Wind Energy Projects to Create Jobs, https://www.whitehouse.gov/briefing-room/statements-releases/2021/03/29/fact-sheet-biden-administration-jumpstarts-offshore-wind-energy-projects-to-create-jobs/, last access: 4 April 2023.

Fischereit, J., Brown, R., Larsén, X. G., Badger, J., and Hawkes, G.: Review of Mesoscale Wind-Farm Parametrizations and Their Applications, Bound.-Lay. Meteorol., 182, 175–224, https://doi.org/10.1007/s10546-021-00652-y, 2022.

Fitch, A. C., Olson, J. B., Lundquist, J. K., Dudhia, J., Gupta, A. K., Michalakes, J., and Barstad, I.: Local and Mesoscale Impacts of Wind Farms as Parameterized in a Mesoscale NWP Model, Mon. Weather. Rev., 140, 3017–3038, https://doi.org/10.1175/MWR-D-11-00352.1, 2012.

Fitch, A. C., Lundquist, J. K., and Olson, J. B.: Mesoscale Influences of Wind Farms throughout a Diurnal Cycle, Mon. Weather Rev., 141, 2173–2198, https://doi.org/10.1175/MWR-D-12-00185.1, 2013.

Golbazi, M., Archer, C. L., and Alessandrini, S.: Surface impacts of large offshore wind farms, Environ. Res. Lett., 17, 064021, https://doi.org/10.1088/1748-9326/ac6e49, 2022.

Gupta, T. and Baidya Roy, S.: Recovery processes in a large offshore wind farm, Wind Energ. Sci., 6, 1089–1106, https://doi.org/10.5194/wes-6-1089-2021, 2021.

Hahmann, A. N., Sīle, T., Witha, B., Davis, N. N., Dörenkämper, M., Ezber, Y., García-Bustamante, E., González-Rouco, J. F., Navarro, J., Olsen, B. T., and Söderberg, S.: The making of the New European Wind Atlas – Part 1: Model sensitivity, Geosci. Model Dev., 13, 5053–5078, https://doi.org/10.5194/gmd-13-5053-2020, 2020.

Hersbach, H., Bell, B., Berrisford, P., Hirahara, S., Horányi, A., Muñoz-Sabater, J., Nicolas, J., Peubey, C., Radu, R., Schepers, D., Simmons, A., Soci, C., Abdalla, S., Abellan, X., Balsamo, G., Bechtold, P., Biavati, G., Bidlot, J., Bonavita, M., De Chiara, G., Dahlgren, P., Dee, D., Diamantakis, M., Dragani, R., Flemming, J., Forbes, R., Fuentes, M., Geer, A., Haimberger, L., Healy, S., Hogan, R. J., Hólm, E., Janisková, M., Keeley, S., Laloyaux, P., Lopez, P., Lupu, C., Radnoti, G., de Rosnay, P., Rozum, I., Vamborg, F., Villaume, S., and Thépaut, J.-N.: The ERA5 global reanalysis, Q. J. Roy. Meteor. Soc., 146, 1999–2049, https://doi.org/10.1002/qj.3803, 2020.

Hersbach, H., Bell, B., Berrisford, P., Biavati, G., Horányi, A., Muñoz Sabater, J., Nicolas, J., Peubey, C., Radu, R., Rozum, I., Schepers, D., Simmons, A., Soci, C., Dee, D., and Thépaut, J.-N.: ERA5 hourly data on pressure levels from 1940 to present, Copernicus Climate Change Service (C3S) Climate Data Store (CDS) [data set], https://doi.org/10.24381/cds.bd0915c6, 2023.

Iacono, M. J., Delamere, J. S., Mlawer, E. J., Shephard, M. W., Clough, S. A., and Collins, W. D.: Radiative forcing by long-lived greenhouse gases: Calculations with the AER radiative transfer models, J. Geophys. Res.-Atmos., 113, D13103, https://doi.org/10.1029/2008JD009944, 2008.

Jiang, Q.: Impact of Elevated Kevin-Helmholtz Billows on the Atmospheric Boundary Layer, J. Atmos. Sci., 1, 3983–3999, https://doi.org/10.1175/JAS-D-21-0062.1, 2021.

Kain, J. S.: The Kain–Fritsch Convective Parameterization: An Update, J. Appl. Meteorol. Clim., 43, 170–181, https://doi.org/10.1175/1520-0450(2004)043<0170:TKCPAU>2.0.CO;2, 2004.

Kusaka, H., Crook, A., Knievel, J. C., and Dudhia, J.: Sensitivity of the WRF Model to Advection and Diffusion Schemes for Simulation of Heavy Rainfall along the Baiu Front, SOLA, 1, 177–180, https://doi.org/10.2151/sola.2005-046, 2005.

Lauridsen, M. J. and Ancell, B. C.: Nonlocal Inadvertent Weather Modification Associated with Wind Farms in the Central United States, Adv. Meteorol., 2018, e2469683, https://doi.org/10.1155/2018/2469683, 2018.

Lee, J. C. Y. and Fields, M. J.: An overview of wind-energy-production prediction bias, losses, and uncertainties, Wind En-

erg. Sci., 6, 311–365, https://doi.org/10.5194/wes-6-311-2021, 2021.

Livingston, H. G. and Lundquist, J. K.: How many offshore wind turbines does New England need?, Meteorol. Appl., 27, e1969, https://doi.org/10.1002/met.1969, 2020.

Lundquist, J. K., DuVivier, K. K., Kaffine, D., and Tomaszewski, J. M.: Costs and consequences of wind turbine wake effects arising from uncoordinated wind energy development, Nature Energy, 4, 26–34, https://doi.org/10.1038/s41560-018-0281-2, 2019.

Mirocha, J. D., Kosovic, B., Aitken, M. L., and Lundquist, J. K.: Implementation of a generalized actuator disk wind turbine model into the weather research and forecasting model for large-eddy simulation applications, J. Renew. Sustain. Ener., 6, 013104, https://doi.org/10.1063/1.4861061, 2014.

Monin, A. S. and Obukhov, A. M.: Basic laws of turbulent mixing in the surface layer of the atmosphere, Tr. Akad. Nauk SSSR Geophiz. Inst., 24, 30, https://gibbs.science/efd/handouts/monin_obukhov_1954.pdf (last access: 28 November 2022), 1954.

Morrison, H., Thompson, G., and Tatarskii, V.: Impact of Cloud Microphysics on the Development of Trailing Stratiform Precipitation in a Simulated Squall Line: Comparison of One- and Two-Moment Schemes, Mon. Weather Rev., 137, 991–1007, https://doi.org/10.1175/2008MWR2556.1, 2009.

Muñoz-Esparza, D., Cañadillas, B., Neumann, T., and van Beeck, J.: Turbulent fluxes, stability and shear in the offshore environment: Mesoscale modelling and field observations at FINO1, J. Renew. Sustain. Ener., 4, 063136, https://doi.org/10.1063/1.4769201, 2012.

Musial, W., Heimiller, D., Beiter, P., Scott, G., and Draxl, C.: 2016 Offshore Wind Energy Resource Assessment for the United States, NREL/TP-5000-66599, https://doi.org/10.2172/1324533, 2016.

Nakanishi, M. and Niino, H.: An Improved Mellor–Yamada Level-3 Model: Its Numerical Stability and Application to a Regional Prediction of Advection Fog, Bound.-Lay. Meteorol., 119, 397–407, https://doi.org/10.1007/s10546-005-9030-8, 2006.

National Renewable Energy Laboratory: 2023 National Offshore Wind data set (NOW-23), National Renewable Energy Laboratory [data set], https://doi.org/10.25984/1821404, 2020.

NEISO: Energy, Load, and Demand Reports, ISO New England [data set], https://www.iso-ne.com/isoexpress/web/reports/load-and-demand/-/tree/dmnd-rt-hourly-sys (last access: 24 October 2022), 2019.

NEISO: Reliable Electricity. Competitive Prices. Clean-Energy Transition, https://www.iso-ne.com (last access: 10 January 2023), 2023.

Niu, G.-Y., Yang, Z.-L., Mitchell, K. E., Chen, F., Ek, M. B., Barlage, M., Kumar, A., Manning, K., Niyogi, D., Rosero, E., Tewari, M., and Xia, Y.: The community Noah land surface model with multiparameterization options (Noah-MP): 1. Model description and evaluation with local-scale measurements, J. Geophys. Res.-Atmos., 116, D12110, https://doi.org/10.1029/2010JD015139, 2011.

Nygaard, N. G.: Wakes in very large wind farms and the effect of neighbouring wind farms, J. Phys. Conf. Ser., 524, 012162, https://doi.org/10.1088/1742-6596/524/1/012162, 2014.

Optis, M., Bodini, N., Debnath, M., and Doubrawa, P.: Best Practices for the Validation of U.S. Offshore Wind Resource Models, National Renewable Energy Lab. (NREL), Golden, CO (United States), NREL/TP-5000-78375, https://doi.org/10.2172/1755697, 2020.

Perkins, S. E., Pitman, A. J., Holbrook, N. J., and McAneney, J.: Evaluation of the AR4 Climate Models' Simulated Daily Maximum Temperature, Minimum Temperature, and Precipitation over Australia Using Probability Density Functions, J. Climate, 20, 4356–4376, https://doi.org/10.1175/JCLI4253.1, 2007.

Platis, A., Siedersleben, S. K., Bange, J., Lampert, A., Bärfuss, K., Hankers, R., Cañadillas, B., Foreman, R., Schulz-Stellenfleth, J., Djath, B., Neumann, T., and Emeis, S.: First in situ evidence of wakes in the far field behind offshore wind farms, Sci. Rep., 8, 2163, https://doi.org/10.1038/s41598-018-20389-y, 2018.

Porté-Agel, F., Bastankhah, M., and Shamsoddin, S.: Wind-Turbine and Wind-Farm Flows: A Review, Bound.-Lay. Meteorol, 174, 1–59, https://doi.org/10.1007/s10546-019-00473-0, 2020.

Price-Whelan, A. M., Lim, P. L., Earl, N., Starkman, N., Bradley, L., Shupe, D. L., Patil, A. A., Corrales, L., Brasseur, C. E., Nöthe, M., Donath, A., Tollerud, E., Morris, B. M., Ginsburg, A., Vaher, E., Weaver, B. A., Tocknell, J., Jamieson, W., Kerkwijk, M. H. van, Robitaille, T. P., Merry, B., Bachetti, M., Günther, H. M., Authors, P., Aldcroft, T. L., Alvarado-Montes, J. A., Archibald, A. M., Bódi, A., Bapat, S., Barentsen, G., Bazán, J., Biswas, M., Boquien, M., Burke, D. J., Cara, D., Cara, M., Conroy, K. E., Conseil, S., Craig, M. W., Cross, R. M., Cruz, K. L., D'Eugenio, F., Dencheva, N., Devillepoix, H. A. R., Dietrich, J. P., Eigenbrot, A. D., Erben, T., Ferreira, L., Foreman-Mackey, D., Fox, R., Freij, N., Garg, S., Geda, R., Glattly, L., Gondhalekar, Y., Gordon, K. D., Grant, D., Greenfield, P., Groener, A. M., Guest, S., Gurovich, S., Handberg, R., Hart, A., Hatfield-Dodds, Z., Homeier, D., Hosseinzadeh, G., Jenness, T., Jones, C. K., Joseph, P., Kalmbach, J. B., Karamehmetoglu, E., Kałuszyński, M., Kelley, M. S. P., Kern, N., Kerzendorf, W. E., Koch, E. W., Kulumani, S., Lee, A., Ly, C., Ma, Z., MacBride, C., Maljaars, J. M., Muna, D., Murphy, N. A., Norman, H., O'Steen, R., Oman, K. A., Pacifici, C., Pascual, S., Pascual-Granado, J., Patil, R. R., Perren, G. I., Pickering, T. E., Rastogi, T., Roulston, B. R., Ryan, D. F., Rykoff, E. S., Sabater, J., Sakurikar, P., Salgado, J., Sanghi, A., Saunders, N., Savchenko, V., Schwardt, L., Seifert-Eckert, M., Shih, A. Y., Jain, A. S., Shukla, G., Sick, J., Simpson, C., Singanamalla, S., Singer, L. P., Singhal, J., Sinha, M., Sipőcz, B. M., Spitler, L. R., Stansby, D., Streicher, O., Šumak, J., Swinbank, J. D., Taranu, D. S., Tewary, N., Tremblay, G. R., de Val-Borro, M., Kooten, S. J. V., Vasović, Z., Verma, S., Cardoso, J. V. de M., Williams, P. K. G., Wilson, T. J., Winkel, B., Wood-Vasey, W. M., Xue, R., Yoachim, P., Zhang, C., and Zonca, A.: The Astropy Project: Sustaining and Growing a Community-oriented Open-source Project and the Latest Major Release (v5.0) of the Core Package, Astrophys. J., 935, 167, https://doi.org/10.3847/1538-4357/ac7c74, 2022.

Pronk, V., Bodini, N., Optis, M., Lundquist, J. K., Moriarty, P., Draxl, C., Purkayastha, A., and Young, E.: Can reanalysis products outperform mesoscale numerical weather prediction models in modeling the wind resource in simple terrain?, Wind Energ. Sci., 7, 487–504, https://doi.org/10.5194/wes-7-487-2022, 2022.

Pryor, S. C., Barthelmie, R. J., and Shepherd, T. J.: Wind power production from very large offshore wind farms, Joule, 5, 2663–2686, https://doi.org/10.1016/j.joule.2021.09.002, 2021.

Redfern, S., Olson, J. B., Lundquist, J. K., and Clack, C. T. M.: Incorporation of the Rotor-Equivalent Wind Speed into the Weather Research and Forecasting Model's Wind Farm Parameterization, Mon. Weather Rev., 147, 1029–1046, https://doi.org/10.1175/MWR-D-18-0194.1, 2019.

Redfern, S., Optis, M., Xia, G., and Draxl, C.: Offshore wind energy forecasting sensitivity to sea surface temperature input in the Mid-Atlantic, Wind Energ. Sci., 8, 1–23, https://doi.org/10.5194/wes-8-1-2023, 2023.

Rosencrans, D.: mid-Atlantic_namelists, Zenodo [code], https://doi.org/10.5281/zenodo.7374239, 2021.

Rosencrans, D.: mid-Atlantic_turbines, Zenodo [code], https://doi.org/10.5281/zenodo.7374283, 2022.

Rybchuk, A., Juliano, T. W., Lundquist, J. K., Rosencrans, D., Bodini, N., and Optis, M.: The sensitivity of the Fitch wind farm parameterization to a three-dimensional planetary boundary layer scheme, Wind Energ. Sci., 7, 2085–2098, https://doi.org/10.5194/wes-7-2085-2022, 2022.

Schneemann, J., Rott, A., Dörenkämper, M., Steinfeld, G., and Kühn, M.: Cluster wakes impact on a far-distant offshore wind farm's power, Wind Energ. Sci., 5, 29–49, https://doi.org/10.5194/wes-5-29-2020, 2020.

Shapiro, C. R., Gayme, D. F., and Meneveau, C.: Filtered actuator disks: Theory and application to wind turbine models in large eddy simulation, Wind Energy, 22, 1414–1420, https://doi.org/10.1002/we.2376, 2019.

Siedersleben, S. K., Platis, A., Lundquist, J. K., Djath, B., Lampert, A., Bärfuss, K., Cañadillas, B., Schulz-Stellenfleth, J., Bange, J., Neumann, T., and Emeis, S.: Turbulent kinetic energy over large offshore wind farms observed and simulated by the mesoscale model WRF (3.8.1), Geosci. Model Dev., 13, 249–268, https://doi.org/10.5194/gmd-13-249-2020, 2020.

Skamarock, W. C., Klemp, J. B., Dudhia, J., Gill, D. O., Liu, Z., Berner, J., Wang, W., Powers, J. G., Duda, M. G., and Barker, D. M.: A description of the advanced research WRF model version 4, NCAR/TN–556+ STR, https://doi.org/10.5065/1dfh-6p97, 2019.

Stevens, R. J. A. M., Gayme, D. F., and Meneveau, C.: Effects of turbine spacing on the power output of extended wind-farms, Wind Energy, 19, 359–370, https://doi.org/10.1002/we.1835, 2016.

Stoelinga, M., Sanchez-Gomez, M., Poulos, G. S., and Crescenti, J.: Estimating Long-Range External Wake Losses in Energy Yield and Operational Performance Assessments Using the WRF Wind Farm Parameterization, 20, https://arcvera.com/wp-content/uploads/2022/08/ArcVera-White-Paper-Estimating-Long-Range-External-Wake-Losses-WRF-WFP-1.0.pdf (last access: 2 January 2022), 2022.

Thompson, G., Field, P. R., Rasmussen, R. M., and Hall, W. D.: Explicit Forecasts of Winter Precipitation Using an Improved Bulk Microphysics Scheme. Part II: Implementation of a New Snow Parameterization, Mon. Weather Rev., 136, 5095–5115, https://doi.org/10.1175/2008MWR2387.1, 2008.

Tomaszewski, J. M. and Lundquist, J. K.: Simulated wind farm wake sensitivity to configuration choices in the Weather Research and Forecasting model version 3.8.1, Geosci. Model Dev., 13, 2645–2662, https://doi.org/10.5194/gmd-13-2645-2020, 2020.

Vanderwende, B. J., Kosoviæ, B., Lundquist, J. K., and Mirocha, J. D.: Simulating effects of a wind-turbine array using LES and RANS, J. Adv. Model. Earth Sy., 8, 1376–1390, https://doi.org/10.1002/2016MS000652, 2016.

Virtanen, P., Gommers, R., Oliphant, T. E., Haberland, M., Reddy, T., Cournapeau, D., Burovski, E., Peterson, P., Weckesser, W., Bright, J., van der Walt, S. J., Brett, M., Wilson, J., Millman, K. J., Mayorov, N., Nelson, A. R. J., Jones, E., Kern, R., Larson, E., Carey, C. J., Polat, Ý., Feng, Y., Moore, E. W., VanderPlas, J., Laxalde, D., Perktold, J., Cimrman, R., Henriksen, I., Quintero, E. A., Harris, C. R., Archibald, A. M., Ribeiro, A. H., Pedregosa, F., and van Mulbregt, P.: SciPy 1.0: fundamental algorithms for scientific computing in Python, Nat. Methods, 17, 261–272, https://doi.org/10.1038/s41592-019-0686-2, 2020.

Viselli, A., Faessler, N., and Filippelli, M.: Analysis of Wind Speed Shear and Turbulence LiDAR Measurements to Support Offshore Wind in the Northeast United States, ASME 2018 1st International Offshore Wind Technical Conference, https://doi.org/10.1115/iowtc2018-1003, 2018.

Volker, P. J. H., Badger, J., Hahmann, A. N., and Ott, S.: The Explicit Wake Parametrisation V1.0: a wind farm parametrisation in the mesoscale model WRF, Geosci. Model Dev., 8, 3715–3731, https://doi.org/10.5194/gmd-8-3715-2015, 2015.

W.F. Baird & Associates: Vessel Navigation Through the Proposed Rhode Island/Massachusetts and Massachusetts Wind Energy Areas, https://static1.squarespace.com/static/5a2eae32be42d64ed467f9d1/t/5dd3d3e476d4226b2a83db25/1574163438896/Proposed+1x1+layout+from+RI-MA+Leaseholders+1+Nov+19+%281%29.pdf (last access: 5 April 2022), 2019.

Wu, C., Luo, K., Wang, Q., and Fan, J.: A refined wind farm parameterization for the weather research and forecasting model, Appl. Energ., 306, 118082, https://doi.org/10.1016/j.apenergy.2021.118082, 2022.

Xia, G., Draxl, C., Optis, M., and Redfern, S.: Detecting and characterizing simulated sea breezes over the US northeastern coast with implications for offshore wind energy, Wind Energ. Sci., 7, 815–829, https://doi.org/10.5194/wes-7-815-2022, 2022.

scientific reports

Check for updates

OPEN

Accelerating deployment of offshore wind energy alter wind climate and reduce future power generation potentials

Naveed Akhtar✉, Beate Geyer, Burkhardt Rockel, Philipp S. Sommer & Corinna Schrum

The European Union has set ambitious CO_2 reduction targets, stimulating renewable energy production and accelerating deployment of offshore wind energy in northern European waters, mainly the North Sea. With increasing size and clustering, offshore wind farms (OWFs) wake effects, which alter wind conditions and decrease the power generation efficiency of wind farms downwind become more important. We use a high-resolution regional climate model with implemented wind farm parameterizations to explore offshore wind energy production limits in the North Sea. We simulate near future wind farm scenarios considering existing and planned OWFs in the North Sea and assess power generation losses and wind variations due to wind farm wake. The annual mean wind speed deficit within a wind farm can reach 2–2.5 ms^{-1} depending on the wind farm geometry. The mean deficit, which decreases with distance, can extend 35–40 km downwind during prevailing southwesterly winds. Wind speed deficits are highest during spring (mainly March–April) and lowest during November–December. The large-size of wind farms and their proximity affect not only the performance of its downwind turbines but also that of neighboring downwind farms, reducing the capacity factor by 20% or more, which increases energy production costs and economic losses. We conclude that wind energy can be a limited resource in the North Sea. The limits and potentials for optimization need to be considered in climate mitigation strategies and cross-national optimization of offshore energy production plans are inevitable.

The increasing demand for carbon–neutral energy production has fostered the rapidly increasing deployment of offshore wind farms (OWFs). The construction of OWFs is generally 1.5–2 times more expensive than onshore wind farms[1]. Additionally, their maintenance/repair, power network, and obtaining observational data for optimization are more challenging and costlier[2]. Although OWFs are more expensive in construction and maintenance than onshore wind farms, these costs are offset to some extent by the higher capacity factor (CF) of OWFs due to the strength of offshore wind resources[3]. About 10 km off the coast, sea surface winds are generally 25% higher than onshore winds. These high offshore wind resources can be utilized 2–3 times longer to generate electricity than onshore wind farms in the same period of time[4,5]. Europe's total installed OWF capacity reached 22 GW in 2019; of that capacity, 77% is installed in the North Sea[6]. As part of the ambitious plans of the EU to reach climate neutrality a significant increase to 450 GW total offshore wind energy capacity is intended by 2050[7]. About 47% (212 GW) of these will be installed in the North Sea at an annual consenting rate of 8.8 GW per year during the 2020s[8]. This implies that the North Sea forms one of the worldwide hotspots of OWF development. Figure 1 shows the planning status of OWFs in the North Sea by 2019[9]. These massive developments are motivated by the strong and reliable wind resources in the North Sea at shallow water depths.

Wind farms are usually clustered around transmission lines to minimize deployment and operating costs. Hence, in addition to the quality of wind resources also the transmission lines determine whether a location is optimal for a wind farm. Despite the considerable availability of wind resources, evidence suggests that wake effects, which manifest as a downwind reduction in wind speed, can undermine the potential of cost-efficient wind energy production[10–12]. The efficiency limits that can arise from clustering and the overall regional saturation might limit the offshore wind energy production. These important questions at regional and longer times scales remain yet unassessed and need detailed scientific analysis for an efficient climate mitigation strategy.

Institute of Coastal Systems-Analysis and Modeling, Helmholtz-Zentrum Hereon, Geesthacht, Germany. ✉email: [redacted]@hereon.de

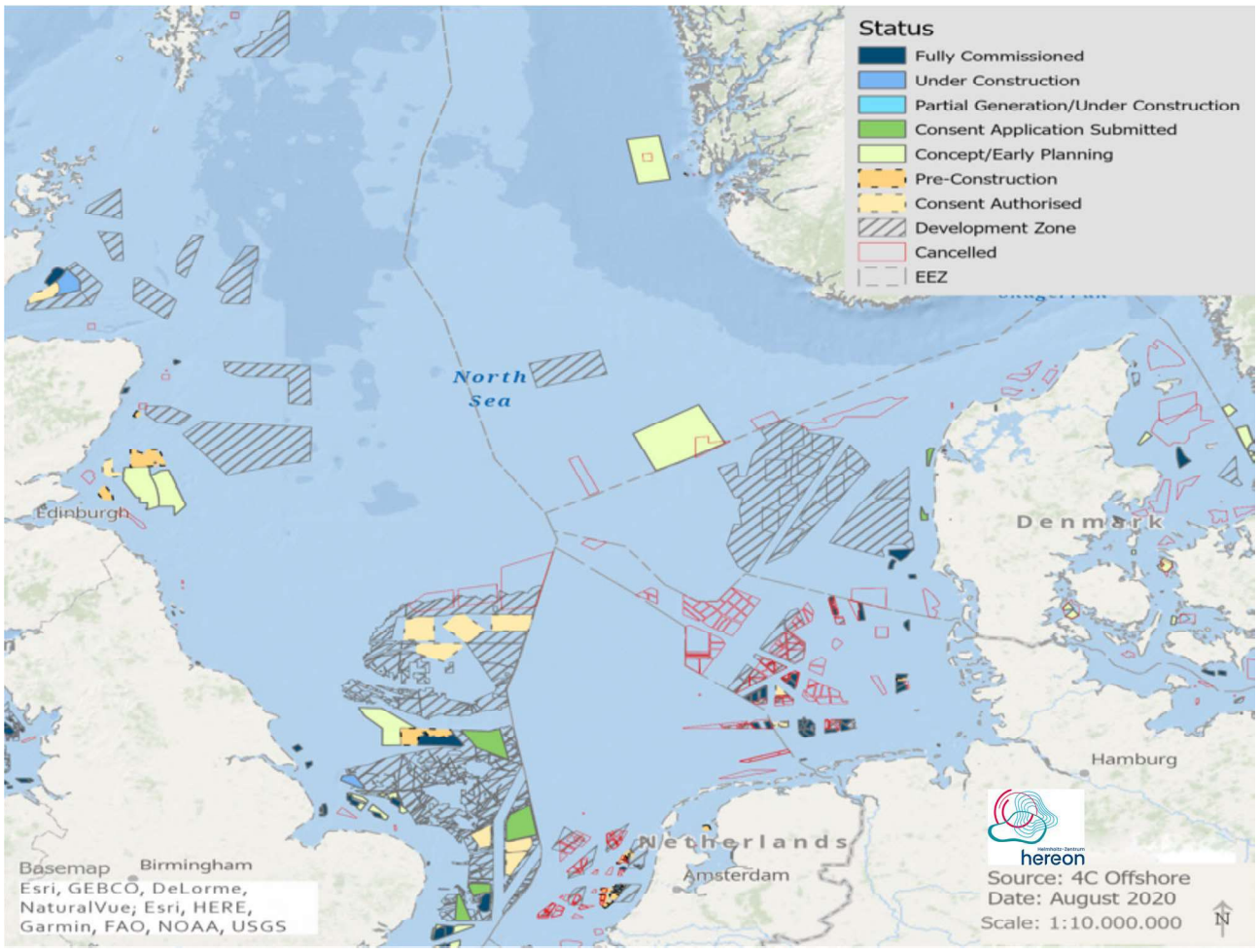

Figure 1. Distribution of OWFs in the North Sea (4c Offshore. https://www.4coffshore.com/windfarms/, 2019). Colors indicate the planning status of the OWFs by 2019. This map was created by Ulrike Kleeberg with ArcGIS Pro 10.7 (ESRI Inc. ArcGIS Pro 10.7, 2019).

Additionally, in order to develop the OWFs efficiently and accurately, a comprehensive evaluation of the wind resources is required.

Wind turbines extract kinetic energy (KE) from the atmosphere and convert part of that energy into electric power. The remaining part of the energy is converted into turbulent kinetic energy (TKE); that generates wakes (downwind wind speed deficits)[13–17]. Airborne observations show that TKE is significantly increasing (factor of 10–20) above the wind farms[17]. These observations also show that wind farm wakes can extend up to 50–70 km under stable atmospheric conditions[18]. These wakes further impact the efficiency of downwind wind farms through changes in the temperature and turbulence in the boundary layer[19]. At a given wind speed, colder and denser air masses provide more energy than warmer and lighter air masses. Moreover, atmospheric turbulence additionally reduces the energy output and increases the load on wind farm structures and equipment[19]. Observational evidence shows that wakes can increase the temperature by 0.5 °C and humidity by 0.5 g per kilogram at hub height, even as far as 60 km downwind of wind farms[20]. Case studies related to wake dynamics have largely been limited to single wind turbines[21,22] and/or individual wind farms[23–26]. Only a few studies have analyzed the wake effects caused by neighboring wind farms[11,25,27]. In a recent study[11], the authors highlighted the economic losses suffered by onshore downwind wind farms due to the wake effects of upwind wind farms. Estimates of the wake effects on power production and environmental changes have been limited to short timescales (on the order of a few days or to a specific year[28]) and only one or two wind farms. The aforementioned studies emphasize the need to better understand the physical and economic interactions of large wind farms with complex clustered layouts (such as those planned in the North Sea) to ensure the efficient utilization of wind energy resources.

Building on process understanding of case studies, we assess for the first time the wake effect on the power production of both existing and planned large OWFs on a regional scale for the North Sea over a period of 10 years. It allows us to take into account the natural variability in wind climate, as inter-annual variability plays an important role in wind energy[29]. We perform two high-resolution numerical scenario simulations for a multi-year simulation period, one considering existing and currently planned OWFs in the North Sea and one for the undisturbed atmosphere. For the future scenario simulation, we apply a generic wind farm parameterization considering energy extraction and turbulence effects using a standard wind farm configuration, which we validate

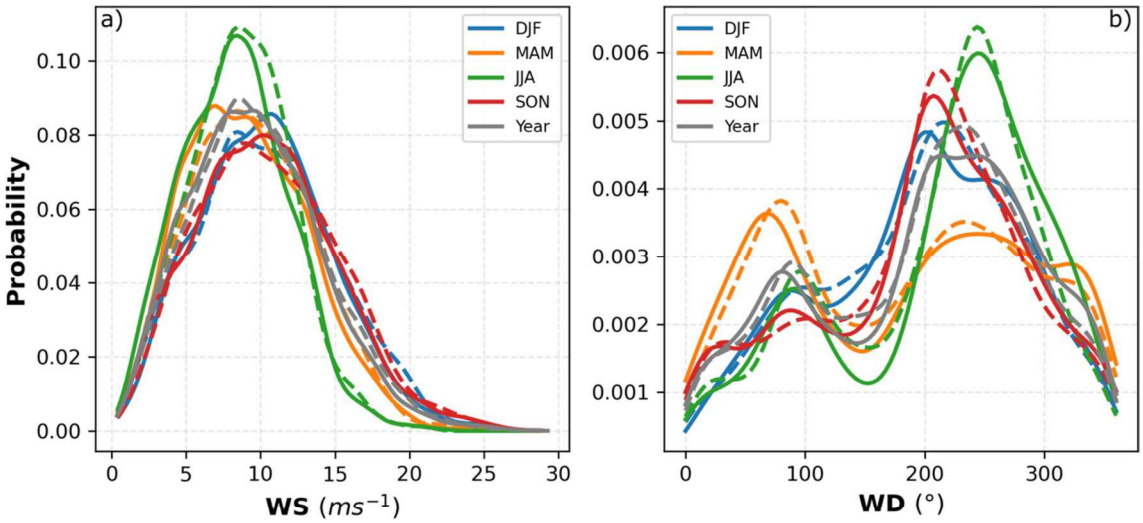

Figure 2. Annual and seasonal probability density functions calculated using the hourly (**a**) wind speed and (**b**) wind direction data at FINO1 (6.5875°E and 54.01472°N) at a height of 90 m in the period 2008–2009. Dashed lines result from measurements, while solid lines are from COSMO-CLM simulation. Gray lines indicate data for the entire period whereas colors indicate the different seasons as given in the legend.

against earlier published high-resolution observations[30] to ensure the realism of the scenario simulation. Mean wind changes will be analyzed and efficiency loss in offshore energy production will be estimated in terms of the Capacity Factor (CF) deficiency. Given the ongoing development of OWFs in the North Sea, our study highlights the urgent need to consider feedbacks between existing and planned OWFs to assess physical and economic impacts to optimize planning and to assess the limits and environmental impacts of industrial offshore energy production. To the best of our knowledge, this is the first study to estimate the wind speed deficits due to OWF production at a basin-wide scale covering a multi-year period and to investigate the effect of these deficits on the CF of wind farms. Furthermore, in this study, we evaluated the wind farm parameterization for real case simulations against the observations.

Experimental design

All existing and planned OWFs by 2015[31] in the North Sea area (see Fig. SI 1, the latest planning status is shown in Fig. 1) are considered for the scenario simulations. We focus on the Central and Southern North Sea where OWFs are planned close to each other. The scenario simulations are carried out for a multi-year period from 2008 to 2017, to account for a range of different weather conditions to assess the impact of large-scale OWF development on the production potential of wind farms. For the numerical simulations, we use the high-resolution Consortium for Small-Scale Modeling (COSMO)-CLimate Mode (CLM) regional climate model (RCM)[32] both without and with a wind farm parameterization. An existing wind farm parameterization[15,16,33,34] for a standard turbine size has been implemented into COSMO-CLM to include the effects of wind farms; these RCM simulations provide us with high-resolution spatiotemporal estimates of the wind speed over wind farm areas. A CF model[35] has been used to assess the average energy production of wind farms based on wind speed. Several factors can influence the CF, such as the wake effect, turbine efficiency, and offshore distance[36]. For the intercomparison of scenario simulations, we consider the impact of wakes on the CF, to illustrate the potential impact of feedbacks between wind farm deployment and regional atmospheric conditions. Hereafter, "CCLM_WF" and "CCLM" refer to the COSMO-CLM simulations with and without a wind farm parameterization, respectively.

Verification of the simulated wind fields and OWFs wakes

Comparison with the point observations of wind fields. To verify the realism of our scenario simulation, a detailed validation against published data[30,37] was performed. The simulated wind characteristics over the North Sea can be directly evaluated using data from the research platforms[37] FINO1 (6.5875°E, 54.01472°N) and FINO3 (7.158333°E, 55.195°N) starting in 2004 and 2009, respectively. The high quality of the mast-corrected measurement data allows for a detailed analysis of both the wind speed and the wind direction. Here we compared the FINO1 and FINO3 measurements with CCLM simulations for the period 2008–2009 and 2009–2014 respectively to avoid the effects of the OWF Alpha Ventus and DanTysk on the mast measurements[38]. The annual and seasonal probability density functions (PDFs) derived from hourly values of the wind speed and wind direction are in good agreement with the FINO1 data (Fig. 2). The annual and seasonal biases, root mean square error (RMSE), correlation coefficients, and Perkins' score (PS)[39] calculated between the CCLM simulation results and observations (FINO1 and FINO3) are presented in Tables 1 and 2. Compared with the FINO1 data, the CCLM winds show small, mostly negative biases of 0.27 ms^{-1} with simulated wind speeds that are lower than the observed wind speeds. During the spring and summer season model bias become stronger, along with higher RMSE values (Table 1). The autumn correlations of 0.87 are slightly higher than those in the other seasons. The PS of the yearly mean simulated wind speed is 0.95, with the highest values during winter (0.92) and the

	Bias		RMSE		CORR		PS	
	WS (ms^{-1})	WD (°)	WS (ms^{-1})	WD (°)	WS	WD	WS	WD
Yearly	−0.27	3.07	2.81	70.11	0.79	0.71	0.95	0.92
DFJ	−0.08	1.44	3.41	64.61	0.73	0.71	0.92	0.88
MAM	−0.34	1.21	2.54	76.53	0.82	0.72	0.85	0.77
JJA	0.40	8.08	2.73	72.18	0.72	0.67	0.79	0.80
SON	−0.25	1.40	2.49	65.89	0.87	0.73	0.91	0.87

Table 1. Yearly and seasonal mean wind speed and wind direction bias (CCLM – FINO1), root mean square error (RMSE), correlation (CORR), and Perkin's score (PS) of CCLM compared with FINO1 in the period 2008–2009.

	Bias		RMSE		CORR		PS	
	WS (ms^{-1})	WD (°)	WS (ms^{-1})	WD (°)	WS	WD	WS	WD
Yearly	−0.39	−6.34	2.59	67.01	0.85	0.75	0.95	0.93
DFJ	−0.54	−7.95	2.60	55.91	0.87	0.81	0.92	0.88
MAM	−0.40	−9.12	2.55	70.32	0.84	0.77	0.73	0.80
JJA	−0.30	−0.45	2.72	79.92	0.75	0.63	0.62	0.78
SON	−0.37	−7.99	2.50	58.11	0.85	0.79	0.81	0.89

Table 2. Yearly and seasonal mean wind speed and wind direction bias (CCLM – FINO3), root mean square error (RMSE), correlation (CORR), and Perkin's score (PS) of CCLM compared with FINO3 in the period 2009–2014.

lowest values during summer (0.79). The simulated CCLM wind direction PDFs are also well represented; the prevailing southwesterly (200°–280°) wind directions are effectively captured (Fig. 2). On average, the CCLM-simulated wind directions show a positive bias of 3.07°, a small counterclockwise shift with an RMSE of 70.11° and a correlation coefficient of 0.71 (Table 1). Again, the simulated summer values show larger deviations from the observations with a bias of 8.08° and an RMSE of 72.18°; in addition, the correlation coefficient is lower than those in the other seasons. The simulated wind direction shows the highest PS during winter (0.88) and the lowest PS during spring (0.77) with a yearly value of 0.92. The simulated wind direction relative to FINO3 shows a negative bias of −6.34°, an RMSE of 67.01°, a correlation coefficient of 0.75, and a PS of 0.93 (Table 2). Studies show that the existing wind farms in the North Sea are already affecting the wind field reaching FINO1 and FINO3[38]. A comparison of the wind speed and direction between CCLM_WF and FINO1 shows that the construction of planned wind farms will further affect their measurements in the future (Fig. SI 2). The annual and seasonal probability density functions (PDFs) derived from hourly values of the wind speed and wind direction are also in good agreement with the FINO3 data (Table 2 and Fig. SI 3).

Wake effects in case studies: evaluation of CCLM. For the sake of completeness, CCLM_WF has been evaluated against airborne campaign data[18] to illustrate the ability of CCLM_WF to simulate upwind flow and the spatial extent of wakes generated by wind farms. Here, we choose two different cases. In the first case, we evaluate the wake extent of the Amrumbank West wind farm; in the second case, we evaluated the wind speed deficit over the two Godewind farms. Only operational wind farms at the measurement times are considered in these simulations. Figure SI 4 shows the model domain and the wind farm locations.

Case 10 September 2016. A detailed comparison is performed for the wakes observed downwind of the Amrumbank West, Meerwind SüdOst, and Nordsee Ost wind farms with model simulations. The wake was measured during an aircraft campaign on 10 September 2016 between 0800 to 1100 UTC using five flight legs of 5 km, 15 km, 25 km, 35 km, and 45 km downwind of the Amrumbank West wind farm[18,30]. Stable atmospheric conditions and a wake extent of at least 45 km were measured. The installed turbines in Amrumbank West have a 90 m hub height and 120 m rotor diameter[12]. For this experiment, we employ only those wind farms which were existing at the time of measurements (see Fig. SI 4).

The simulated spatial extent of the wake agrees well with the measurement. Figure 3 shows the wake extents simulated in CCLM_WF (interpolated on the aircraft track) and airborne observations (see Fig. SI 5a for a complete snapshot of the wind speed field simulated in CCLM_WF and its difference from the observation). Both the observations and the simulations show a wake extending more than 45 km downwind of the wind farm. The simulation shows that the wake reached down to the Butendiek wind farm, located 50 km downwind of the Amrumbank West wind farm. However, the simulated wind direction is slightly rotated counterclockwise. Similar to the width of the wind farms, the wake width is approximately 12 km at the beginning, which expands and weakens as the distance increases from the generating wind farm. The transect of the simulated and observed wind speeds through the first flight leg of 5 km downwind of the wind farm shows that the simulated-observed

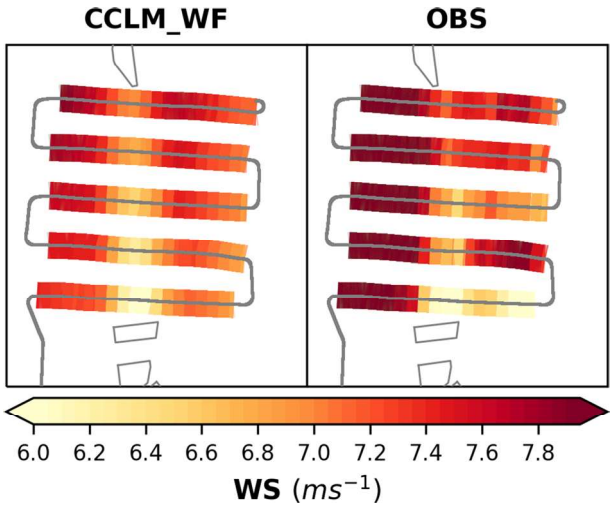

Figure 3. Wind speed at 90 m hub height (**a**) simulated in CCLM_WF and (**b**) observed by aircraft measurements. The aircraft track (gray lines) shown here ranged from 0820 to 0924 UTC on 10 September 2016. The model simulations show the wind speed at 0900 UTC.

differences are smaller inside the wake than outside (Fig. SI 5b). In general, the model slightly underestimates the wind speed compared to the observations.

Case 14 October 2017. In the chosen case, we evaluate the wind speed at a height of 250 m over Godewind farms 1 and 2 with aircraft observations. The installed turbines in these wind farms have a 110 m hub height and 153 m diameter[18]. For this experiment, we employ the wind farm location data as in Fig. SI 4; however, we used the turbine dimensions as installed in Godewind farms.

Figure 4 shows the wind speeds at 1500 UTC on 14 October 2017 over the Godewind farms simulated in CCLM_WF (interpolated on the aircraft track) and observed wind speeds (see Fig. SI 6a for a complete snapshot of the wind speed field simulated in CCLM_WF and its difference from the observation). Stable atmospheric conditions were observed at the times of the measurements[18]. An observed speed-up around the wind farms is well reproduced in the simulations. The simulated wind speeds agree better with the observations inside the wake than outside (Fig. SI 6b).

Due to the relatively coarse horizontal resolution of RCMs (1–2 km), the effects of individual wind turbines (with a rotor span of 120 or 153 m) cannot be fully resolved. Therefore, the simulated wake effects of the wind turbine can be underestimated, and thus, the wake effects of wind farms can be underestimated. In the present wind farm parameterization[16], the power produced by the wind turbine depends on the wind speed in the grid cell at the model level interacting with the rotor. The wind turbine removes momentum from the rotor-interacting layers to produce the power that leads to wind speed deficits in downwind grid cells.

The evaluation results show that COSMO-CLM with a wind farm parameterization realistically reproduces the effects of wind farms. The spatiotemporal variability of the wake effects and their impact on the CF of the wind farms at 90 m hub height are analyzed for the period 2008–2017 in the following sections.

Wake effect on wind speed and turbulent kinetic energy

Our simulations show that the development of massive clustered OWFs significantly impacts the wind climate and efficiency of renewable energy production on a regional scale. The reduction in the annual mean wind speed reaches up to 2–2.5 ms^{-1} during prevailing southwesterly (200°–280°) winds, and that in the seasonal mean reaches more than 3 ms^{-1} (see Fig. 5 and Figs. SI 2 and SI 8).

The wind speed in the North Sea exhibits strong spatial and temporal variability. At 90 m hub height, the wind speed varies seasonally, with a minimum of approximately 7–8.5 ms^{-1} in summer and a maximum of 10–11.5 ms^{-1} in winter (Fig. SI 7). The presence of a wind farm impacts the boundary layer flow over the wind farm and its vicinity by extracting KE from the mean flow and generating TKE. The highest wind speed deficit in the annual mean is about −18%, and the increase in TKE is nearly a factor of 4 over the wind farm itself (Fig. 6). These changes in wind speed and TKE extend vertically to a height of approximately 500 m (about 350 m above the turbine height). A deficit/raise of about 1 ms^{-1}/0.6 m^{-2} s^{-2} in wind speed/TKE extends to a height of approximately 200 m. The maximum change in wind speed and TKE found in the atmospheric levels between the hub (90 m) and tip height (153 m) of the wind turbines. The change in the wind speed and TKE above the turbine height is consistent with the previous studies[16,40,41]. The wind speed deficits are higher during spring (−22%) and summer (−20.8%) than during the other seasons (see also Fig. SI 8), the reason for which is explained later in this section. The increase in the TKE is found higher during winter (factor of 3.2) and autumn (factor of 3.8). The addition TKE source in the wind farm parameterization improves the representation of mixing and wind speed deficit during stable conditions[17]. The change in wind speed and TKE increases the boundary layer height[16].

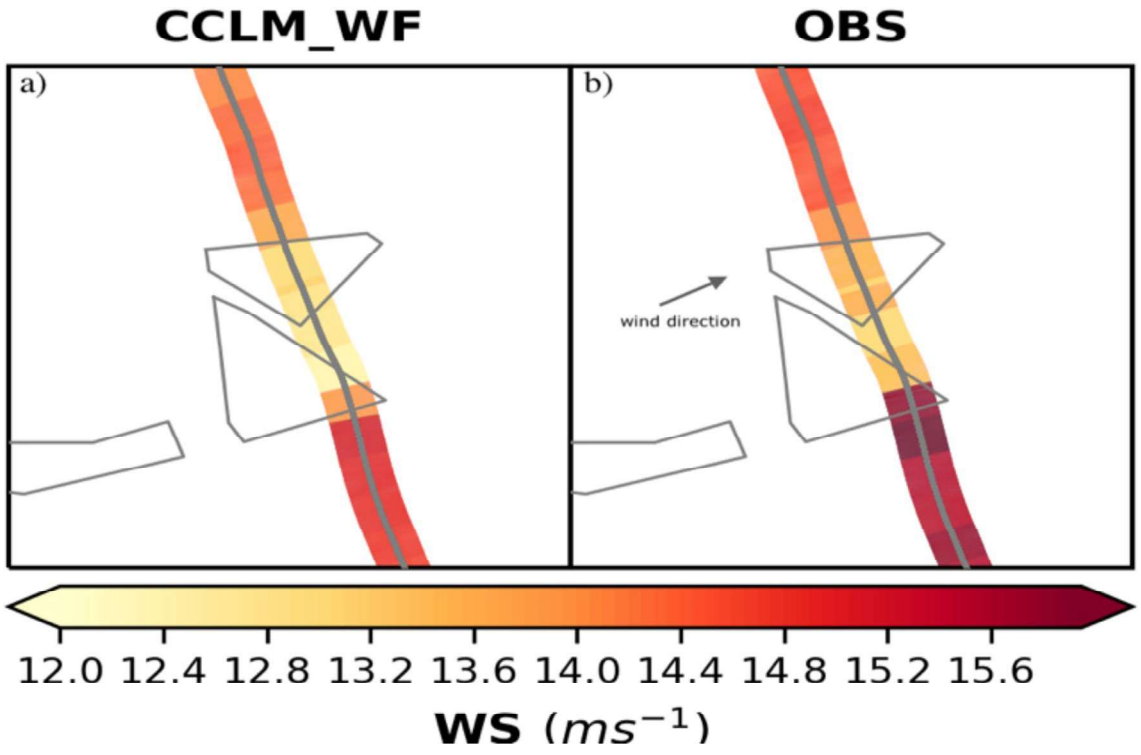

Figure 4. Wind speed at a height of 250 m (**a**) simulated in CCLM_WF and (**b**) observed by aircraft measurements. The aircraft track shown here ranged from 1445 to 1500 UTC on 14 October 2017. Arrow indicates the wind direction. The model simulations show the wind speed at 1500 UTC.

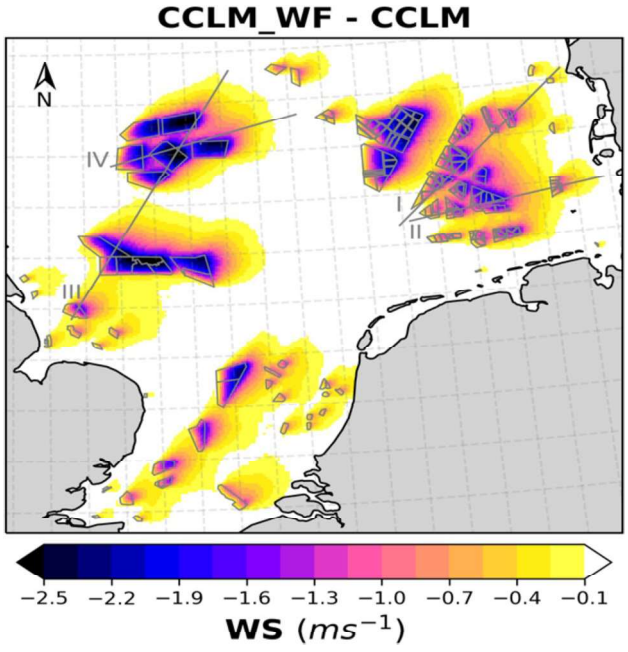

Figure 5. Annual mean wind speed deficits (CCLM_WF – CCLM) outside and inside the wind farms for the prevailing wind directions of 200°–280° at hub height (90 m) in the period 2008–2017. Numbered gray lines indicate the transects used for calculations of Fig. 8 and Fig. SI 6 and SI 7. This figure was created with Matplotlib (Hunter, J. D., Matplotlib: a 2D graphics environment. Computing in Science and Engineering 9, 2007) and Cartopy (Met office, Cartopy: a cartographic python library with a matplotlib interface. Exeter, Devon, https://scitools.org.uk/cartopy, 2015).

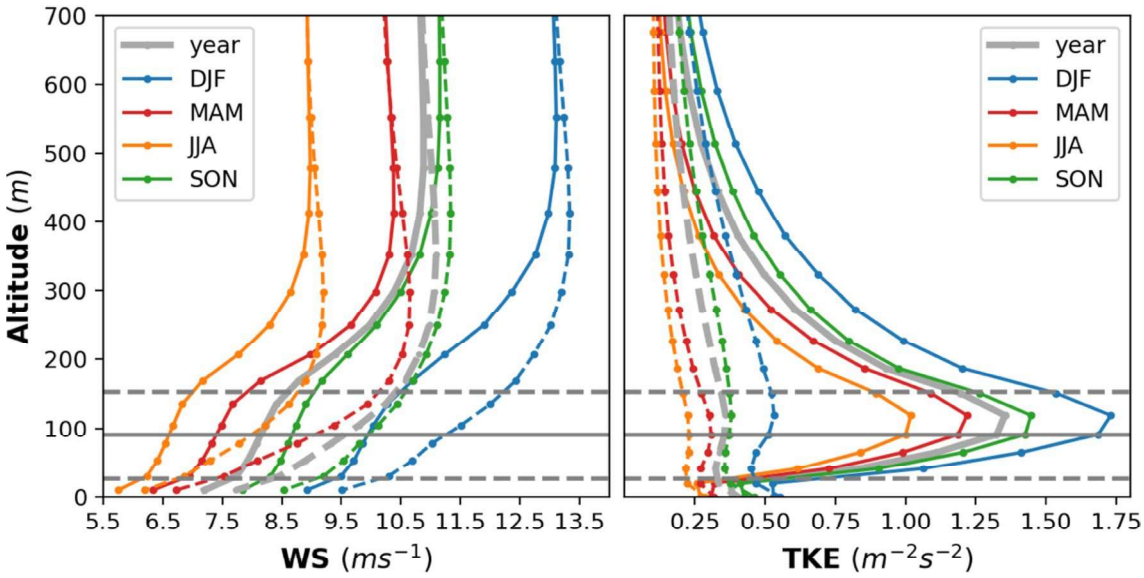

Figure 6. Annual and seasonal mean vertical profiles of the wind speed (left) and turbulent kinetic energy (right) simulated by CCLM (broken dotted lines) and CCLM_WF (solid dotted line) over the wind farm areas in the period 2008–2017. Solid circles indicate the model levels. The horizontal solid gray line indicates the hub height (90 m) of the turbine whereas dotted gray lines indicate lower (27 m) and upper (153 m) tip of the rotor.

Wakes, i.e., downwind reductions in wind speed, exhibit significant spatial variability inside and outside wind farms (Fig. 5). The wind speed deficit inside a wind farm increases with increasing distance from the upstream edge, reaching a maximum of 2–2.5 ms^{-1}. In an idealized numerical study, a maximum reduction of approximately 16% in the wind speed and increase in TKE by nearly a factor of 7 was estimated at hub height over a 10×10 km wind farm[16]. Here we used a realistic climate set up to study a scenario with clustered and large-scale wind farms and found larger mean wind speed deficits of approximately 18–20% of the annual mean wind. In our case, the increase in the mean TKE within the wind farm is almost a factor of 3 less than that reported (factor of 7) in the idealized study[16]. This could be due to the reason that mean values of TKE over a longer period 2008–2017 are shown here.

The wind farm induced boundary layer mixing, air friction, turbulence and weaken stratification effects within and above the rotor area that reach about 600 m. The maximum differences are found in the layers between the hub and tip height of the turbine. The reduction in the wind speed extends highest during spring when the atmospheric conditions are generally stable. The increase in TKE leads to the mixing of more momentum from aloft[15,24]. This mechanism is more pronounced during winter and autumn when atmospheric conditions are generally unstable in the North Sea. The strength of the TKE depends on the difference between the power coefficient and thrust coefficients which varies with the wind speed.

The wakes forming downwind extend over large distances and influence the wind climate at surrounding wind farms. The wake extends varies, it depends on wind speed and atmospheric stratification and might extend up to 70 km downwind[11,18,20]. On average wakes extend ca 40–45 km downwind (Fig. SI 8).

Implications for the CF

The downwind speed reduction results in a significant decrease in the efficiency of energy production here illustrated in terms of the CF. The wake induced decrease in CF up to 22% in the annual mean and up to 26% for the seasonal mean with the highest values at the downwind edge within the wind farms during southwesterly wind directions (see Fig. 7 and Figs. SI 4 and SI 5). Outside of the wind farms, these values decrease as the distance from the wind farms is increasing. A decrease of about 1% has been noted at a distance of 35–40 km in annual means during southwesterly wind directions. The highest drops are observed for the large wind farms in the German Bight and the UK's Dogger Bank for southwesterly wind directions (Fig. 7).

Without the wind farms, the annual mean CF for all wind directions varies spatially in the North Sea from 50 to 62%, with higher values during winter (65–70%) and lower values in summer (37–50%, Fig. SI 9). These values are strongly reduced in the areas where the large-size wind farms are clustered. The mean wind speed deficits and CF losses for all wind directions show that the wake effect extends more towards the northeast than in the other wind directions, indicating the dominance of southwesterly winds (Fig. SI 8 and Fig. SI 10).

A more specific analysis of the implications of large wind farm clusters and extremely large farms for the efficiency of neighboring farms and clusters in the area of the German Bight and the Dogger Bank (Fig. SI 1) highlights substantial CF losses. Figure 8 shows the annual and seasonal mean wind speed deficits and CF losses through the wind farms on two of the transects (gray lines I and III) shown in Fig. 5 in the case of prevailing winds in the German Bight and the UK's Dogger Bank. The wind farms in both of these areas are large and are located spatially close to each other. These transects show the strong horizontal influences of the wind farms together with the reductions in the wind speed and CF. Mean CF and wind speed show characteristic patterns

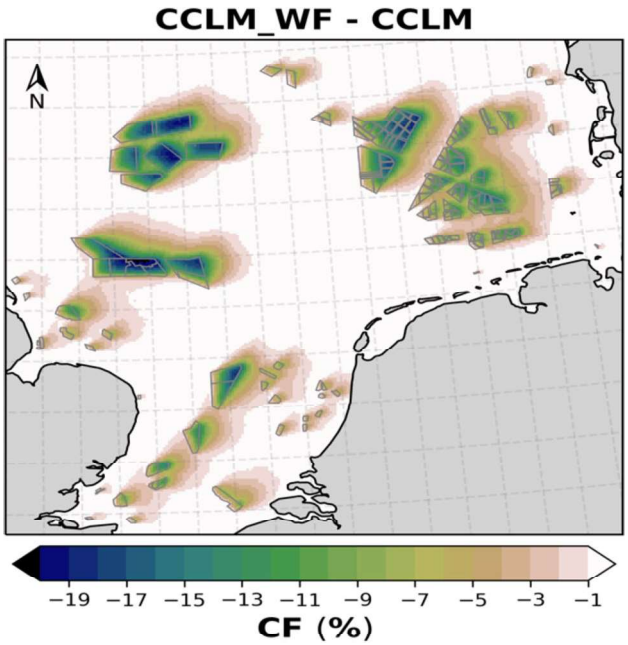

Figure 7. Annual mean losses in the capacity factor CF (CCLM_WF – CCLM) out- and inside of the wind farms (gray lines) for the prevailing wind directions of 200°–280° at hub height (90 m) in the period 2008–2017. This figure was created with Matplotlib (Hunter, J. D., Matplotlib: a 2D graphics environment. Computing in Science and Engineering 9, 2007) and Cartopy (Met office, Cartopy: a cartographic python library with a matplotlib interface. Exeter, Devon, https://scitools.org.uk/cartopy, 2015).

along transects crossing several wind farms (Fig. 8). The wind speed deficit, being higher towards the downwind wind farm edge, leads to an annual reduction of up to 25% in the CF of downwind wind turbines inside wind farms; outside these wind farms, the CF losses reach up to 20% depending on the size of the farm and distance away from it. For example, as shown in Fig. 8a, wind farm 2, which is 7 km from wind farm 1, suffers a mean wind speed deficit of 1–1.5 ms^{-1}. This reduces the CF of upwind turbines by 10–15% and that of downwind turbines by 15–20% in wind farm 2. Then, the wakes generated by wind farm 2 extend up to wind farm 3 (25 km away) with a deficit of 0.5–0.8 ms^{-1} and CF losses of 5–8%. The wake effect of wind farm 4 reaches up to 30 km. The wind speed between wind farms 1 and 2 recovers approximately 45% in 5 km. However, the recovery of the wind speed in the following wind farms is slow due to the accumulated effects. Similarly, as shown in Fig. 8b, the wake effect reaches approximately 33 km between wind farms 2 and 3 and approximately 28 km beyond wind farm 5. The wake generated by the wind farm 4 reduces the CF of wind farm 5 (17 km away) up to 12%. Due to the short distance between wind farms 3 and 4 (about 5 km), wind farm 4 receives about 1.5–2 ms^{-1} less wind speed which is equivalent to CF losses of 12–16%, during prevailing southwesterly winds. The transects of lines II and IV are shown in Fig. SI 11. The most productive wind turbines/farms are those located on the grid-cells at upwind edge/farms of the wind farms where the wind flow is uninterrupted[25].

The wake effect can substantially influence the economic potential of wind power generation within a cluster, in large farms, and in neighboring farms located at a distance within the wake. Annual mean wind speed deficits of 1–1.5 ms^{-1} and CF deficits of wind farms in the vicinity of large downwind clusters are frequent, within clusters, the reduction is even stronger and amounts up to a seasonal mean wind speed reduction of more than 3 ms^{-1} or a seasonal CF reduction of up to 25% (Fig. 8). Average wakes extend up to 40 km for the largest wind farms and clusters.

The highest wind speed deficits occur during the spring season which leads to the highest CF losses in these seasons. On a monthly timescale, the highest wind speed deficits are simulated in March and April, whereas the lowest deficits are simulated in November and December (see Fig. SI 12). The seasonal variations in wind speed deficits are related to the relatively stronger winds (see Fig. SI 12) and weaker stratification[42] during the autumn and winter seasons compared to the spring seasons. During spring, the atmospheric conditions are more stable than the other seasons which leads to longer wakes[18,42–44]. It implies that the most productive season is winter when the wind speed is higher and the stratification not stable.

Discussion and conclusions

The results show that the wind fields simulated by the regional climate model COSMO-CLM are in good agreement with the mast measurement stations FINO1 and FINO3 in the North Sea. It also indicates that the deployment of large wind farms near the mast measurement stations will affect their measurements. The COSMO-CLM model with the wind farm parametrization[15] simulated the wake generated by the wind farms reasonably well. Despite the differences in the upwind wind speed, the length and width of the wake were simulated quite well.

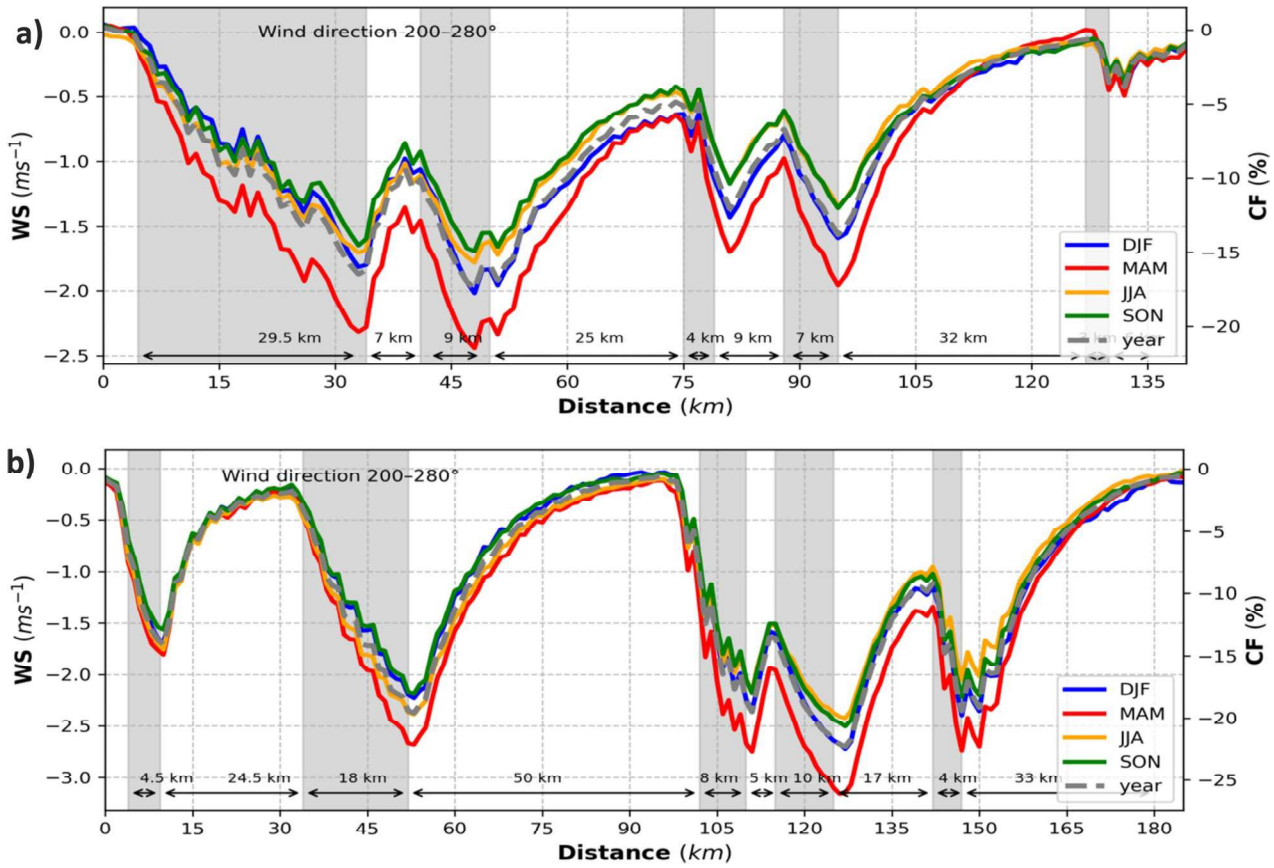

Figure 8. (**a**) Transects of the seasonal (colored, see legend) and yearly mean (dashed gray) wind speed deficits (left axis; CCLM_WF – CCLM) and capacity factor losses (right axis; CCLM_WF – CCLM) for the prevailing wind directions of 200°–280° in the period 2008–2017 at hub height (90 m) taken at transect I (German Bight, Fig. 5) latitude 54.2 latitude 54.2°N–55.6°N and longitude 5.45°E–8.0°E. Gray sectors indicate the wind farm positions. Arrows and attached numbers give the distances between the edges of the wind farms. (**b**) As of (**a**) but for transect III (Dogger Bank, Fig. 5) latitude 54.4°N–55.8°N and longitude 0.8°E–3.15°E.

Our results show that clusters of large wind farms, such as the farms planned for the near future in the UK's Dogger Bank and the German Bight, have the potential to substantially modify the atmospheric dynamics and lead to local mean wind speed reductions extending as far as more than 40 km downwind from the farm. Depending on the size of the wind farm, generally, the annual mean wind speed deficit can reach 2–2.5 ms^{-1} which is equivalent to the power loss of 1–2 MW[45]. These results are consistent with the previous studies[15,46,47]. These authors studied the consequences of wind farms in case studies and short-term simulations. Our results show that the previously identified effects accumulate and influence the mean wind pattern. We identified a trade-off in the clustering of offshore wind farms. Clustering supports reduced energy production costs due to reduced infrastructure investments, but these advantages can be offset by wakes effects and the consequent reduction of CF. Our results emphasize that wind energy in the North Sea can be considered a limited resource. With the current plans to install offshore wind energy farms in the North Sea locally resource exploitation limits are reached. Better planning and optimization of locations are required that consider the development of wind wakes under realistic multi-year atmospheric conditions.

It is important to note that for our idealized study we used an average size (90 m hub height and 126 m rotor diameter) of turbines for existing wind farms. The rapidly increasing size and power generation of wind turbines[48] can intensify the wake effects vertically and horizontally. Moreover, wind farm installations in the North Sea are further accelerating and the here identified limits of power generation will become more important.

Southwesterly winds are predominant in the North Sea[49] (Fig. 2 and Fig. SI 3), and wake effects and their implications for power generation are therefore of particular importance for efficient energy production and production costs. During prevailing southwesterly winds, the power production of a downwind wind farm on the northeastern side is generally undermined by the wind farms located upwind.

Under stably stratified atmospheric conditions, weak vertical momentum mixing strengthens the wake effect[11,15,18,20], and observational evidence shows that the wake can extend up to 50–70 km under such atmospheric conditions[30]. Such individual cases are also well reproduced in the model simulations. These findings suggest that CF losses can be greater than the mean values shown herein and last longer under stable atmospheric conditions. Additionally, this study shows the annual and seasonal mean values calculated using hourly values during the period 2008–2017 to illustrate the mean wake effect on the CF using multi-year weather conditions

under all atmospheric conditions. This shows that the wind speed and CF deficits are highest during spring (mainly March–April) and lowest during November–December. The proximity of large wind farms affects the production of downwind wind turbines and wind farms, reducing the CF by more than 20–25%.

Already now, offshore renewable energy production in the North Sea shows substantial impacts on the atmospheric conditions therein, and these effects will continue to increase in the future. The evidence indicates that OWFs can impact marine animals and can raise environmental and climate concerns[2,50,51]. Since wind is one of the main factors modulating ecosystem productivity and ecosystem structure, OWFs have the potential to develop into dominant ecosystem drivers and need to be considered for ecosystem management and fisheries assessment. Therefore, an optimization strategy based on both national and international considerations is required to minimize economic losses and to assess the limits and environmental impacts of industrial offshore energy production. Furthermore, atmospheric wakes can induce ocean responses by modifying the sea surface roughness, atmospheric stability, and heat fluxes, and hence have the potential to influence local climate that requires further investigation[32,52,53].

Methods

Numerical model setup. In this study, we employ the regional climate model COSMO-CLM[32] with a wind farm parameterization[15,33,34] to consider the wind farm impacts on local atmospheric dynamics and the spatial–temporal pattern of wind speed deficits for a near-future wind farm scenario in the North Sea (see Fig. SI 1). COSMO-CLM uses a horizontal atmospheric grid mesh size of 0.02° (~2 km; 396 × 436 grid cells) and 62 vertical levels. In our configuration, COSMO-CLM uses a time step of 12 s with a third-order Runge–Kutta numerical integration scheme. The physics options include a cloud microphysics scheme, a delta-two-stream scheme for shortwave and longwave radiation, and a one-dimensional prognostic TKE advection scheme for the vertical turbulent diffusion parameterization[54]. The roughness length over the sea is computed on the basis of the Charnock formula[54]. The initial and lateral boundary conditions for the wind, sea surface temperature and other meteorological variables are taken from a CoastDat3 simulation[29], which provides hourly data at a horizontal resolution of 0.11° (~11 km). The CoastDat3 atmospheric simulation was driven by European Centre for Medium-Range Weather Forecast (ECMWF) ERA-Interim reanalysis data in 6 hourly intervals at a horizontal resolution of 0.703°[55].

To include wind farm effects, a wind farm parameterization for mesoscale numerical weather prediction models is implemented into COSMO-CLM[56]. This parameterization represents wind turbines as a momentum sink for the mean flow that converts KE into electric energy and TKE. The parameterization uses the velocity in each grid to estimate the average effect of the wind turbines within that grid. In our configuration, we use five vertical levels within the rotor area. The wind turbine extracts KE from the mean flow of each layer intersecting the rotor area. The amount of extracted KE depends on the wind speed, thrust, power coefficients, air density, and the density of the wind turbines in the considered grid[45] (see Fig. SI 13). A fraction of the extracted KE is converted into electric power by the turbine, whereas the remaining part of KE is converted into TKE. Here, we use the thrust and power coefficients as a function of wind speed derived from the theoretical National Renewable Energy Laboratory (NREL) 5 MW reference wind turbine for offshore system development[45]. These coefficients are close to those of real wind turbines, as the NREL 5 MW turbine data were derived from the REPower 5 MW offshore wind turbine. The wind turbine is hallmarked by a cut-in wind speed of 3 ms^{-1}, a rated power speed of 12 ms^{-1}, and a cut-out speed of 25 ms^{-1}. In this study, we used the 90 m hub height and a 126 m rotor diameter with a rated power of 5.3 MW. The chosen turbine size falls within the range of existing wind farms by 2017 (Table SI 3). For a more detailed description of the wind farm parameterization and its implementation, we refer the readers to the previous studies[15,33,34].

Capacity factor (CF). Because of the high variability of wind, low, medium, and high wind speeds alternate frequently, and wind turbines cannot operate continuously at the rated power. Therefore, the CF is commonly used to calculate the average energy production of a wind turbine. In turn, the CF is used for the economic assessment of a project, optimum turbine site matching, and the ranking of potential sites[35]. Several generic models are available in the literature to represent the ascending segment of the power curve between the cut-in and rated speeds (Fig. SI 13) independent of the power coefficients, which are unique to every turbine and difficult to generalize. These generic models use the cut-in, rated, and cut-out speeds to estimate the ascending segment of the power curve without information on the turbine output. We use a polynomial generic model[35] to estimate the CF using a Weibull probability density function based on hourly wind speed values and three speeds, namely, the cut-in (3 ms^{-1}), rated (12 ms^{-1}), and cut-out (25 ms^{-1}), of the performance curve shown in Fig. SI 13.

Data availability

The model COSMO-CLM_WF and COSMO-CLM datasets supporting the results can be downloaded via CERA-DKRZ[57,58] and the COSMO-CLM namelists are available from the authors upon request. The COSMO-CLM simulations employ the community-wide publicly available (http://www.clm-community.eu) COSMO-CLM code. In situ airborne observational data were accessed via PANGAEA[30] and the FINO data were obtained via https://www.fino-offshore.de/en/ and http://fino.bsh.de.

Received: 31 January 2021; Accepted: 24 May 2021
Published online: 03 June 2021

References

1. Zheng, C. W., Li, C. Y., Pan, J., Liu, M. Y. & Xia, L. L. An overview of global ocean wind energy resource evaluations. *Renew. Sustain. Energy Rev.* **53**, 1240–1251 (2016).
2. Leung, D. Y. C. & Yang, Y. Wind energy development and its environmental impact: A review. *Renew. Sustain. Energy Rev.* **16**, 1031e9 (2012).
3. Junfeng, L., Pengfei, S. & Hu, G. China Wind Power Outlook 2010 (2010).
4. Tambke, J., Lange, M., Focken, U., Wolff, J. O. & Bye, J. A. T. Forecasting offshore wind speeds above the North Sea. *Wind Energy* **8**, 3–16 (2005).
5. Wang, J., Qin, S., Jin, S. & Wu, J. Estimation methods review and analysis of offshore extreme wind speeds and wind energy resources. *Renew. Sustain. Energy Rev.* **42**, 313–322 (2015).
6. WindEurope. Offshore wind in Europe: Key trends and statistics 2019 (2019).
7. The European Green Deal. Communication from the commission to the European parliament, the European council, the council, the European economic and social committee and the committee of the regions (2019).
8. WindEurope. Our Energy Our Future: How offshore wind will help Europe go carbon-neutral (2019).
9. 4c Offshore. https://www.4coffshore.com/windfarms/. (2019).
10. Hasager, C. B. *et al.* Wind farm wake: The 2016 Horns Rev photo case. *Energies* **10**, 317 (2017).
11. Lundquist, J. K., DuVivier, K. K., Kaffine, D. & Tomaszewski, J. M. Costs and consequences of wind turbine wake effects arising from uncoordinated wind energy development. *Nat. Energy* **4**, 26–34 (2019).
12. Siedersleben, S. K. *et al.* Evaluation of a wind farm parametrization for mesoscale atmospheric flow models with aircraft measurements. *Meteorol. Z.* **27**, 401–415 (2018).
13. Rhodes, M. E. & Lundquist, J. K. The effect of wind-turbine wakes on summertime US midwest atmospheric wind profiles as observed with ground-based Doppler Lidar. *Bound.-Layer Meteorol.* **149**, 85–103 (2013).
14. Djath, B., Schulz-Stellenfleth, J. & Cañadillas, B. Impact of atmospheric stability on X-band and C-band synthetic aperture radar imagery of offshore windpark wakes. *J. Renew. Sustain. Energy* **10**, 043301 (2018).
15. Fitch, A. C., Olson, J. B. & Lundquist, J. K. Parameterization of wind farms in climate models. *J. Clim.* **26**, 6439–6458 (2013).
16. Fitch, A. C. *et al.* Local and mesoscale impacts of wind farms as parameterized in a mesoscale NWP model. *Mon. Weather Rev.* **140**, 3017–3038 (2012).
17. Siedersleben, S. K. *et al.* Turbulent kinetic energy over large offshore wind farms observed and simulated by the mesoscale model WRF (3.8.1). *Geosci. Model Dev.* **13**, 249–268 (2020).
18. Platis, A. *et al.* First in situ evidence of wakes in the far field behind offshore wind farms. *Sci. Rep.* **8**, 1–10 (2018).
19. Irena. Renewable energy technologies: Cost analysis series. *Green Energy Technol.* **1** (2012).
20. Siedersleben, S. K. *et al.* Micrometeorological impacts of offshore wind farms as seen in observations and simulations. *Environ. Res. Lett.* **13**, 124012 (2018).
21. Smalikho, I. N. *et al.* Lidar investigation of atmosphere effect on a wind turbine wake. *J. Atmos. Ocean. Technol.* **30**, 2554–2570 (2013).
22. Churchfield, M. J., Lee, S., Michalakes, J. & Moriarty, P. J. A numerical study of the effects of atmospheric and wake turbulence on wind turbine dynamics. *J. Turbul.* **13**, 1–32 (2012).
23. Aitken, M. L., Kosović, B., Mirocha, J. D. & Lundquist, J. K. Large eddy simulation of wind turbine wake dynamics in the stable boundary layer using the Weather Research and Forecasting Model. *J. Renew. Sustain. Energy* **6**, 033137 (2014).
24. Calaf, M., Meneveau, C. & Meyers, J. Large eddy simulation study of fully developed wind-turbine array boundary layers. *Phys. Fluids* **22**, 015110 (2010).
25. Nygaard, N. G. Wakes in very large wind farms and the effect of neighbouring wind farms. *J. Phys. Conf. Ser.* **524**, 012162 (2014).
26. Nygaard, N. G. & Christian Newcombe, A. Wake behind an offshore wind farm observed with dual-Doppler radars. *J. Phys. Conf. Ser.* **1037**, 032020 (2018).
27. Nygaard, N. G. & Hansen, S. D. Wake effects between two neighbouring wind farms. *J. Phys. Conf. Ser.* **753**, 032020 (2016).
28. Badger, J. *et al*. Making the most of offshore wind: Re-evaluating the potential of offshore wind in the German North Sea. Study commissioned by Agora Energiewende and Agora Verkehrswende, 1–84 (2020).
29. Geyer, B., Weisse, R., Bisling, P. & Winterfeldt, J. Climatology of North Sea wind energy derived from a model hindcast for 1958–2012. *J. Wind Eng. Ind. Aerodyn.* **147**, 18–29 (2015).
30. Bärfuss, K. *et al.* In-situ airborne measurements of atmospheric and sea surface parameters related to offshore wind parks in the German Bight. PANGAEA https://doi.org/10.1594/PANGAEA.902845 (2019).
31. EWEA. The European offshore wind industry key 2015 trends and statistics. … *Documents/Publications/Reports/Statistics/* … 31 (2015). https://doi.org/10.1109/CCA.1997.627749.
32. Rockel, B., Will, A. & Hense, A. The regional climate model COSMO-CLM (CCLM). *Meteorol. Z.* **17**, 347–348 (2008).
33. Chatterjee, F., Allaerts, D., Blahak, U., Meyers, J. & van Lipzig, N. P. M. Evaluation of a wind-farm parametrization in a regional climate model using large eddy simulations. *Q. J. R. Meteorol. Soc.* **142**, 3152–3161 (2016).
34. Blahak, U., Goretzki, B. & Meis, J. A simple parameterization of drag forces induced by large wind farms for numerical weather prediction models. *European Wind Energy Conference and Exhibition 2010, EWEC 2010* **6**, 4577–4585 (2010).
35. Albadi, M. H. & El-Saadany, E. F. Optimum turbine-site matching. *Energy* **35**, 3593–3602 (2010).
36. Dean, N. Performance factors. *Nat. Energy* **5**, 5 (2020).
37. Leiding, T. *et al.* Standardisierung und vergleichende Analyse der meteorologischen FINO-Messdaten (FINO123) (2016).
38. Westerhellweg, A., Cañadillas, B., Kinder, F. & Neumann, T. Wake measurements at alpha ventus—Dependency on stability and turbulence intensity. *J. Phys. Conf. Ser.* **555**, 012106 (2014).
39. Perkins, S. E., Pitman, A. J., Holbrook, N. J. & McAneney, J. Evaluation of the AR4 climate models' simulated daily maximum temperature, minimum temperature, and precipitation over Australia using probability density functions. *J. Clim.* **20**, 4356–4376 (2007).
40. Lu, H. & Porté-Agel, F. Large-eddy simulation of a very large wind farm in a stable atmospheric boundary layer. *Phys. Fluids* **23**, 065101 (2011).
41. Chamorro, L. P. & Porté-Agel, F. A wind-tunnel investigation of wind-turbine wakes: Boundary-Layer turbulence effects. *Bound. Layer Meteorol.* **132**, 129–149 (2009).
42. Djath, B. & Schulz-Stellenfleth, J. Wind speed deficits downstream offshore wind parks—A new automised estimation technique based on satellite synthetic aperture radar data. *Meteorol. Z.* **28**, 499–515 (2019).
43. Emeis, S. A simple analytical wind park model considering atmospheric stability. *Wind Energy* **13**, 459–469 (2010).
44. Christiansen, M. B. & Hasager, C. B. Wake effects of large offshore wind farms identified from satellite SAR. *Remote Sens. Environ.* **98**, 251–268 (2005).
45. Jonkman, J., Butterfield, S., Musial, W. & Scott, G. Definition of a 5-MW reference wind turbine for offshore system development. *United States* https://doi.org/10.2172/947422 (2009).
46. Abkar, M. & Porté-Agel, F. Influence of atmospheric stability on wind-turbine wakes: A large-eddy simulation study. *Phys. Fluids* **27**, 035104 (2015).
47. Allaerts, D. Large-eddy simulation of wind farms in conventionally neutral and stable atmospheric boundary layers (2016).

48. IEA. Offshore Wind Outlook 2019. *World Energy Outlook* https://doi.org/10.1787/caf32f3b-en (2019).
49. Siegismund, F. & Schrum, C. Decadal changes in the wind forcing over the North Sea. *Clim. Res.* **18**, 39–45 (2001).
50. Saidur, R., Rahim, N. A., Islam, M. R. & Solangi, K. H. Environmental impact of wind energy. *Renew. Sustain. Energy Rev.* **15**, 2423–2430 (2011).
51. Tabassum, A., Premalatha, M., Abbasi, T. & Abbasi, S. A. Wind energy: Increasing deployment, rising environmental concerns. *Renew. Sustain. Energy Rev.* **31**, 270–288 (2014).
52. Boettcher, M., Hoffmann, P., Lenhart, H. J., Heinke Schlunzen, K. & Schoetter, R. Influence of large offshore wind farms on North German climate. *Meteorol. Z.* **24**, 465–480 (2015).
53. Platis, A. *et al.* Long-range modifications of the wind field by offshore wind parks—Results of the project WIPAFF. *Meteorol. Z.* https://doi.org/10.1127/metz/2020/1023 (2020).
54. Doms, G., Schättler, U. & Baldauf, M. *A Description of the Nonhydrostatic Regional COSMO Model. DWD COSMO V5.4.* http://www.cosmo-model.org (2011).
55. Dee, D. P. *et al.* The ERA-Interim reanalysis: Configuration and performance of the data assimilation system. *Q. J. R. Meteorol. Soc.* **137**, 553–597 (2011).
56. Akhtar, N. & Chatterjee, F. Wind farm parametrization in COSMO5.0_clm15 (2020) doi:https://doi.org/10.35089/WDCC/WindFarmPCOSMO5.0clm15.
57. Akhtar, N. coastDat-3_COSMO-CLM_HR_WF. *World Data Center for Climate* (*WDCC*) *at DKRZ.* http://cera-www.dkrz.de/WDCC/ui/Compact.jsp?acronym=DKRZ_LTA_302_ds00001 *(2020).*
58. Akhtar, N. coastDat-3_COSMO-CLM_HR. *World Data Center for Climate* (*WDCC*) *at DKRZ.* http://cera-www.dkrz.de/WDCC/ui/Compact.jsp?acronym=DKRZ_LTA_302_ds00002 *(2020).*

Acknowledgements

The study is initiated and funded by the Initiative and Networking Fund of the Helmholtz Association through the project "Advanced Earth System Modelling Capacity (ESM)". The authors would like to acknowledge the German Climate Computing Center (DKRZ) for providing computational resources, the Federal Ministry for Economic Affairs and Energy (BMWi) and the Federal Agency for Shipping and Sea for the FINO data, and Wind Park Far Field (WIPAFF) project for providing first in situ airborne atmospheric observational data of the offshore wind farms. The authors also acknowledge F. Chatterjee for helping with the implementation of the wind farm parameterization in COSMO-CLM. The authors thank Johannes Schulz-Stellenfleth for fruitful discussion and suggestions and Ulrike Kleeberg for contributing Fig. 1. We thank the CLM Community for their assistance and collaboration.

Author contributions

N.A. and B.R. implemented the wind farm parameterization in COSMO-CLM. N.A. designed the atmospheric simulations. B.G. provided the forcing data. N.A. and P.S. analyzed the data. B.G. wrote the FINO validation section. C.S. and B.R. initiated and supervised the work. N.A. wrote the original draft. All authors contributed to writing, reviewing, and editing the manuscript.

Funding

Open Access funding enabled and organized by Projekt DEAL.

Competing interests

The authors declare no competing interests.

Additional information

Supplementary Information The online version contains supplementary material available at https://doi.org/10.1038/s41598-021-91283-3.

Correspondence and requests for materials should be addressed to N.A.

Reprints and permissions information is available at www.nature.com/reprints.

Publisher's note Springer Nature remains neutral with regard to jurisdictional claims in published maps and institutional affiliations.

Wind Energ. Sci., 9, 697–719, 2024
https://doi.org/10.5194/wes-9-697-2024

eawe european academy of wind energy
Open Access WIND ENERGY SCIENCE

Mesoscale modelling of North Sea wind resources with COSMO-CLM: model evaluation and impact assessment of future wind farm characteristics on cluster-scale wake losses

Ruben Borgers[1], Marieke Dirksen[2], Ine L. Wijnant[3], Andrew Stepek[3], Ad Stoffelen[3], Naveed Akhtar[4], Jérôme Neirynck[1], Jonas Van de Walle[1], Johan Meyers[5], and Nicole P. M. van Lipzig[1]

[1]Department of Earth and Environmental Sciences, KU Leuven, Leuven, Belgium
[2]Department of Geoscience and Remote Sensing, Delft University of Technology, Delft, the Netherlands
[3]Royal Netherlands Meteorological Institute (KNMI), De Bilt, the Netherlands
[4]Institute of Coastal Systems – Analysis and Modeling, Helmholtz-Zentrum Hereon, Geesthacht, Germany
[5]Department of Mechanical Engineering, KU Leuven, Leuven, Belgium

Correspondence: Ruben Borgers [redacted]@kuleuven.be)

Received: 27 March 2023 – Discussion started: 6 April 2023
Revised: 14 December 2023 – Accepted: 30 January 2024 – Published: 20 March 2024

Abstract. As many coastal regions experience a rapid increase in offshore wind farm installations, inter-farm distances become smaller, with a tendency to install larger turbines at high capacity densities. It is, however, not clear how the wake losses in wind farm clusters depend on the characteristics and spacing of the individual wind farms. Here, we quantify this based on multiple COSMO-CLM simulations, each of which assumes a different, spatially invariant combination of the turbine type and capacity density in a projected, future wind farm layout in the North Sea. An evaluation of the modelled wind climate with mast and lidar data for the period 2008–2020 indicates that the frequency distributions of wind speed and wind direction at turbine hub height are skillfully modelled and the seasonal and inter-annual variations in wind speed are represented well. The wind farm simulations indicate that for a typical capacity density and for SW winds, inter-farm wakes can reduce the capacity factor at the inflow edge of wind farms from 59 % to between 54 % and 30 % depending on the proximity, size and number of the upwind farms. The efficiency losses due to intra- and inter-farm wakes become larger with increasing capacity density as the layout-integrated, annual capacity factor varies between 51.8 % and 38.2 % over the considered range of 3.5 to 10 MW km^{-2}. Also, the simulated efficiency of the wind farm layout is greatly impacted by switching from 5 MW turbines to next-generation, 15 MW turbines, as the annual energy production increases by over 27 % at the same capacity density. In conclusion, our results show that the wake losses in future wind farm clusters are highly sensitive to the inter-farm distances and the capacity densities of the individual wind farms and that the evolution of turbine technology plays a crucial role in offsetting these wake losses.

Published by Copernicus Publications on behalf of the European Academy of Wind Energy e.V.

1 Introduction

The global capacity of offshore wind technologies has increased more than 10-fold over the previous decade as part of the urgent transition to low-emission energy systems (IPCC, 2022). In 2021, the unprecedented commissioning of over 17 GW of offshore wind capacity pushed the cumulative, global capacity past 50 GW (Musial et al., 2022). In Europe, hosting more than half of that global offshore capacity, annual growth rates are expected to surpass 4 GW per year in 2023 (Komusanac et al., 2021). At the same time, the size and capacity of individual turbines are increasing, with a global average rating of 7.4 MW (8.5 MW in Europe) in 2021 compared to 3.3 MW in 2011 (Komusanac et al., 2021; Musial et al., 2022). As wind turbines offshore are organized in arrays, the total efficiency is impacted by turbine-to-turbine wake effects which strongly depend on the inter-turbine spacing and the size of the wind farm (e.g. Meyers and Meneveau, 2012; Stevens et al., 2016; Antonini and Caldeira, 2021). Currently, limited space and the urgent decarbonization of electricity systems lead to the installation and planning of very dense wind farms (capacity density $> 10\,\mathrm{MW\,km^{-2}}$) and exceptionally large wind farms (capacity > 1 GW) that are strongly impacted by these turbine interactions (Borrmann et al., 2018; Komusanac et al., 2020; EMODnet, 2022). On top of that, hotspots such as the North Sea are becoming more densely built (Matthijsen et al., 2018), which amplifies the risk of inter-farm interference through far-field wind farm wakes. These can extend several tens of kilometres (Platis et al., 2018; Schneemann et al., 2020) and can lead to considerable reductions in the wind resource (e.g. Lundquist et al., 2019; Akhtar et al., 2021; Munters et al., 2022). These developments raise questions on the magnitude of intra- and inter-farm wake losses in a future, densely clustered wind farm layout including large wind farms. Mesoscale models have been applied to illustrate the strongly reduced efficiency of very large wind farms (e.g. Volker et al., 2017; Antonini and Caldeira, 2021; Pryor et al., 2021) and how this depends on the turbine spacing (Volker et al., 2017), but also how wind farms can significantly alter the energy yield of neighbouring wind farms (e.g. Akhtar et al., 2021; Fischereit et al., 2022b). In this study, we aim to complement the existing work by quantifying how the long-term effect of wake losses in a hypothetical, future North Sea wind farm layout depends on the characteristics of the individual wind farms and on the inter-farm distances. Concretely, this is done based on a set of continuous simulations for one representative wind year, with each simulation including a different but spatially invariant combination of the turbine type and capacity density for the wind farms in a projected, future wind farm layout.

Although the WRF model is the most commonly used mesoscale model for wind energy applications (Fischereit et al., 2022a), it is important to involve several mesoscale models to determine whether signals are robust, especially when going to climatological timescales. In this study, we make use of the regional climate model COSMO-CLM, which has previously been applied for mesoscale wind farm simulations (Chatterjee et al., 2016; Akhtar et al., 2021, 2022) and also for the modelling of wind and wind resources of the past (e.g. Reyers et al., 2015; Geyer et al., 2015; Li et al., 2016) and future (e.g. Nolan et al., 2014; Santos et al., 2015; Reyers et al., 2016). The quality of mesoscale wind farm simulations relies heavily on the accurate simulation of the background wind climate, which is why these models are typically evaluated with in situ, lidar and/or satellite data (e.g. Hahmann et al., 2015; van Stratum et al., 2022; Dirksen et al., 2022). The COSMO-CLM model has been shown to skilfully reproduce winds from LES (Chatterjee et al., 2016) and measurements by offshore masts (Geyer et al., 2015; Akhtar et al., 2021). However, these evaluations have only considered a limited number of datasets and time periods. Therefore, an additional objective of this study is to extend the evaluation of COSMO-CLM based on a large set of multi-year, spatially distributed mast and wind lidar data and a satellite product covering most of the North Sea. With the focus on the wind resource, the evaluation includes metrics of power production derived from the modelled and measured wind speed data.

2 Data and methods

2.1 Model description

The development of the regional climate model COSMO-CLM (COSMO version 5.0, CLM version 15) is a joint effort between the COnsortium for Small-scale MOdelling (COSMO) and the Climate Limited-area Modelling community (CLM-Community) (Rockel et al., 2008). The Runge–Kutta dynamical core solves the non-hydrostatic, compressible hydro-thermodynamical equations on a rotated latitude–longitude grid (Doms and Baldauf, 2013). Several coordinate systems are available in the vertical dimension, of which we used the height-based, terrain-following coordinate with grid stretching. Additional physical processes were represented with available parametrizations: for subgrid-scale turbulence the standard choice was adopted, which is the one-dimensional diagnostic closure scheme (level 2.5) which is based on a prognostic TKE equation after Mellor and Yamada (1982) as described in Raschendorfer (2001). Surface fluxes were also parametrized and are coupled to the included multi-layer soil model, TERRA-ML. In addition, parametrizations for grid-scale clouds and precipitation, moist convection, and radiative processes were included (Doms et al., 2013). An extensive description of the model system is available in the documentation (e.g. Doms and Baldauf, 2013).

The simulation domain covered a large fraction of the North Sea with a horizontal grid spacing of 0.025° (∼ 2.8 km) (Fig. 1). In the vertical dimension, 61 levels were

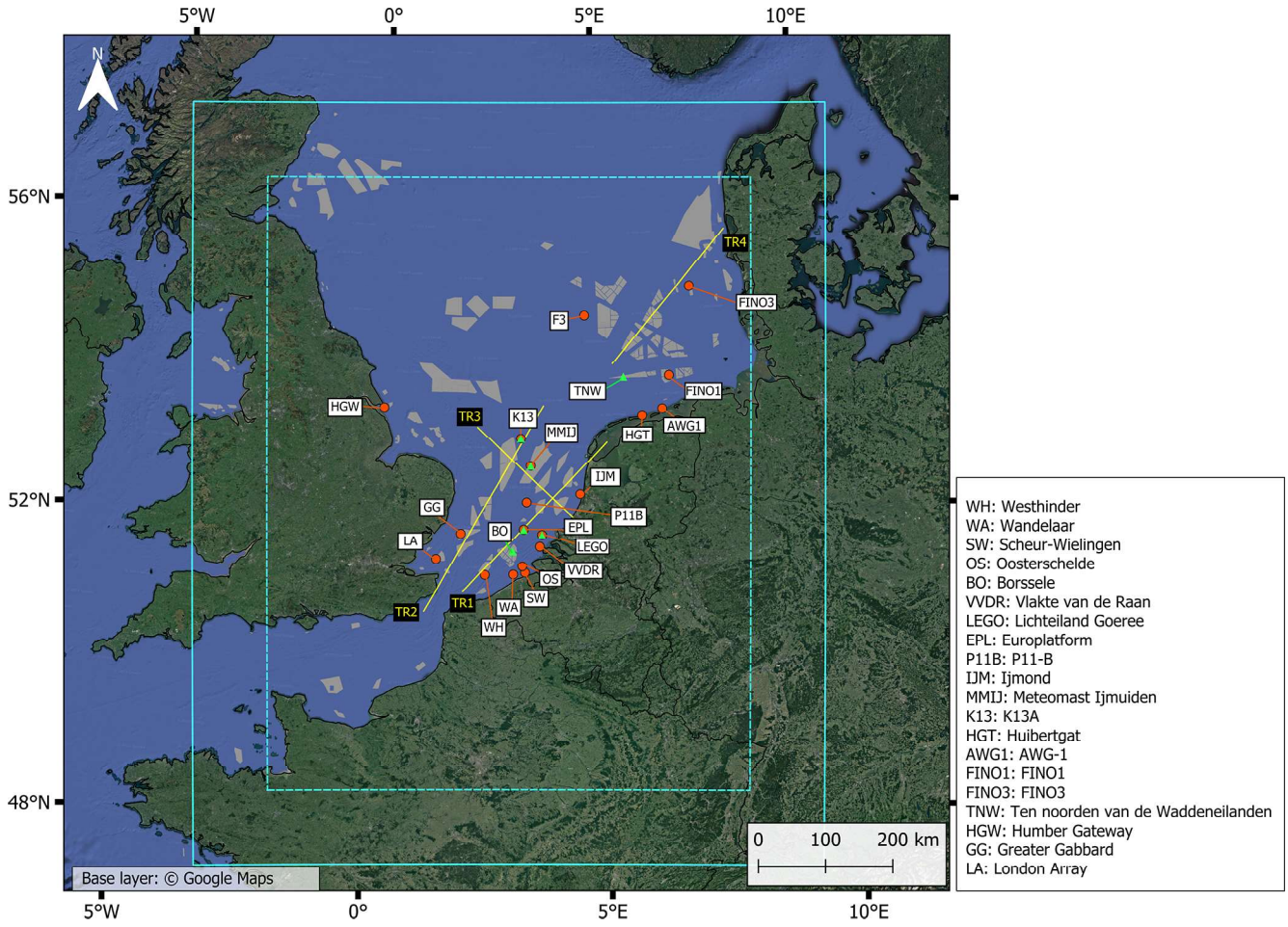

Figure 1. Map of the study area showing the simulation domain (cyan, solid line) and the evaluation domain (cyan, dashed line). The locations of the in situ measurement stations (orange dots) and lidar stations (green triangles) that are used for the model evaluation are also indicated, in addition to the hypothetical future wind farm layout (grey polygons) and the four analysis transects TR1–TR4 (yellow lines) used for the wind farm simulations. Created using QGIS3.4.

used up to an elevation of 22 km with a spacing of approximately 20 m near the surface and 30 m at turbine hub height. The relaxation zone at the lateral boundaries was set to a width of 40 km, whereas the spin-up zone was considered an additional 73 km wide, in agreement with the recommendations of Matte et al. (2017). The remaining inner part of the simulation domain was considered for the evaluation and analysis (Fig. 1). The ERA5 reanalysis (Hersbach et al., 2020) was used as forcing at the boundaries with updates every hour. No additional nesting stages were used, in line with results from Brisson et al. (2015). At the meso-γ scale, the model resolution partly allows the explicit development of deep convection so that only shallow convection was parametrized according to the scheme of Tiedtke (1989). Switching of the deep convection parametrization on this resolution has previously been shown not to degrade COSMO simulations (Vergara-Temprado et al., 2020). In COSMO5.0, the TKE advection term in the prognostic equation is only included for the experimental, LES-type turbulence schemes. With the focus on wind farm wake development in the second part of this study, we implemented the TKE advection term for the standard turbulence scheme in COSMO5.0 based on version 5.01.

Specific to this study, we also employed the Fitch wind farm parametrization (WFP; Fitch et al., 2012), which has been implemented in COSMO5-CLM15 (Chatterjee et al., 2016; Akhtar and Chatterjee, 2020). This additional module represents the wind farm forcing on the atmosphere as a sink of kinetic energy and a source of TKE. Although it has been suggested to reduce the TKE coefficient in the parametrization based on a comparison with large eddy simulations (LES) (Archer et al., 2020), the original value was retained in this study, as other studies did not find that this leads to better performance (Siedersleben et al., 2020; Larsén and Fischereit, 2021). Several other wind farm parametrizations exist (Fischereit et al., 2022a), and it has been shown

that the modelled wind speed deficits inside and behind a wind farm can vary substantially from the Fitch WFP (Ali et al., 2023). However, validation of the Fitch WFP with offshore masts, lidars and airborne measurements in the wake of a wind farm has shown very good performance for HARMONIE-AROME as wind speed biases are strongly reduced (van Stratum et al., 2022; Dirksen et al., 2022). This good performance has also been determined in WRF by comparing to offshore masts (Garcia-Santiago et al., 2022) and in COSMO-CLM by comparing to LES (Chatterjee et al., 2016) and airborne measurements (Akhtar et al., 2021). Wind speed reductions inside of a wind farm have also been shown to agree well with airborne measurements (Ali et al., 2023), mast measurements (Dirksen et al., 2022) and RANS simulations (Fischereit et al., 2022c). Moreover, comparisons with other WFP schemes show that Fitch generally outperforms these other schemes, both inside a wind farm and in the farm wake (Fischereit et al., 2022c; Ali et al., 2023). For a detailed overview of the performance validation of this parametrization, we refer to the review of Fischereit et al. (2022a).

2.2 Evaluation run

To evaluate the model performance, a simulation was performed for a period of 13 years (2008–2020). Data from in situ, lidar and satellite measurements over the North Sea are abundant in both space and time for this period. Additionally, the length of the simulation ensures that a large variation in wind conditions, as described in e.g. Geyer et al. (2015) and Ronda et al. (2017), is sampled. The wind farm parametrization was excluded in this simulation because a time-static wind farm layout cannot represent the rapidly growing wind farm layout over this time period and most observations were representative for wind-farm-free conditions. Hence, only the undisturbed wind climate was evaluated, and the observations were filtered accordingly, which will be discussed in more detail in Sect. 2.4.1. The instantaneous wind field around hub height was written to output at a 10 min frequency following the standard for wind energy assessments (Menezes et al., 2020).

2.3 Wind farm simulations

The projected future wind farm layout used in the wind farm simulations was constructed from the EMODnet wind farm dataset (EMODnet, 2022) and GIS data from the Royal Belgian Institute for Natural Sciences (Vigin, 2022) (Fig. 1). Next to the operational wind farms today, this layout incorporates the concessions that are in different stages of the construction process, zones for which consent has been authorized and also large development zones. Because the wind farm parametrization assumes that turbines within a single grid cell never have any wake interactions, no additional information is required on the layout of the turbines in each wind farm. The turbines were assumed constantly operational, unless the wind speed was below the cut-in wind speed or above the cut-out wind speed. Considering the computational cost of these experiments, the time span was limited to one representative year in terms of the North Sea wind field. This year was determined in a procedure based on the one outlined in Tammelin et al. (2013). We used 31 years of hourly, hub-height wind fields from the ERA5 reanalysis (1990–2020) to compute a metric R for the representativeness per year and per grid cell:

$$R_{i,j,y} = \frac{\mathrm{S1}_{i,j,y}}{\sigma_{\mathrm{S1}}} + \frac{\mathrm{S2}_{i,j,y}}{\sigma_{\mathrm{S2}}} + \frac{\mathrm{S3}_{i,j,y}}{\sigma_{\mathrm{S3}}}, \tag{1}$$

where the indices i, j and y refers to a specific grid cell and year. These R values were computed per year for each North Sea grid cell between 51 and 55.5° latitude. Higher values of R correspond to more representative years. The different scores (S1–S3) are based on the agreement between single-year and the long-term (31 year) histograms as computed by the Perkins skill score:

$$\mathrm{PSS}(H_1, H_2) = \sum_{b=1}^{n} \mathrm{MIN}\left(F^{\mathrm{b}}_{H_1}, F^{\mathrm{b}}_{H_2}\right), \tag{2}$$

where H_1 and H_2 represent the first and second histogram and F^{b} represents the normalized frequency for bin b. The PSS represents the fraction of overlap between the two histograms, so that a PSS of 1 (or 100 %) represents complete overlap. For one-dimensional histograms, this metric is connected to the Earth mover's distance (EMD) metric, which in contrast represents the area of mismatch between two histograms (Rabin et al., 2008). S1 is the PSS between a wind speed histogram for a single-year and the multi-year wind speed histogram, using a bin width of 0.5 m s^{-1}. S2 is the same as S1 but for wind direction, using a bin width of 30°. Finally, S3 represents the mean PSS between the single- and multi-year wind speed distributions over 12 wind direction sectors. The scores (S1–S3) are standardized by the standard deviation to give each term in the sum equal weight. Summation of R over all grid cells then yields a representativeness for a specific year. The different scores and the final score per year are summarized in Figs. S1 and S2 in the Supplement, respectively. Based on this procedure, the year 2016 was selected for the simulations, as the representativeness is high overall for this year (Fig. S1). In addition, the representativeness is especially high for wind direction (Fig. S2), which is particularly important for the study of inter-farm wake interactions.

Five simulations were performed, consisting of one simulation without wind farms (NOWF) and four simulations using a fixed wind farm layout with the same turbine type and capacity density for all wind farms (Table 1). Based on the number of turbines, the total capacity and the surface area of operational wind farms in the North Sea, a median turbine capacity of 4.85 MW and a representative capacity density of 8.1 MW km^{-2} were determined. The 5 MW refer-

Table 1. Summary of the turbine type and capacity density used in the different wind farm model simulations.

Identifier	Turbine type	Capacity density ($MW\,km^{-2}$)
NOWF	–	–
NREL8.1	NREL 5 MW	8.1
IEA3.5	IEA 15 MW	3.5
IEA8.1	IEA 15 MW	8.1
IEA10.0	IEA 15 MW	10

ence wind turbine of the National Renewable Energy Laboratory (NREL) (Jonkman et al., 2009)) with a hub height of 90 m and a rotor diameter of 126 m was therefore used in conjunction with the aforementioned capacity density in one of the wind farm simulations (NREL8.1). Three additional cases were simulated in which the NREL 5 MW was replaced by the 15 MW reference wind turbine of the International Energy Agency (IEA) (Gaertner et al., 2020) with a hub height of 150 m and a rotor diameter of 240 m, as 15 MW turbines are expected to reach the market in a few years and are now being selected for upcoming projects (Bento and Fontes, 2019; Shields et al., 2021). The power curves of these three turbines are available in Fig. S3. The three cases with 15 MW turbines were simulated with a different wind farm capacity density.

- *IEA3.5: low capacity density in which the inter-turbine distance is 10 rotor diameters*. This turbine spacing is larger than is found in most offshore wind farms today and corresponds to a lower cost per unit energy production as the impact of turbine wakes is reduced and is most relevant in regions where offshore space is relatively abundant, such as for the United Kingdom or Denmark (Borrmann et al., 2018).
- *IEA8.1: the same capacity density as for the NREL8.1 scenario*.
- *IEA10.0: high capacity density with a larger revenue per unit area but also increased wake-related losses*. This corresponds to a capacity density for planned projects in regions where the available space is limited, such as Belgium, the Netherlands and Germany (Borrmann et al., 2018).

Based on the different simulations, the impact of the turbine type and capacity density on the wake losses was assessed. In addition, the roles of wind farm size and inter-farm distance in these wake losses were investigated based on the large variation in these properties over the wind farm layout. The different simulations were compared along the transects indicated on Fig. 1, which correspond to dominant but also strongly disturbed wind directions, i.e. directions along which the wind farms are densely clustered. For this analysis, only winds in a sector of 30° around the transect orientation (SW to NE for TR1, TR2 and TR4 and NW to SE for TR3) were selected based on the centre grid cell on the transect. The data selection based on the wind direction reduced the dataset to approximately 14 % of the total for transects TR1, TR2 and TR4 and to 8.1 % for TR3. Additionally, this transect analysis was extended to three stability classes based on the bulk Richardson number (R_B), a metric for the dynamic stability, which will be discussed in more detail in Sect. 2.5.3.

2.4 Measurement data

2.4.1 In situ masts

Wind measurements of 19 in situ stations (Fig. 1) were obtained from the KNMI data platform, Meetnet Vlaamse Banken, the Marine Data Exchange, the FINO data platform and the TNO wind energy data platform (Table A1). Of these 19 stations, 6 were actual meteorological masts with measuring devices at multiple altitudes. The remaining stations correspond to coastal measurement poles and instrumentation mounted on oil, gas or light platforms and provide information at a single altitude. Average wind speed and wind direction are available at 10 min intervals. A timeline of the data availability is summarized for each station in Fig. S4. For most stations, corrections were applied to the measurements of the boom- or platform-mounted anemometers and wind vanes in order to account for flow distortions by the mast or other mounting infrastructure. These corrections were performed by the data providers for the stations FINO1 and FINO3 (Westerhellweg et al., 2012; Leiding et al., 2016), MMIJ (Werkhoven and Verhoef, 2012), WH and WA. For the remaining stations with multiple anemometers per height level, we avoided using measurements in the wake of the mast or other infrastructure by selecting the measurement with the highest 10 min average wind speed. A possible drawback of this approach is that the measured wind speed is overestimated in the case of lateral speed-up effects (Leiding et al., 2016). If wind direction was provided with respect to magnetic north, a magnetic-to-true north correction was applied according to the location and timing of the dataset. Finally, because no wind farm parametrization was included in the evaluation run, measurements potentially taken in the wake of wind farms were omitted from the dataset by filtering out either a specific time range or a directional sector. These dataset corrections are summarized in Table S1 in the Supplement. A station-to-farm distance threshold of 50 km was chosen to perform these corrections, as it is expected that the impact of wind farm wakes on the long-term wind speed statistics becomes relatively unimportant at this distance (Schneemann et al., 2020; Dirksen et al., 2022). The total uncertainty on the wind speed measurements is a combination of the uncertainties of calibration, mounting (including flow obstruction by the mast), data acquisition and the local site conditions. This total uncertainty can vary signifi-

cantly between the stations. For the class 0.9A anemometers at station MMIJ the total uncertainty was estimated at 1.5 % for the top anemometer and 1.9 % for the boom-mounted anemometers (Duncan et al., 2019). For the top anemometers of the other meteorological masts, which have a comparable class number as for MMIJ (Friis Pedersen et al., 2006), we applied the same value of 1.5 % as the uncertainty estimate. As the boom-mounted anemometers at the FINO stations were also mast-corrected prior to use, we adopted the same value of 1.9 %. The mounting uncertainty for boom anemometers at stations GG, LA and HGW is expected to be larger because we only performed a simple correction. Assuming an additional 2 % uncertainty on the mast correction, this leads to a total uncertainty of 3.7 %. For the remaining stations, we assumed a calibration uncertainty of 1.5% (Coquilla et al., 2007), an operational uncertainty of 0.8 % (Friis Pedersen et al., 2006) and an augmented 2 % uncertainty on the data acquisition due to limited information on acquisition and post-processing. For AWG1, P11B and WH a mounting uncertainty of 5 % was estimated due to presence of lateral flow obstructions. For the other stations, where the device is mounted on the top of a platform or platform-mounted mast, a mounting uncertainty of 2 % was assumed following Verkaik (2001).

2.4.2 Wind lidar

In addition to the cup anemometers, measurements from six wind lidars were used for the evaluation (Fig. 1). These lidars use light beam scanning technology to derive vertical profiles of wind speed and direction at regular height intervals and allow evaluation of the wind field above the typical 90 m top of meteorological masts. As for the in situ measurements, wind speed and direction are provided as 10 min averages. The data were obtained from the Dutch services TNO wind energy and Rijksdienst voor Ondernemend Nederland (RVO). The lidars were installed during the pre-construction stages of offshore wind farm development (Table A2). The LEGO, MMIJ, K13 and EPL lidars are installed on the same platforms as the cup anemometers (Table A1). The BO and TNW lidars are floating lidars and are mounted on a Fugro SEAWATCH buoy. Estimates of the uncertainty are from Wouters and Verhoef (2019a, b, c) for LEGO, EPL and K13; from Poveda and Wouters (2015) for MMIJ; and from the report by Dhirendra (2014) for the floating lidars BO and TNW.

2.4.3 ASCAT

The Advanced SCATterometer (ASCAT) sensor on the European MetOp satellites uses radar technology to determine the near-surface wind speed and direction over the sea (Gelsthorpe et al., 2000; Figa-Saldaña et al., 2002). Although the ASCAT product only provides information on the surface wind, it complements the in situ and lidar data as it covers most of the North Sea basin. For this study, we considered the L3-reprocessed ascending and descending passes of the MetOp-A satellite from the website of the Copernicus Marine Service (CMEMS). The satellite was operational for the complete 13 years of this simulation. Specifically, the variant on a 12.5 km grid with a horizontal grid spacing of 25 km was used, which has been validated against buoy measurements (Verhoef and Stoffelen, 2009). The long-term instrumental stability is estimated to be below 0.1 m s^{-1} for this product, whereas the climatological uncertainty is ± 0.1 m s^{-1}, with some anomalies of $+1$ m s^{-1} at the Dutch coast. The datasets for both passes together provide roughly one instantaneous measurement per day for most of the North Sea that we consider (4500 samples in total). Only close to the coasts is data coverage much lower (100–3000 samples), which is a well-known issue with remotely sensed winds related to contamination with land signal (Bourassa et al., 2019).

2.5 Evaluation approach

2.5.1 Model collocation with in situ and lidar

Over a 10 min period, the wind travels over a distance comparable to the edge length of a 0.025° grid cell. Because the model wind components represent smoothed grid box averages, the 10 min time averages of the observations were directly compared to instantaneous values of the grid cell in which the station is located. In the case of gaps in the time series of the in situ and lidar data, the corresponding time steps were also eliminated from the model grid point time series. The model wind speed data were interpolated to the measurement heights using the wind profile power law:

$$V_{\mathrm{s}} = V\left(h_{\mathrm{m}}\right) \cdot \left(\frac{h_{\mathrm{s}}}{h_m}\right)^{\alpha}, \tag{3}$$

where V_{s} is the wind speed at sensor height, $V(h_m)$ is the wind speed at the first model level below sensor height and α is the shear coefficient which is computed as

$$\alpha = \frac{\ln\left(V\left(h_{m+1}\right) / V\left(h_m\right)\right)}{\ln\left(h_{m+1} / h_m\right)}, \tag{4}$$

where $m+1$ denotes the first model level above sensor height. In contrast to the wind speed, the model wind direction at sensor height was computed after linear interpolation of the horizontal wind components of the model levels just above and below sensor height. The Zephir 300S lidar has a well-known 180° ambiguity that can occur in the wind direction time series as it relies on a sonic anemometer just above the lidar to determine the sign of the wind vector. In the case of low wind speeds and/or flow obstructions, it is possible that the incorrect sign is determined and the lidar's wind direction is 180° off (Knoop et al., 2021). We corrected this 180° error by adding or subtracting 180° if the wind direction in the measurements differs more than 90° from the modelled wind direction (~ 2 % occurrence) after Dirksen et al. (2022).

2.5.2 Model collocation with ASCAT and triple collocation

For the comparison with ASCAT, the model surface winds were regridded to the 12.5 km grid of the measurements with first-order conservative remapping. This ensures that all the source grid cells contained within a target grid cell have similar weight in the regridding, in agreement with the ASCAT winds being computed from the signal of this complete area. Afterwards, the measurement time series of each ASCAT grid cell was matched by a model time series for that same grid cell by linear interpolation in time.

Additionally, a comparison between the model, ASCAT and in situ data was conducted at stations WH, EPL and MMIJ. These stations were selected because the location is far enough from the coast to ensure sufficient data points in the ASCAT data and the measurement height is close to 10 m, which reduces any vertical extrapolation errors to 10 m in the in situ data. This extrapolation was done using the power law with a constant shear coefficient of 0.11. The in situ data were then also linearly interpolated to the ASCAT measurement times, and all datasets were limited to the timings where both ASCAT and in situ measurements are available. Finally, the grid cells in which the stations are located were selected from the model and ASCAT datasets for the comparison.

2.5.3 Stability classification

The comparison between COSMO-CLM and the measurements in terms of wind speed was further extended to different classes of atmospheric, dynamic stability because the stability strongly determines the wind conditions over the North Sea (Stull, 1988; Sathe et al., 2011) and also determines the atmospheric response to a wind farm forcing (Platis et al., 2021). This stability classification was done based on the bulk Richardson number (R_B), which is computed as

$$R_B = \frac{\frac{g}{\overline{\theta_v}} \frac{\Delta \theta_v}{\Delta z}}{\left(\frac{\Delta u}{\Delta z}\right)^2 + \left(\frac{\Delta v}{\Delta z}\right)^2}, \tag{5}$$

where g corresponds to the gravitational constant, θ_v is the virtual potential temperature, z is height, and u and v are the zonal and meridional wind speed components, respectively. The overbar over the virtual potential temperature denotes that it is averaged over the four model layers between 50 and 150 m height. Finally, the gradients in u, v and θ_v were determined by averaging the gradients between each of the subsequent layers between 50 and 150 m. Based on the (R_B), we can identify three distinct dynamic stability regimes (Grachev et al., 2013; Dirksen et al., 2022).

- *Unstable:* $R_B < 0$. This is the case when the temperature gradient is negative, which corresponds to an unstable thermal stratification.
- *Weakly stable:* $0 \leq R_B \leq 0.25$. This is the case when the temperature gradient is positive, but the temperature effect is weak compared to the vertical wind shear. In this case, the wind-shear-generated turbulence is relatively strong compared to the buoyant damping.
- *Stable:* $R_B > 0.25$. This is the case when the temperature gradient is positive and strong compared to the vertical shear. In this case, the wind-shear-generated turbulence is strongly damped, and this region of the ABL can be considered dynamically stable.

Gradients were calculated based on potential temperature instead of virtual potential temperature as an analysis of the driving data showed minimal variations of specific humidity over the considered height range. A comparison of the modelled temperature gradients with measured temperature gradients at station MMIJ between 90 and 21 m a.m.s.l. shows a good correspondence in the long-term temperature gradient probability distribution, indicating sufficient model skill for this subdivision into stability classes (Fig. S5). Because vertical profiles of pressure and temperature are generally not available over the range of the meteorological masts or wind lidar scanning ranges, the stability criterion can only be computed for the model. Based on a good temporal correlation between the temperature gradients of COSMO-CLM and measurement mast MMIJ (Pearson correlation coefficient = 0.85), the time steps matched to a stability class for the model grid cell nearest to each measurement location were also matched to that stability class for the measurement data.

2.5.4 Evaluation metrics

We compared the magnitudes of the mean wind speed difference and the observational uncertainty to identify any model bias: an exceedance of the observational uncertainty at a measurement station was used as the threshold for the presence of a model bias at that location. In addition, the PSS (Sect. 2.3) was employed as a metric to express the agreement in the shape of two histograms of either wind speed or wind direction.

Because the relationship between wind speed and wind turbine power production is non-linear, we also evaluated differences between COSMO-CLM and the observations in terms of the capacity factor, which is given by

$$\mathrm{CF} = 100 \frac{\sum_{i=1}^{n} P(V_i)}{n P(V_r)} \ [\%], \tag{6}$$

where V_i is the hub-height wind speed at some instance i in the time series; V_r is the rated wind speed; and P is the generated power, which is a turbine-specific function of the wind speed. So, the capacity factor is the ratio between the power production of a specific turbine based on a wind speed time

series and the theoretical, maximum power production over that same period, i.e. for a turbine continuously operating at full capacity. This is an idealized notion of the capacity factor as it concerns an isolated turbine which constantly operates according to the power curve. For these calculations, we considered the power curve of the NREL 5 MW reference wind turbine, with a hub height of 90 m, for the meteorological masts with the top anemometer below 100 m and the power curve of the DTU 10 MW reference wind turbine (Bak et al., 2013), with a hub height of 119 m, for FINO1, FINO3 and the wind lidars (Fig. S3). An uncertainty range on the capacity factor based on the observed wind speeds was determined based on the uncertainty on the wind speed measurements: the observed wind speed distribution was shifted linearly by the product of the uncertainty and the mean wind speed after which upper and lower bounds on the capacity factor were computed. As the capacity factor is a percentage, absolute differences are also a percentage, so to avoid confusion it is always explicitly stated whether absolute or relative differences in the capacity factor are considered.

3 Results and discussion

3.1 Model evaluation

This subsection covers the model performance evaluation. First, the general evaluation based on all validation sources and the complete height range (10 to 290 m) is described. This is followed by a more detailed performance analysis at turbine hub height (~ 100 m), and finally the evaluation is extended to the different atmospheric stability classes.

The difference in the long-term mean wind speed between the in situ and lidar stations varies with height (Fig. 2). Below 90 m, the difference is generally negative (model underestimates the mean) and exceeds the measurement uncertainty range, indicating a model bias to lower wind speeds. However, the magnitude of the bias generally drops with increasing altitude over the considered height range, albeit with some exceptions (MMIJ, TNW). At measurement heights at or above 90 m, the difference is generally smaller and falls within the uncertainty range of the measurements. The gradient with height persists and the difference is positive above 130 m at the locations of the wind lidars. Although differences over height are substantial, there is no robust indication of regional differences in the ability of COSMO-CLM to model the climatological mean wind speed. The same figure but with relative differences is included in the Supplement (Fig. S6).

The mean difference between COSMO-CLM and the ASCAT data is between -0.5 and $0.5\,\mathrm{m\,s^{-1}}$ for most grid cells (Fig. 3). For approximately 45 % of the grid cells the mean difference is within the ASCAT climatological uncertainty of $\pm 0.1\,\mathrm{m\,s^{-1}}$. These grid cells are generally located farther from the coast and correspond to the regions without in situ measurements, which is an indication of good model performance in this region. The model underestimation near the surface that was identified against the in situ data in the southern North Sea is much smaller than the differences compared to ASCAT in this region (cf. Figs. 2 and 3). A three-way comparison with three in situ stations shows that the mean differences against the in situ data exceed the in situ measurement uncertainty for both COSMO-CLM and ASCAT (Fig. 3). Whereas COSMO-CLM generally underestimates the mean near-surface wind speed, ASCAT overestimates it with a larger magnitude, which explains the differences in PSS values. The PSS values are similar when both COSMO-CLM and ASCAT are corrected for the systematic bias with respect to the in situ data, which indicates that both perform similarly in approximating the distribution shape of the in situ data.

The distributions of wind speed near 100 m height match well with the meteorological masts and lidar stations in most cases (Fig. 4), leading to a PSS generally above 95 %. The associated absolute differences in the idealized capacity factor are within the uncertainty based on the wind speed measurements for 4 out of 10 stations. For FINO1, K13, MMIJ and HGW the differences are outside the uncertainty range, but the deviations from the lower bound of the uncertainty range are less than 1 %, while the deviations are higher for the GG and LA masts. For K13 and HGW the capacity factor difference exceeds the capacity factor uncertainty, whereas the mean wind speed difference is within the wind speed uncertainty, which can be linked to the non-linear relationship between wind speed and power production.

Although the inter-annual variability of the annual mean hub-height wind speed is typically around $1\,\mathrm{m\,s^{-1}}$, the corresponding variability in the wind speed bias between the model and the measurements is typically around $0.1\,\mathrm{m\,s^{-1}}$ or 10 % of that value (Table 2). The corresponding overlap between the single-year histograms generally does not vary more than 2 % over the years. Hence, the agreement in distribution location and shape between COSMO-CLM and the measurements remains consistent over consecutive years, regardless of the inter-annual variability in the wind conditions.

The intra-annual cycle in the wind speed distribution is also well represented by the model (Fig. 5). The gradual seasonal variation from higher (winter) to lower (summer) median wind speeds is accurately reproduced in addition to the variation in distribution width (Q_{25}–Q_{75} range) and more extreme conditions (Q_5 and Q_{95}). Moreover, in extreme months the model also succeeds in modelling the wind speed distribution as can be deduced from Fig. 5b at station TNW for February 2020, albeit with a heavier right tail and consequently more winds above the cut-out wind speed.

Evaluation of the long-term wind direction histograms near turbine hub height (using a bin width of 20°) shows an overlap of 95 % or more in most cases (Table 3) with the magnitude of the bias generally below 4°. A reason for the stronger deviation at FINO3 and EPL has not been identified. Because the considered measurements vary sub-

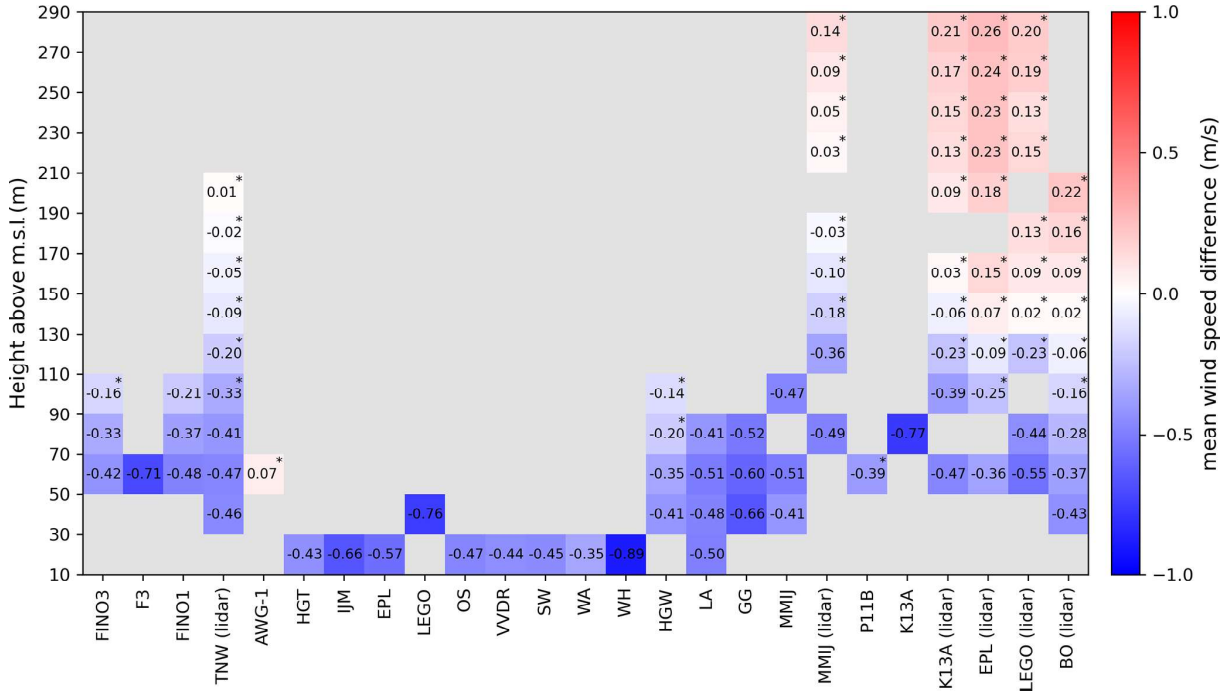

Figure 2. Wind speed bias ($m\,s^{-1}$) for the complete time span of each measurement dataset. This concerns measurements between 10 and 290 m a.m.s.l. The vertical range is subdivided into 20 m intervals for readability. The presence of an asterisk indicates that the bias is within the measurement uncertainty. Stations are clustered per region. The considered time periods for each measurement dataset can be found in Tables A1 and A2.

Table 2. Inter-annual range of the mean wind speed and of the agreement between the model and observations, as expressed by the minimum/maximum annual mean difference and the minimum/maximum annual PSS for the different years in the measurement period.

Station	Period (NR years)	Annual mean ($m\,s^{-1}$)		Mean difference ($m\,s^{-1}$)		PSS (%)	
		MAX	MIN	MAX	MIN	MAX	MIN
FINO3 (107 m)	2010–2013 (4)	11.2	9.5	−0.11	−0.22	98	97
MMIJ (92 m)	2012–2015 (4)	10.3	9.8	−0.44	−0.50	96	94
K13 lidar (115 m)	2018–2020 (3)	10.4	9.9	−0.2	−0.28	97	97
LEGO lidar (115 m)	2015–2020 (6)	11.1	9.2	−0.18	−0.28	97	95
LA (82 m)	2008–2010 (3)	9.5	8.6	−0.32	−0.47	95	93

stantially in measurement height, i.e. from 62 m a.m.s.l. up to 120 m a.m.s.l., this comparison indicates consistency of the good performance with height. The variations of the wind speed statistics with the wind direction are also captured by the model (Fig. S7). This accurate reproduction of the wind direction distributions and the direction-dependent wind speed distributions is encouraging for the application to wind farm modelling as wind farm shapes are tailored to the regional wind climate.

The general differences in mean wind speed profiles for the three stability classes agree well between the model and the measurements (Fig. 6): winds are strongest under weakly stable conditions and weakest under stable conditions, with the wind speeds under unstable conditions falling in between. The agreement between the profiles of the model and the measurements differs between the stability classes: under stable conditions the shear in the model is too strong between 40 and 200 m, leading to a negative model bias below 160 m for EPL and LEGO and below 180 m for K13 and TNW. Around 100 m, the respective underestimations are at least −0.3 and $-0.6\,m\,s^{-1}$. Such an underestimation under stable conditions is not uncommon for climate models (Wijnant et al., 2014; Sheridan et al., 2021). For weakly stable conditions, there is not a clear bias around 100 m, but the deviations below 90 m and above 150 m are outside of the observational uncertainty. The small vertical gradient under unstable conditions is represented well by the model with only small deviations that are well within the measurement

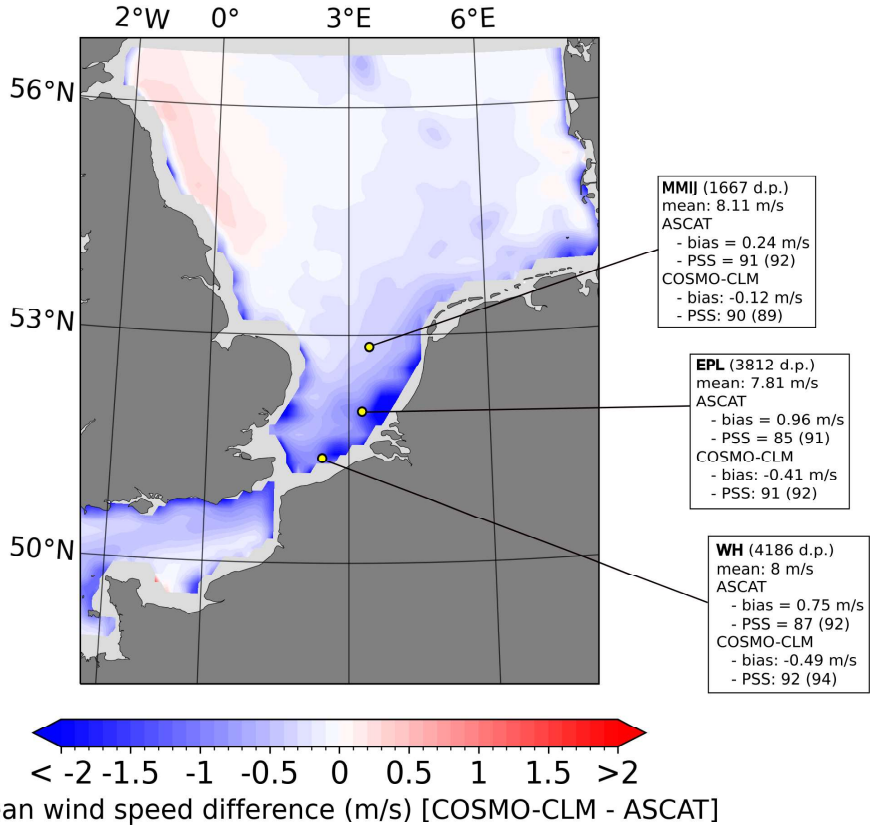

Figure 3. Difference in long-term mean wind speed between COSMO-CLM and ASCAT. Yellow dots indicate the measurement stations for triple collocation. The text boxes summarize the mean 10 m wind speed for three in situ stations and the agreement of ASCAT and COSMO-CLM in terms of the mean difference and the PSS. The PSS values between brackets are after elimination of the mean difference between the two histograms to remove the effect of distribution location.

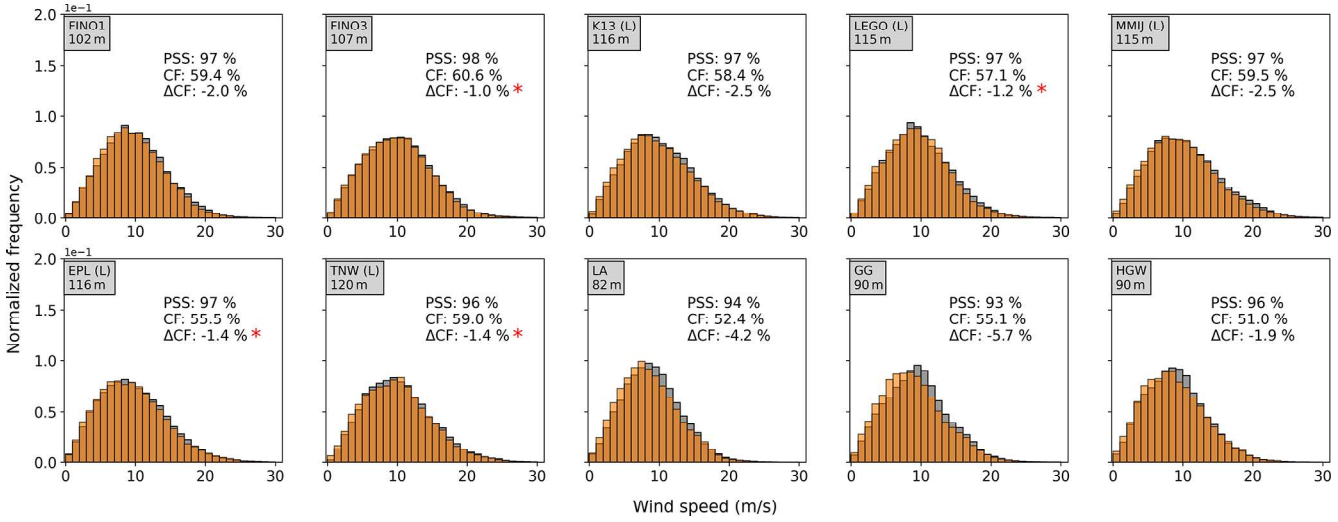

Figure 4. Histograms of the collocated wind speed datasets. Orange: overlap between the histograms; light orange: only COSMO-CLM; grey: only the measurements. In addition, the associated PSS, the capacity factor based on the measured wind speeds and the absolute difference in capacity factor between the model and the measurements are indicated. The presence of a red asterisk indicates that the capacity factor difference falls within the uncertainty on the capacity factor for the measurements.

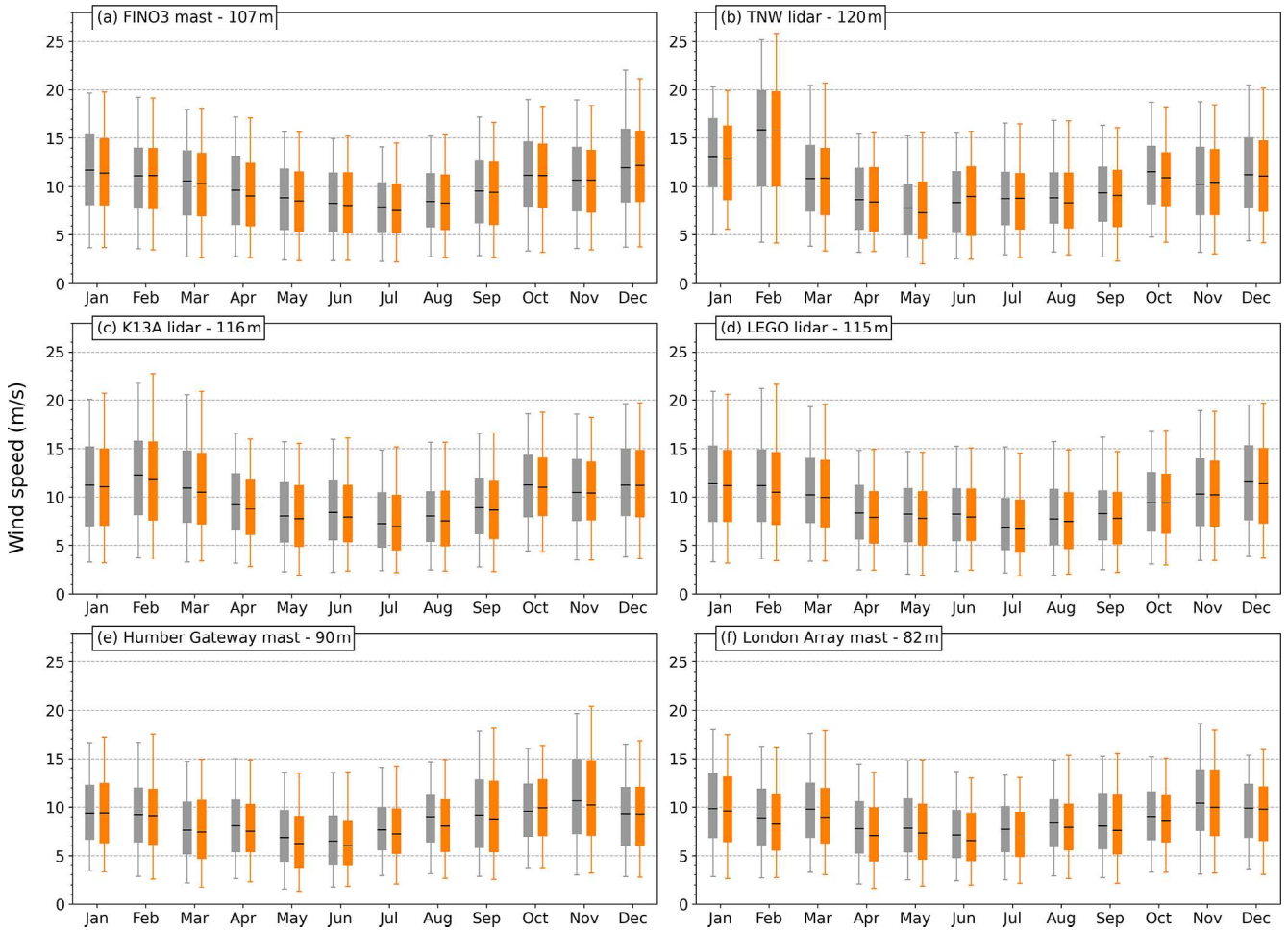

Figure 5. Boxplots representing the multi-year wind speed distribution per month for the observations (grey) and the model (orange). Shown for the three masts and three lidar stations at turbine hub height. The box corresponds to the Q_{25}–Q_{50}–Q_{75} wind speeds. The lower and upper whiskers are the Q_5 and the Q_{95} percentiles, respectively.

Table 3. Bias in the wind direction (model – observations) and the Perkins skill score between the histograms of wind direction (bin width = 20°).

Station	Bias (°)	PSS (%)
FINO3 (101 m)	−8.0	96
FINO1 (91 m)	1.9	95
TNW lidar (120 m)	−4.0	97
K13A lidar (116 m)	−2.2	97
MMIJ lidar (115 m)	1.0	96
EPL lidar (116 m)	8.7	93
LEGO lidar (115 m)	0.7	96
London Array (78 m)	−1.9	96
Humber Gateway (86 m)	2.3	96
Greater Gabbard (62 m)	−3.5	97

uncertainty over the complete height range. The hub-height wind speed distributions as reflected in the boxplot mainly differ in distribution location, with the strongest differences under stable conditions. Corresponding capacity factor values were calculated with lower and upper uncertainty bounds for the observations (Fig. S8). Under stable conditions, the deviations between the model and observations exceed the uncertainty range, so the absolute model underestimation of the capacity factor is at least 2.5 %. For unstable and weakly stable conditions, the deviations are within the uncertainty range.

3.2 Impact of wind farm characteristics on cluster-scale wake losses

This subsection covers the results of the wind farm simulations. First, the impact of the NREL8.1 base scenario on the wind climate and wind resource is described, also under different atmospheric stability conditions. Afterwards, the dif-

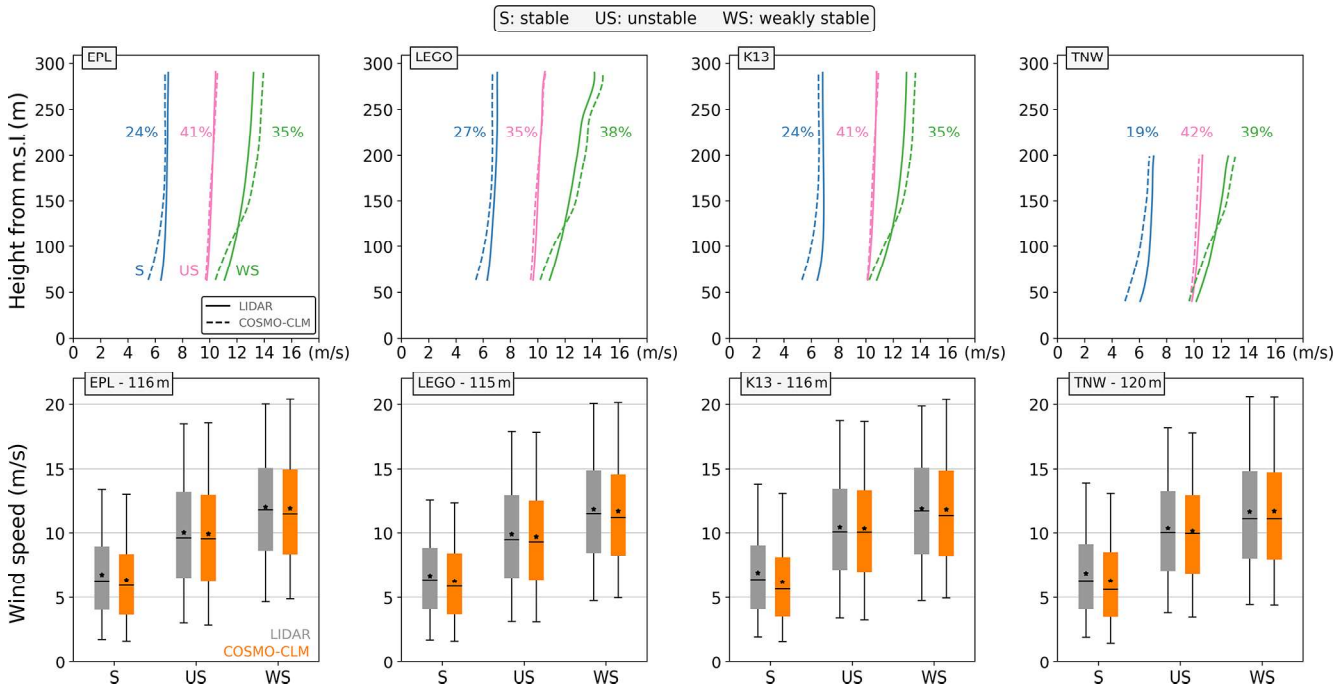

Figure 6. Model evaluation for different stability classes. Top row: vertical profiles of the mean wind speed per stability class for four lidar stations (full line) and the corresponding model output (dashed line). The stability classes are stable (blue), unstable (pink) and weakly stable (green). The indicated percentages are the relative frequency of the different stability classes at hub height. Bottom row: boxplots of the hub-height wind speeds per stability class for the same four lidar stations (grey) and the corresponding model output (orange). The box corresponds to the Q_{25}–Q_{50}–Q_{75} wind speeds. The asterisk indicates the mean, and the lower and upper whiskers are the Q_5 and the Q_{95} percentiles, respectively.

ferent wind farm scenarios are compared in terms of cluster-scale wake effects and efficiency of power production.

The modelled mean wind speed at 90 m for 2016 varies from 7.5 m s^{-1} at the coast up to 10 m s^{-1} in the open North Sea (Fig. 7). The associated capacity factor varies between 45 % and 60 %, and the simulated pattern agrees well with earlier, multi-decadal estimates over the North Sea (Geyer et al., 2015). Stability separation shows that the capacity factors are generally largest under weakly stable conditions and can reach 75 % in the open North Sea. For stable conditions, capacity factors are considerably lower but also prone to the bias discussed in Sect. 3.1. The bottom row of Fig. 7 visualizes the impact of the projected, future wind farm layout if they were all occupied with NREL 5 MW turbines at 8.1 MW km^{-2}. Without subdividing for stability, the absolute reductions of the full-year capacity factor in the immediate vicinity of farms located in dense clusters are around 15 %, with cumulative contributions from multiple wind farms. The magnitude of the long-term resource reductions is similar to what other studies have identified in terms of closely spaced wind farms (Akhtar et al., 2021; Fischereit et al., 2022b). Very close to the larger farms, larger values can be found even when the farms are isolated. The absolute and relative changes in the capacity factor vary over the stability classes. Absolute capacity factor reductions are typically the smallest for stable conditions, but these are the largest in relative terms as capacity factors are small themselves. In weakly stable conditions, absolute capacity factor reductions are much higher, as these exceed 13 % over large zones within and outside the wind farm clusters and 5 % more than 20 km from wind farm clusters and larger wind farms.

The impact of the atmospheric stability on the wind-farm-induced reduction in hub-height wind speed can be analysed in more detail along the four analysis transects (Fig. 8). For TR1, TR2 and TR4, the data are dominated by weakly stable conditions ($\sim$ 65 %) compared to unstable ($\sim$ 19 %) and stable ($\sim$ 16 %) conditions, whereas for TR3 unstable conditions are more prevalent ($\sim$ 59 %) compared to stable ($\sim$ 29 %) and weakly stable ($\sim$ 12 %) conditions. The relative reductions at the end of wind farms typically exceed 20 % for all stability classes, but reductions are generally smaller for unstable conditions than for stable and weakly stable conditions. However, the transects do not show a significantly slower wind farm wake recovery for stable conditions, as has been found based on observations (Cañadillas et al., 2020; Platis et al., 2021). The presented transect analysis also differs strongly from such studies in that it considers time averages of different wind speeds and covers a very large extent with the stability and wind direction criterion only evaluated at the centre of the transects. Added to that,

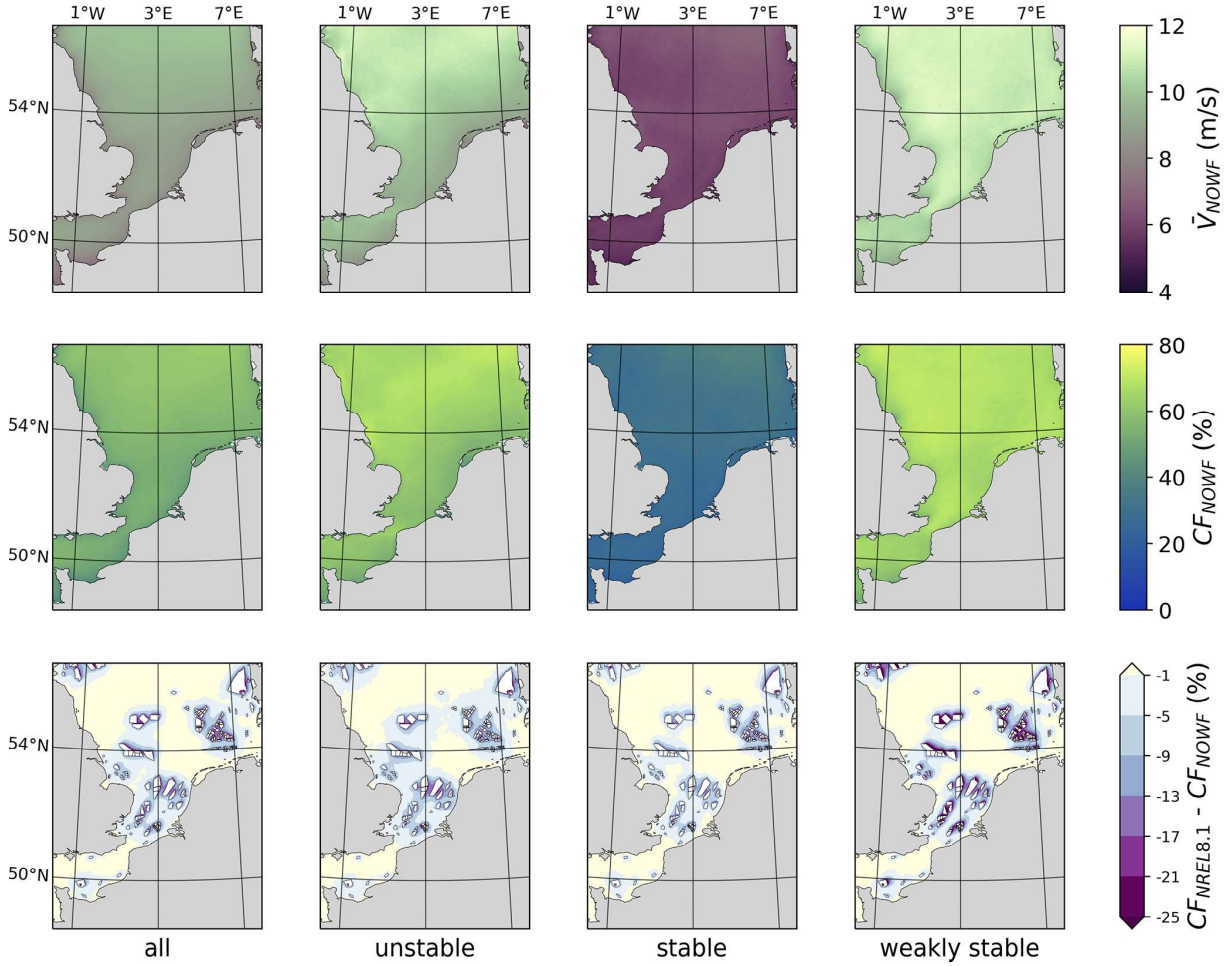

Figure 7. Maps of the modelled North Sea wind climatology at 90 m a.m.s.l., the corresponding wind resource in terms of the capacity factor, and the resource deficit under the NREL8.1 scenario for the complete year and for the three stability classes. Top: maps of the yearly mean wind speed ($m\,s^{-1}$) under the NOWF scenario. Middle: capacity factor under the NOWF scenario (%). Bottom: absolute capacity factor deficit for the NREL8.1 scenario (%). White polygons represent wind farm locations. Capacity factor computations are based on the power curve of the NREL 5 MW wind turbine.

modifications of dynamic stability by wind farms, which has previously been modelled with LES (Porté-Agel et al., 2014; Lu and Porté-Agel, 2015), could be strongly enhanced by the large, non-existent wind farms used in this study. The associated capacity factor profiles show that the relative impact on the wind resource is large for all stability classes (Fig. S9). The forcing by large wind farms and clusters can lead to a halving of the capacity factor for all stability classes in some transect sections. The relative impact on the capacity factor values is much larger than for the mean wind speed, due to the non-linearity of the turbine power curves (Fig. S3).

The wind farm capacity density used in the different wind farm simulations strongly determines the mean wind speed profile along these transects (Fig. 9). In each case, zones of densely clustered farms (< 20 km apart) are characterized by the strongest reductions and a limited farm wake recovery that is typically less than half of the maximum deficit at the previous wind farm. The scenario with IEA 15 MW turbines at 3.5 MW km^{-2} is characterized by the smallest reductions, which are typically within 1.5 $m\,s^{-1}$ at the upwind side of wind farms. For higher capacity densities, these upwind edge reductions are often more than twice as large and can exceed 3 $m\,s^{-1}$ under very dense clustering. Only for recovery distances of 30–60 km, the IEA8.1 and IEA10.0 scenarios converge to within 0.5 $m\,s^{-1}$ of the IEA3.5 scenario. Furthermore, the impact of wind farm size on the intensity of the reduction can be assessed by focusing on the first wind farm in each transect: the larger wind farms of TR1, TR3 and TR4 have an along-transect farm length between 24 and 31 km, while this is only 9 km for the one in TR2. The associated reductions at the downwind edge of the wind farms are approximately twice as large for TR1, TR3 and TR4 than for TR2.

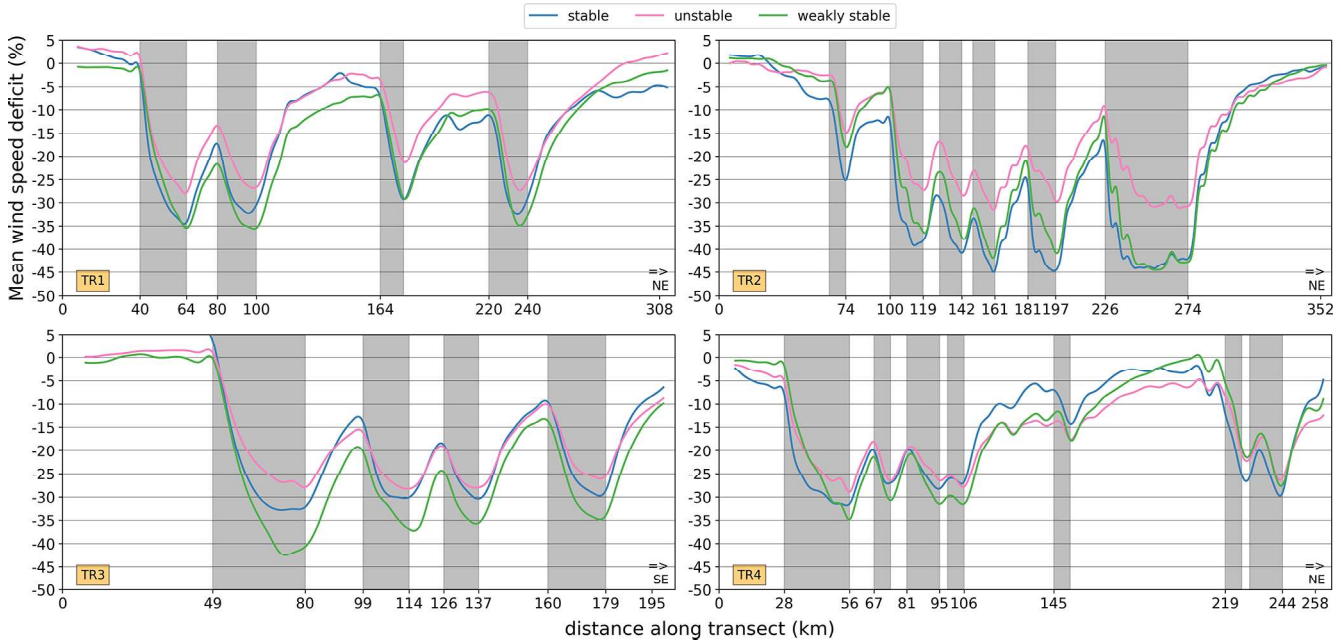

Figure 8. Relative deficit of the along-transect mean wind speed (%) at 90 m a.m.s.l. for the four transects indicated on Fig. 1. This concerns the NREL8.1 scenario, subdivided in the three dynamic stability classes: unstable (pink), weakly stable (green) and stable (blue) according to the R_B. Wind data are only considered when the wind direction deviates within ±15° from the transect orientation (W to E) at the middle grid cell of each transect. Grey shadings represent wind farm locations.

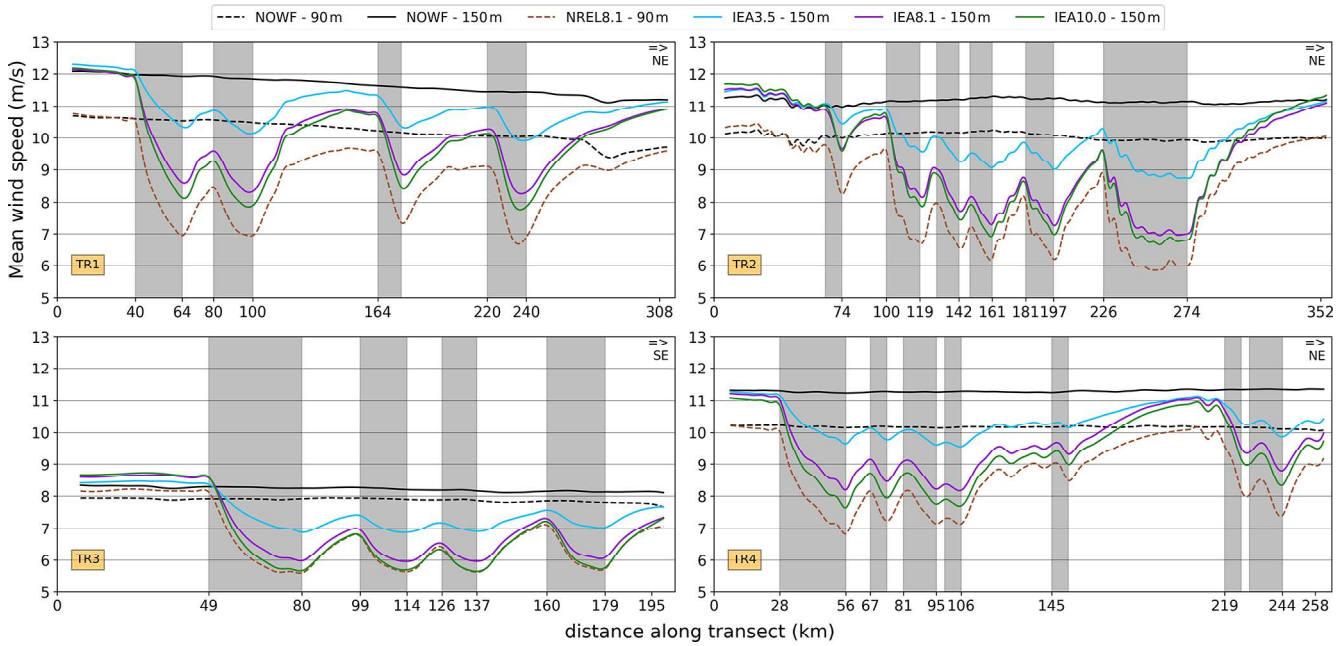

Figure 9. Transects of the mean wind speed at turbine hub height for the different wind farm scenarios. These transects correspond to the four lines in Fig. 1. Wind data are only considered when the wind direction deviates within ±15° from the transect orientation (W to E) at the middle grid cell of each transect. Grey shadings represent wind farm locations.

When converting the wind speed information of the NOWF scenario into capacity factors, the transect averages are ∼ 58 % for TR1, TR2 and TR4 and ∼ 38 % for TR3 when considering the hub height and power curve of the NREL 5 MW turbine. For the IEA 15 MW turbine, these increase to ∼ 66 % and ∼46%, respectively. Figure 10 shows that the associated, absolute reductions in these capacity factor follow the general patterns established for the mean wind speed. In each transect, the IEA3.5 scenario is characterized by the smallest deficits at the upwind edge of wind farms, typically around 10 % with larger values in dense clusters. For higher capacity densities, the upwind edge reductions reach 25 % to 30 % for closely spaced wind farms. The intensity of these upwind edge reductions is strongly dependent on the degree of upwind clustering and the sizes of the upwind farms. For the scenarios with higher capacity densities, the superposition of the high momentum sink on the already intense farm wake deficit eventually results in much lower wind farm efficiencies for these scenarios. For the SW–NE-oriented transects, the impact of the turbine type becomes apparent: for the 90 m turbines in the NREL8.1 scenario, the absolute deficits over the wind farms exceed those of the IEA8.1 scenario, which translates to a much stronger reduction in relative terms as the unaltered (NOWF) capacity factors for the 5 MW turbines are lower than for the 15 MW turbines.

The wind farm layout in the IEA8.1 scenario is significantly more efficient than for the NREL8.1 scenario, as reflected in the layout-integrated capacity factor and full load hours in the evaluation domain (Table 4). As a consequence, the integrated AEP is 27.4 % higher in the former. This difference is partly due to the rated wind speed being 0.8 m s^{-1} lower for the 15 MW turbines so that the rated section of the power curve is more wide (Fig. S2). Added to that, taller turbines can take advantage of the wind speed gradient with height, which leads to a larger fraction of wind speeds in the rated regime and a reduced fraction in the steep part of the power curve. To disentangle both effects, the 90 m wind speed data of the NREL8.1 scenario were fed to the 15 MW power curve, which resulted in an AEP of 539 TW h. This implies that approximately 40 % of the increase in AEP can be attributed to the lower rated wind speed and approximately 60 % to the wind speed gradient with height. Combining 15 MW turbines with a low capacity density of 3.5 MW km^{-2} only reduces the integrated capacity factor from 64.2 % in the NOWF scenario to 51.8 %, as a consequence of limited intra- and inter-farm wake impacts, in agreement with Meyers and Meneveau (2012) and Gupta and Baidya Roy (2021). From IEA3.5 to IEA8.1, the capacity density increases by 131 %, whereas the AEP only increases by 82 %. From IEA8.1 to IEA10.0, these increases are 23.4 % and 13.1 %, respectively. This efficiency degradation when moving to larger capacity densities can be recognized in a reduced capacity factor and a reduction in the full load hours (FLH): compared to IEA3.5, the IEA10.0 capacity factor is reduced from 51.8 % to 38.2 % and the FLH is reduced by approximately 1150 h. This follows from the increased wake losses that are further exacerbated by the densely clustered layout and the presence of several large wind farms that are typically characterized by very low power densities (Volker et al., 2017).

Table 4. Annual energy and power metrics integrated over all wind farms in the evaluation domain. CF: layout-integrated capacity factor. FLH: full load hours for the complete layout. AEP: annual energy production for the complete layout. The calculations are based on the wind speed data of the wind farm grid cells. The capacity factors for the NOWF simulation correspond to efficiency in absence of intra- and inter-farm wakes.

Experiment	Turbine	Total capacity (GW)	CF (%)	FLH (h)	AEP (TW h)
NOWF	NREL 5 MW	–	56.1	–	–
NOWF	IEA 15 MW	–	64.2	–	–
NREL8.1	NREL 5 MW	191	32.7	2549	488
IEA3.5	IEA 15 MW	83	51.8	4136	342
IEA8.1	IEA 15 MW	191	41.4	3252	622
IEA10.0	IEA 15 MW	236	38.2	2981	704

4 Conclusions

We have used the regional climate model COSMO-CLM to quantify the dependence of long-term, cluster-scale wake losses on the turbine type, capacity density, wind farm spacing and wind farm size for a hypothetical future wind farm layout. First, the model skill in simulating the wind climate was evaluated in a comparison with in situ, lidar and satellite data, which revealed the following.

- The differences between the measured and modelled, long-term mean wind speed at turbine hub height (∼ 100 m) are generally within the measurement uncertainty. This is also the case for differences at higher altitudes (up to 290 m), but closer to the surface COSMO-CLM underestimates the mean wind speed (∼ −0.5 m s^{-1}). Under stable stratification (∼ 25 %), the model underestimates the long-term mean wind speed at turbine height but not under weakly stable and unstable stratification (∼ 75 %).

- The agreement between the measured and modelled, long-term wind speed histograms is high, with a PSS above 95 % in most cases. The theoretical capacity factors derived from these histograms agree well overall, but small underestimations (∼ 1 %–5 %) are present at some locations.

- The agreement with the wind speed measurements is consistent over the different years of the simulation period as inter-annual variations in the mean wind speed

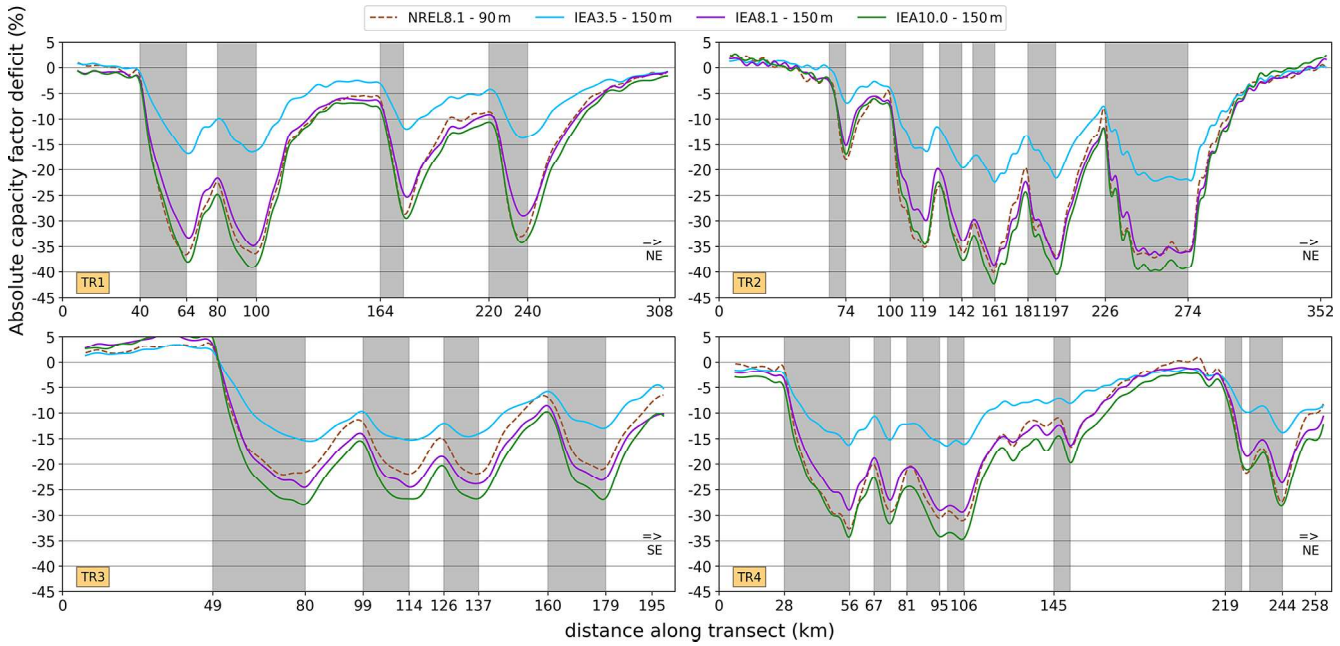

Figure 10. Transects of the absolute capacity factor deficit at hub height for the different wind farm scenarios. These transects correspond to the four lines in Fig. 1. Wind data are only considered when the wind direction deviates within ±15° from the transect orientation (W to E) at the middle grid cell of each transect. Grey shadings represent wind farm locations.

difference and the PSS are small. The seasonal variability in the shape and location of the wind speed distribution is also captured by COSMO-CLM.

– Multi-year histograms of wind direction also agree well, with again a PSS above 95 % in most cases. The variation of the wind speed histograms over 12 directional bins (30°) is also adequately captured in the model. This encourages the application of COSMO-CLM to wind farm modelling as wind farm shapes are adapted to the regional wind climate.

As deviations mainly occur under stable conditions, a stability-dependent bias correction could be considered for future applications in addition to continuous efforts to improve the model. Overall, this evaluation emphasizes the value of having a large set of wind measurements available in regions for offshore wind farm development, as it allows a benchmarking of mesoscale models over the region of interest.

The application of the model to a hypothetical, future wind farm layout indicates that the creation of dense wind farm clusters is accompanied by an alteration of the surrounding wind climate and significant farm-to-farm wake interactions. The impact of these interactions depends heavily on the turbine type, the capacity density, the inter-farm spacing and the size of the wind farms. In this study, the comparison of two turbine types (NREL 5 MW and IEA 15 MW) and three capacity densities (3.5, 8.1 and 10 MW km^{-2}) show the following.

– For a capacity density of 8.1 MW km^{-2}, the layout-integrated AEP is ∼ 27 % larger for a layout of 15 MW turbines than for 5 MW turbines. This difference is linked to the layout-integrated capacity factor being considerably larger when using taller, 15 MW turbines because of the increase in the wind resource with height (60 %) and a lower rated wind speed (40 %). The use of 15 MW turbines compensates for ∼ 37 % of the wake losses recorded in the NREL8.1 simulation.

– Under dominant wind directions with dense wind farm clustering, the wind resource is strongly reduced due to inter-farm wakes. Assuming 15 MW turbines, the absolute reductions in the capacity factor at the upwind edge of wind farms range from 3 % to 17 % for a capacity density of 3.5 MW km^{-2} depending on the degree of clustering and the size of the upwind farms. For a capacity density of 8.1 MW km^{-2} this ranges from 5 % to 30 % and for 10 MW km^{-2} from 5 % to 33 %.

– Assuming a projected, future wind farm layout with 15 MW turbines, increases in the capacity density of the wind farms lead to strong efficiency reductions. The layout-integrated capacity factor reduces from 51.8 % for a 3.5 MW km^{-2} capacity density to 38.2 % for a 10 MW km^{-2} capacity density, due to the intensification of intra- and inter-farm wake losses.

– Wind farm wake effects play an important role for all considered atmospheric stability classes, even if the im-

pact is a bit smaller for unstable conditions. Under strongly waked wind directions, the low capacity factors (20 %–30 %) under stable conditions ($R_B > 0.25$) can be further reduced to well below 10 %, thereby nearly completely halting the production of some of the simulated wind farms. Although these results are possibly impacted by the negative model bias that was found for stable stratification, it is expected that this large impact under stable conditions still holds.

Whereas comparisons between wind farm parametrizations have shown large variations in terms of modelled wind speed deficits inside and behind wind farms (Ali et al., 2023), validation efforts in several mesoscale models have indicated a very good performance of the Fitch WFP (Fischereit et al., 2022c; van Stratum et al., 2022; Ali et al., 2023). Nonetheless, the use of other WFP schemes might significantly alter the magnitudes presented here, more so due to the large clusters and large wind farms included in the considered layout, which can even lead to wake losses for background wind speeds well above rated. Hence, further benchmarking studies of WFPs for a range of atmospheric conditions and validation data could help in further reducing this WFP-related uncertainty. An additional complication here is that this study includes wind farms of non-existent sizes for which validations simply do not exist.

Even if the mesoscale wind farm parametrization approach has limitations, these modelling studies provide valuable information for the efficient deployment and operation of offshore wind infrastructure, more so because mesoscale models can consider the climatic variability of wake effects, for large regions. This study demonstrates the potential of this modelling approach to explore a large variety of wind farm characteristics and layouts in a climatic context, which can aid in a more efficient expansion of the offshore infrastructure.

Appendix A

Table A1. Description of the in situ measurement stations. S: wind speed (m^{-1}); D: wind from direction (°). The superscripts a, b and c link measurement heights to measurement devices in the next column. 1×, 2× and 3× refers to one, two, or three anemometers and/or wind vanes at one measurement height. Source acronyms: KDP, Royal Netherlands Meteorological Institute (KNMI) data platform; MNVB, Meetnet Vlaamse Banken; MDE, the Marine Data Exchange; FINO, Forschungsplattformen in Nord- und Ostsee; TNO, Nederlandse Organisatie voor Toegepast-natuurwetenschappelijk Onderzoek.

Name (abbreviation)	Location	Heights (m a.m.s.l.)	Measured variables	Period	Uncertainty (%)	Source
Westhinder (WH)	platform	26	$2 \times S, D$	2008–2020	5.6	MNVB
Wandelaar (WA)	measuring pole	26	$2 \times S, 1 \times D$	2013–2020	3.3	MNVB
Scheur-Wielingen (SW)	measuring pole	25	$1 \times S, D$	2010–2020	3.3	MNVB
Oosterschelde (OS)	measuring pole	17		2008–Jun 2019	3.3	KDP
Vlakte van de Raan (VVDR)	measuring pole	17		Sep 2009–Jun 2019	3.3	KDP
Lichteiland Goeree (LEGO)	platform	38	$2 \times S, D$	2008–2020	3.3	KDP
Europlatform (EPL)	platform	29	$2 \times S, D$	2008–2020	3.3	KDP
Ijmond (IJM)	measuring pole	17		2008–Jun 2019	3.3	KDP
P11-B (P11B)	mast on platform	51	$2 \times S, D$	2010–2020	5.6	KDP
Meteomast IJmuiden (MMIJ)	meteorological mast	27, 58[a], 92[b]	$a: 3 \times S, D, b: 2 \times S$	Nov 2011–Mar 2016	a : 1.9; b : 1.5	TNO
K13A (K13)	mast on platform	74	$2 \times S, D$	2008–2019	3.3	KDP
F3N (F3)	mast on platform	60	$2x \times S, D$	2010–Dec 2019	3.3	KDP
Huibertgat (HGT)	measuring pole	18		2008–Jun 2019	3.3	KDP
AWG-1 (AWG1)	mast on platform	60	$2 \times S, D$	Sep 2009–2020	5.6	KDP
FINO1 (FINO1)	meteorological mast	51, 71, 91[a], 102[b]	$a: 1 \times S, D; b: 1 \times S$	2008–Jul 2009	a : 1.9; b : 1.5	FINO
FINO3 (FINO3)	meteorological mast	50, 70, 90, 100[a], 107[b]	$a: 3 \times S, D; b: 1 \times S$	2009–Oct 2014	a : 1.9; b : 1.5	FINO
Humber Gateway (HGW)	meteorological mast	34, 52, 70, 88[a], 68[b], 90[c]	$a: 2 \times S; b: 1 \times D; c: 1 \times S$	Oct 2009–Jul 2011	a : 3.7; c : 1.5	MDE
Greater Gabbard (GG)	meteorological mast	42, 52, 72, 82[a], 62[b], 88[c]	$a: 2 \times S; b: 2 \times D; c: 1 \times S$	2008–2010	a : 3.7; c : 1.5	MDE
London Array (LA)	meteorological mast	20, 32, 57[a], 29, 78[b], 82[c]	$a: 2 \times S; b: 1 \times D; c: 1 \times S$	2008–2010	a : 3.7; c : 1.5	MDE

Table A2. Description of the lidar measurement stations. Source acronyms: RVO, Rijksdienst voor Ondernemend Nederland; TNO, Nederlandse Organisatie voor Toegepast-natuurwetenschappelijk Onderzoek.

Name (abbreviation)	Type	Location	Heights (m a.m.s.l.)	Period	Uncertainty (%)	Source
Borssele 1 (BO)	Zephir 300S	buoy	40:20:200	Jun 2015–Feb 2017	3.3–3.4	RVO
Lichteiland Goeree (LEGO)	Leosphere Windcube	platform	90:25:290 and 63	Nov 2014–2020	2.6–3.3	TNO
Europlatform (EPL)	Zephir 300S	platform	91:25:291 and 63	May 2016–2020	2.9–3.5	TNO
Meteomast IJmuiden (MMIJ)	Zephir 300S	platform	90:25:290	Nov 2011–Mar 2016	2.5–3.1	TNO
K13A (K13)	Zephir 300S	platform	91:25:291 and 63	2018–2020	2.7–3.2	TNO
TNVD Waddeneilanden A (TNW)	Zephir 300S	buoy	40:20:200	Sep 2019–2020	3.3–3.4	RVO

Code and data availability. The code and data used to generate Figs. 3–10 can be retrieved as one dataset at https://doi.org/10.5281/zenodo.8348700 (Borgers, 2023). The ERA5 reanalysis data used to identify representative wind years were downloaded via the Copernicus Climate Change Service (C3S) Climate Data Store (CDS) and can be found at https://doi.org/10.24381/cds.adbb2d47 (Hersbach et al., 2022). The ASCAT data were retrieved from the Copernicus Marine Service via https://doi.org/10.48670/moi-00183 (Copernicus Marine Service, 2022). The in situ measurements of the KNMI can be retrieved from their data platform, at https://dataplatform.knmi.nl/group/wind (Koninklijk Nederlands Meteorologisch Instituut, 2022). For the in situ data at the Belgian coast, data are accessible via the website of the Belgian coastal measurement network, at https://meetnetvlaamsebanken.be/ (Meetnet Vlaamse Banken, 2022). Mast data at the coast of the United Kingdom are available via the website of the Marine Data Exchange, at https://www.marinedataexchange.co.uk/ (The Crown Estate, 2022). For the German Bight, the data are available at the website of the FINO data platform, http://fino.bsh.de/ (Das Bundesamt für Seeschifffahrt und Hydrographie, 2022). Data from the IJmuiden meteorological mast and from the platform-mounted wind lidars can be found at the TNO data cloud website https://nimbus.windopzee.net/ (Nederlandse Organisatie voor toegepast-natuurwetenschappelijk onderzoek, 2022). Finally, the data from the buoy-mounted lidars can be found

at https://offshorewind.rvo.nl/ (Rijksdienst voor Ondernemend Nederland, 2022).

Supplement. The supplement related to this article is available online at: https://doi.org/10.5194/wes-9-697-2024-supplement.

Author contributions. RB contributed to the conceptualization, data curation, formal analysis, investigation, methodology, project administration, software, validation, visualization and writing (original draft, review and editing). MD contributed to the data curation, resources, methodology and writing (review and editing). IW, ASte and ASto contributed to the resources, methodology and writing (review and editing). NA contributed to the methodology, software and writing (review and editing). JN and JVdW contributed to the methodology and writing (review and editing). JM contributed to the conceptualization, funding acquisition, methodology, project administration, supervision and writing (review and editing). NPMvL contributed to the conceptualization, funding acquisition, investigation, methodology, project administration, resources, supervision, visualization and writing (original draft, review and editing).

Competing interests. At least one of the (co-)authors is a member of the editorial board of *Wind Energy Science*. The peer-review process was guided by an independent editor, and the authors also have no other competing interests to declare.

Disclaimer. Publisher's note: Copernicus Publications remains neutral with regard to jurisdictional claims made in the text, published maps, institutional affiliations, or any other geographical representation in this paper. While Copernicus Publications makes every effort to include appropriate place names, the final responsibility lies with the authors.

Acknowledgements. The computational resources and services in this work were provided by the VSC (Flemish Supercomputer Center), funded by the Research Foundation Flanders (FWO) and the Flemish government department EWI.

The authors further acknowledge the COSMO-CLM community for support in the modelling efforts in this study. EUMETSAT OSI-SAF, in which Ad Stoffelen is involved, is also acknowledged. Naveed Akhtar also acknowledges the support from the German Federal Ministry of Education and Research (BMBF) under project CoastalFutures (03F0911A), a project of the DAM Research Mission sustainMare – Protection and Sustainable Use of Marine Areas.

The authors further thank the Royal Netherlands Meteorological Institute (KNMI), the Meetnet Vlaamse Banken, the German Federal Maritime and Hydrographic Agency (BSH), and the Marine Data Exchange (MDE) for the in situ wind measurements, metadata and additional data handling support. The Energieonderzoek Centrum Nederland (ECN) and the Nederlandse Organisatie voor toegepast-natuurwetenschappelijk onderzoek (TNO) are also thanked for the mast and lidar measurements at IJmuiden and lidar measurements at Lichteiland Goeree, Europlatform, and K13A, and Rijksdienst voor Ondernemend Nederland (RVO) is thanked for the lidar data of Borssele and Ten Noorden van de Waddeneilanden. Finally, Copernicus and the Copernicus Marine Service are acknowledged for the ERA5 reanalysis and MetOp-A ASCAT measurements.

Financial support. This research has been supported by the project FREEWIND, funded by the Energy Transition Fund of the Belgian Federal Public Service for Economy, SMEs, and Energy (FOD Economie, K.M.O., Middenstand en Energie).

Review statement. This paper was edited by Julie Lundquist and reviewed by Andrea Hahmann, David Schultz, and Pablo Ouro.

References

Akhtar, N. and Chatterjee, F.: Wind farm parametrization in COSMO5.0_clm15, World Data Center for Climate (WDCC) at DKRZ, https://doi.org/10.35089/WDCC/WindFarmPCOSMO5.0clm15, 2020.

Akhtar, N., Geyer, B., Rockel, B., Sommer, P. S., and Schrum, C.: Accelerating deployment of offshore wind energy alter wind climate and reduce future power generation potentials, Sci. Rep., 11, 11826, https://doi.org/10.1038/s41598-021-91283-3, 2021.

Akhtar, N., Geyer, B., and Schrum, C.: Impacts of accelerating deployment of offshore windfarms on near-surface climate, Sci. Rep., 12, 18307, https://doi.org/10.1038/s41598-022-22868-9, 2022.

Ali, K., Schultz, D. M., Revell, A., Stallard, T., and Ouro, P.: Assessment of Five Wind-Farm Parameterizations in the Weather Research and Forecasting Model: A Case Study of Wind Farms in the North Sea, Mon. Weather Rev., 151, 2333–2359, https://doi.org/10.1175/MWR-D-23-0006.1, 2023.

Antonini, E. G. and Caldeira, K.: Spatial constraints in large-scale expansion of wind power plants, P. Natl. Acad. Sci. USA, 118, e2103875118, https://doi.org/10.1073/pnas.2103875118, 2021.

Archer, C. L., Wu, S., Ma, Y., and Jiménez, P. A.: Two corrections for turbulent kinetic energy generated by wind farms in the WRF model, Mon. Weather Rev., 148, 4823–4835, https://doi.org/10.1175/MWR-D-20-0097.1, 2020.

Bak, C., Zahle, F., Bitsche, R., Kim, T., Yde, A., Henriksen, L. C., Hansen, M. H., Blasques, J. P. A. A., Gaunaa, M., and Natarajan, A.: The DTU 10-MW reference wind turbine, in: Danish wind power research 2013, https://orbit.dtu.dk/en/publications/the-dtu-10-mw-reference-wind-turbine (last access: 6 May 2022), 2013.

Bento, N. and Fontes, M.: Emergence of floating offshore wind energy: Technology and industry, Renew. Sustain. Energ. Rev., 99, 66–82, https://doi.org/10.1016/j.rser.2018.09.035, 2019.

Borgers, R.: Mesoscale modelling of North Sea wind resources with COSMO-CLM: model evaluation and impact assessment of future wind farm characteristics on cluster-scale wake losses, Zenodo [data set], https://doi.org/10.5281/zenodo.8348700, 2023.

Borrmann, R., Knud, R., Wallasch, A.-K., and Lüers, S.: Capacity densities of European offshore wind

farms, Tech. rep., no. SP18004A1, Deutsche WindGuard GmbH, Varel, Germany, https://vasab.org/document/capacity-densities-of-european-offshore-wind-farms/ (last access: 2 February 2022), 2018.

Bourassa, M. A., Meissner, T., Cerovecki, I., Chang, P. S., Dong, X., De Chiara, G., Donlon, C., Dukhovskoy, D. S., Elya, J., Fore, A., et al.: Remotely sensed winds and wind stresses for marine forecasting and ocean modeling, Front. Mar. Sci., 6, 443, https://doi.org/10.3389/fmars.2019.00443, 2019.

Brisson, E., Demuzere, M., and Van Lipzig, N.: Modelling strategies for performing convection-permitting climate simulations, Meteorol. Z., 25, 149–163, https://doi.org/10.1127/metz/2015/0598, 2015.

Cañadillas, B., Foreman, R., Barth, V., Siedersleben, S., Lampert, A., Platis, A., Djath, B., Schulz-Stellenfleth, J., Bange, J., Emeis, S., and Neumann, T.: Offshore wind farm wake recovery: Airborne measurements and its representation in engineering models, Wind Energy, 23, 1249–1265, 2020.

Chatterjee, F., Allaerts, D., Blahak, U., Meyers, J., and van Lipzig, N.: Evaluation of a wind-farm parametrization in a regional climate model using large eddy simulations, Q. J. Roy. Meteorol. Soc., 142, 3152–3161, https://doi.org/10.1002/qj.2896, 2016.

Copernicus Marine Service: Global Ocean Daily Gridded Reprocessed L3 Sea Surface Winds from Scatterometer, Copernicus Marine Service [data set], https://doi.org/10.48670/moi-00183, 2022.

Coquilla, R. V., Obermeier, J., and White, B. R.: Calibration procedures and uncertainty in wind power anemometers, Wind Eng., 31, 303–316, https://doi.org/10.1260/030952407783418720, 2007.

Das Bundesamt für Seeschifffahrt und Hydrographie: FINO database, http://fino.bsh.de/ (last access: 10 January 2022), 2022.

Dhirendra, D.: Uncertainty Assessment Fugro OCEANOR SEAWATCH Wind LiDAR Buoy at RWE Meteomast IJmuiden, Tech. rep., ECOFYS, https://offshorewind.rvo.nl/file/download/45051422 (last access: 15 February 2022), 2014.

Dirksen, M., Wijnant, I., Siebesma, P., Baas, P., and Natalie, T.: Validation of wind farm parameterisation in Weather Forecast Model HARMONIE-AROME – Analysis of 2019, Tech. rep., WINS50 report, TU Delft, https://www.wins50.nl/downloads/dirksen_etal_validationreport.pdf (last access: 1 September 2022), 2022.

Doms, G. and Baldauf, M.: A description of the nonhydrostatic regional COSMO-Model Part I: dynamics and numerics, Tech. rep., COSMO documentation, Deutscher Wetterdienst, https://doi.org/10.5676/DWD_pub/nwv/cosmo-doc_5.00_I, 2013.

Doms, G., Förstner, J., Heise, E., Herzog, H.-J., Mironov, D., Raschendorfer, M., Reinhardt, T., Ritter, B., Schrodin, R., Schulz, J.-P., and Vogel, P.: A description of the nonhydrostatic regional COSMO-Model Part II: physical parametrization, Tech. rep., COSMO documentation, Deutscher Wetterdienst, https://doi.org/10.5676/DWD_pub/nwv/cosmo-doc_5.00_II, 2013.

Duncan, J., Wijnant, I., and Knoop, S.: DOWA validation against offshore mast and LiDAR measurements, Tech. rep., TNO report 2019 R10062, KNMI – Royal Netherlands Meteorological Institute, https://www.dutchoffshorewindatlas.nl/binaries/dowa/ (last access: 1 September 2021), 2019.

EMODnet: Wind Farms (Polygons), EMODnet Human Activities [data set], https://emodnet.ec.europa.eu/en/human-activities#humanactivities-data-products (last access: 21 January 2022), 2022.

Figa-Saldaña, J., Wilson, J. J., Attema, E., Gelsthorpe, R., Drinkwater, M. R., and Stoffelen, A.: The advanced scatterometer (ASCAT) on the meteorological operational (MetOp) platform: A follow on for European wind scatterometers, Can. J. Remote Sens., 28, 404–412, https://doi.org/10.5589/m02-035, 2002.

Fischereit, J., Brown, R., Larsén, X. G., Badger, J., and Hawkes, G.: Review of mesoscale wind-farm parametrizations and their applications, Bound.-Lay. Meteorol., 182, 175–224, https://doi.org/10.1007/s10546-021-00652-y, 2022a.

Fischereit, J., Larsén, X. G., and Hahmann, A. N.: Climatic Impacts of Wind-Wave-Wake Interactions in Offshore Wind Farms, Front. Energ. Res., 10, 881459, https://doi.org/10.3389/fenrg.2022.881459, 2022b.

Fischereit, J., Schaldemose Hansen, K., Larsén, X. G., van der Laan, M. P., Réthoré, P.-E., and Murcia Leon, J. P.: Comparing and validating intra-farm and farm-to-farm wakes across different mesoscale and high-resolution wake models, Wind Energ. Sci., 7, 1069–1091, https://doi.org/10.5194/wes-7-1069-2022, 2022c.

Fitch, A. C., Olson, J. B., Lundquist, J. K., Dudhia, J., Gupta, A. K., Michalakes, J., and Barstad, I.: Local and mesoscale impacts of wind farms as parameterized in a mesoscale NWP model, Mon. Weather Rev., 140, 3017–3038, https://doi.org/10.1175/MWR-D-11-00352.1, 2012.

Friis Pedersen, T., Dahlberg, J.-Å., and Busche, P.: ACCUWIND – Classification of five cup anemometers according to IEC 61400-12-1, no. 1556(EN) in Denmark, Forskningscenter Risoe, Risoe-R, ISBN 87-550-3516-7, 2006.

Gaertner, E., Rinker, J., Sethuraman, L., Zahle, F., Anderson, B., Barter, G. E., Abbas, N. J., Meng, F., Bortolotti, P., Skrzypinski, W., Scott, G., Feil, R., Bredmose, H., Dykes, K., Shields, M., Allen, C., and Viselli, A.: IEA wind TCP task 37: definition of the IEA 15-megawatt offshore reference wind turbine, Tech. rep., no. NREL/TP-5000-75698, NREL – National Renewable Energy Lab., Golden, CO, USA, https://doi.org/10.2172/1603478, 2020.

Garcia-Santiago, O. M., Badger, J., Hahmann, A. N., and da Costa, G. L.: Evaluation of two mesoscale wind farm parametrisations with offshore tall masts, J. Phys.: Conf. Ser., 2265, 022038, https://doi.org/10.1088/1742-6596/2265/2/022038, 2022.

Gelsthorpe, R., Schied, E., and Wilson, J.: ASCAT-Metop's advanced scatterometer, ESA Bulletin, 102, 19–27, 2000.

Geyer, B., Weisse, R., Bisling, P., and Winterfeldt, J.: Climatology of North Sea wind energy derived from a model hindcast for 1958–2012, J. Wind Eng. Indust. Aerodynam., 147, 18–29, https://doi.org/10.1016/j.jweia.2015.09.005, 2015.

Grachev, A. A., Andreas, E. L., Fairall, C. W., Guest, P. S., and Persson, P. O. G.: The critical Richardson number and limits of applicability of local similarity theory in the stable boundary layer, Bound.-Lay. Meteorol., 147, 51–82, https://doi.org/10.1007/s10546-012-9771-0, 2013.

Gupta, T. and Baidya Roy, S.: Recovery processes in a large offshore wind farm, Wind Energ. Sci., 6, 1089–1106, https://doi.org/10.5194/wes-6-1089-2021, 2021.

Hahmann, A. N., Vincent, C. L., Peña, A., Lange, J., and Hasager, C. B.: Wind climate estimation using WRF model output:

method and model sensitivities over the sea, Int. J. Climatol., 35, 3422–3439, https://doi.org/10.1002/joc.4217, 2015.

Hersbach, H., Bell, B., Berrisford, P., Hirahara, S., Horányi, A., Muñoz-Sabater, J., Nicolas, J., Peubey, C., Radu, R., Schepers, D., Simmons, A., Soci, C., Abdalla, S., Abellan, X., Balsamo, G., Bechtold, P., Biavati, G., Bidlot, J., Bonavita, M., De Chiara, G.,Dahlgren, P., Dee, D., Diamantakis, M., Dragani, R., Flemming, J., Forbes, R., Fuentes, M., Geer, Al., Haimberger, L., Healy, S., Hogan, R. J., Hólm, E., Janisková, M., Keeley, S., Laloyaux, P., Lopez, P., Lupu, C., Radnoti, G., de Rosnay, P., Rozum, I., Vamborg, F., Villaume, S., and Thépaut, J.-N.: The ERA5 global reanalysis, Q. J. Roy. Meteorol. Soci., 146, 1999–2049, https://doi.org/10.1002/qj.3803, 2020.

Hersbach, H., Bell, B., Berrisford, P., Hirahara, S., Horányi, A., Muñoz-Sabater, J., Nicolas, J., Peubey, C., Radu, R., Schepers, D., Simmons, A., Soci, C., Abdalla, S., Abellan, X., Balsamo, G., Bechtold, P., Biavati, G., Bidlot, J., Bonavita, M., De Chiara, G., Dahlgren, P., Dee, D., Diamantakis, M., Dragani, R., Flemming, J., Forbes, R., Fuentes, M., Geer, A., Haimberger, L., Healy, S., Hogan, R. J., Hólm, E., Janisková, M., Keeley, S., Laloyaux, P., Lopez, P., Lupu, C., Radnoti, G., de Rosnay, P., Rozum, I., Vamborg, F., Villaume, S., and Thépaut, J.-N.: ERA5 monthly averaged data on single levels from 1940 to present, Copernicus Climate Change Service (C3S) Climate Data Store (CDS) [data set], https://doi.org/10.24381/cds.adbb2d47, 2022.

IPCC: Summary for Policymakers, in: Climate Change 2022: Mitigation of Climate Change, Contribution of Working Group III to the Sixth Assessment Report of the Intergovernmental Panel on Climate Change, edited by: Shukla, P., Skea, J., Slade, R., Khourdajie, A. A., van Diemen, R., McCollum, D., Pathak, M., Some, S., Vyas, P., Fradera, R., Belkacemi, M., Hasija, A., Lisboa, G., Luz, S., and Malley, J., Cambridge University Press, Cambridge, UK and New York, NY, USA, https://doi.org/10.1017/9781009157926.001, 2022.

Jonkman, J., Butterfield, S., Musial, W., and Scott, G.: Definition of a 5-MW reference wind turbine for offshore system development, Tech. rep., no. NREL/TP-500-38060, NREL – National Renewable Energy Lab., Golden, CO, USA, https://doi.org/10.2172/947422, 2009.

Knoop, S., Bosveld, F. C., de Haij, M. J., and Apituley, A.: A 2-year intercomparison of continuous-wave focusing wind lidar and tall mast wind measurements at Cabauw, Atmos. Meas. Tech., 14, 2219–2235, https://doi.org/10.5194/amt-14-2219-2021, 2021.

Komusanac, I., Brindley, G., Fraile, D., and Ramirez, L.: Wind energy in Europe: 2020 Statistics and the outlook for 2021–2025, Tech. rep., WindEurope, Brussels, Belgium, https://windeurope.org/intelligence-platform/product/wind-energy-in-europe-2020-statistics-and-the-outlook-for-2021 (last access: 10 January 2022), 2020.

Komusanac, I., Brindley, G., Fraile, D., and Ramirez, L.: Wind energy in Europe: 2021 Statistics and the outlook for 2022–2026, Tech. rep., WindEurope, Brussels, Belgium, https://windeurope.org/intelligence-platform/product/wind-energy-in-europe-2021-statistics-and-the-outlook-for-2022 (last access: 10 January 2022), 2021.

Koninklijk Nederlands Meteorologisch Instituut: KNMI data platform, https://dataplatform.knmi.nl/group/wind (last access: 25 February 2022), 2022.

Larsén, X. G. and Fischereit, J.: A case study of wind farm effects using two wake parameterizations in the Weather Research and Forecasting (WRF) model (V3. 7.1) in the presence of low-level jets, Geosci. Model Dev., 14, 3141–3158, https://doi.org/10.5194/gmd-14-3141-2021, 2021.

Leiding, T., Tinz, B., Gates, L., Rosenhagen, G., Herklotz, K., and Senet, C.: Standardisierung und vergleichende Analyse der meteorologischen FINO-Messdaten (FINO123): Forschungsvorhaben FINO-Wind: Abschlussbericht: 12/2012–04/2016, Deutscher Wetterdienst, https://www.dwd.de/DE/klimaumwelt/klimaforschung/klimaueberwachung/finowind/finodoku/abschlussbericht_pdf.pdf?__blob=publicationFile&v=3 (last access: 1 October 2021), 2016.

Li, D., Geyer, B., and Bisling, P.: A model-based climatology analysis of wind power resources at 100-m height over the Bohai Sea and the Yellow Sea, Appl. Energy, 179, 575–589, https://doi.org/10.1016/j.apenergy.2016.07.010, 2016.

Lu, H. and Porté-Agel, F.: On the impact of wind farms on a convective atmospheric boundary layer, Bound.-Lay. Meteorol., 157, 81–96, 2015.

Lundquist, J. K., DuVivier, K. K., Kaffine, D., and Tomaszewski, J. M.: Costs and consequences of wind turbine wake effects arising from uncoordinated wind energy development, Nat. Energy, 4, 26–34, https://doi.org/10.1038/s41560-018-0281-2, 2019.

Matte, D., Laprise, R., Thériault, J. M., and Lucas-Picher, P.: Spatial spin-up of fine scales in a regional climate model simulation driven by low-resolution boundary conditions, Clim. Dynam., 49, 563–574, 2017.

Matthijsen, J., Dammers, E., and Elzenga, H.: De toekomst van de Noordzee: de Noordzee in 2030 en 2050: een scenariostudie, Planbureau voor de Leefomgeving, https://www.pbl.nl/sites/default/files/downloads/pbl-2018-toekomst-van-de-noordzee-2728.pdf (last access: 1 July 2021), 2018.

Meetnet Vlaamse Banken: Data of the Flemish Banks Monitoring Network, https://meetnetvlaamsebanken.be/Download/Welcome (last access: 25 February 2022), 2022.

Mellor, G. L. and Yamada, T.: Development of a turbulence closure model for geophysical fluid problems, Rev. Geophys., 20, 851–875, https://doi.org/10.1029/RG020i004p00851, 1982.

Menezes, D., Mendes, M., Almeida, J. A., and Farinha, T.: Wind farm and resource datasets: A comprehensive survey and overview, Energies, 13, 4702, https://doi.org/10.3390/en13184702, 2020.

Meyers, J. and Meneveau, C.: Optimal turbine spacing in fully developed wind farm boundary layers, Wind Energy, 15, 305–317, https://doi.org/10.1002/we.469, 2012.

Munters, W., Adiloglu, B., Buckingham, S., and van Beeck, J.: Wake impact of constructing a new offshore wind farm zone on an existing downwind cluster: a case study of the Belgian Princess Elisabeth zone using FLORIS, J. Phys.: Conf. Ser., 2265, 022049, https://doi.org/10.1088/1742-6596/2265/2/022049, 2022.

Musial, W., Spitsen, P., Duffy, P., Beiter, P., Marquis, M., Hammond, R., and Shields, M.: Offshore Wind Market Report: 2022 Edition, Tech. rep., no. NREL/TP-5000-83544, NREL – National Renewable Energy Lab., Golden, CO, USA, https://doi.org/10.2172/1883382, 2022.

Nederlandse Organisatie voor toegepast-natuurwetenschappelijk onderzoek: Nimbus, https://nimbus.windopzee.net/ (last access: 15 February 2022), 2022.

Nolan, P., Lynch, P., and Sweeney, C.: Simulating the future wind energy resource of Ireland using the COSMO-CLM model, Wind Energy, 17, 19–37, https://doi.org/10.1002/we.1554, 2014.

Platis, A., Siedersleben, S. K., Bange, J., Lampert, A., Bärfuss, K., Hankers, R., Cañadillas, B., Foreman, R., Schulz-Stellenfleth, J., Djath, B., Neumann, T., and Emeis, S.: First in situ evidence of wakes in the far field behind offshore wind farms, Sci. Rep., 8, 2163, https://doi.org/10.1038/s41598-018-20389-y, 2018.

Platis, A., Hundhausen, M., Lampert, A., Emeis, S., and Bange, J.: The role of atmospheric stability and turbulence in offshore wind-farm wakes in the German bight, Bound.-Lay. Meteorol., 182, 441–469, https://doi.org/10.1007/s10546-021-00668-4, 2021.

Porté-Agel, F., Lu, H., and Wu, Y.-T.: Interaction between large wind farms and the atmospheric boundary layer, Procedia Iutam, 10, 307–318, 2014.

Poveda, J. M. and Wouters, D. A. J.: Wind measurements at meteorological mast IJmuiden, Tech. rep., eCN-E–14-058, ECN, https://publicaties.ecn.nl/PdfFetch.aspx?nr=ECN-E--14-058 (last access: 19 January 2022), 2015.

Pryor, S. C., Barthelmie, R. J., and Shepherd, T. J.: Wind power production from very large offshore wind farms, Joule, 5, 2663–2686, https://doi.org/10.1016/j.joule.2021.09.002, 2021.

Rabin, J., Delon, J., and Gousseau, Y.: Circular Earth Mover's Distance for the comparison of local features, in: 2008 19th International Conference on Pattern Recognition, 8–11 December 2008, Tampa, USA, https://doi.org/10.1109/ICPR.2008.4761372, 2008.

Raschendorfer, M.: The new turbulence parameterization of LM, Tech. rep., COSMO newsletter, Deutscher Wetterdienst, http://www.cosmo-model.org/content/model/documentation/newsLetters/newsLetter01/newsLetter_01.pdf (last access: 22 May 2021), 2001.

Reyers, M., Pinto, J. G., and Moemken, J.: Statistical–dynamical downscaling for wind energy potentials: evaluation and applications to decadal hindcasts and climate change projections, Int. J. Climatol., 35, 229–244, https://doi.org/10.1002/joc.3975, 2015.

Reyers, M., Moemken, J., and Pinto, J. G.: Future changes of wind energy potentials over Europe in a large CMIP5 multi-model ensemble, Int. J. Climatol., 36, 783–796, https://doi.org/10.1002/joc.4382, 2016.

Rijksdienst voor Ondernemend Nederland: Offshorewind RVO, https://offshorewind.rvo.nl/ (last access: 15 February 2022), 2022.

Rockel, B., Will, A., and Hense, A.: The regional climate model COSMO-CLM (CCLM), Meteorol. Z., 17, 347–348, https://doi.org/10.1127/0941-2948/2008/0309, 2008.

Ronda, R., Wijnant, I., and Stepek, A.: Inter-annual wind speed variability on the North Sea, Tech. rep., TR-360, KNMI – Royal Netherlands Meteorological Institute, https://cdn.knmi.nl/knmi/pdf/bibliotheek/knmipubTR/TR360.pdf (last access: 5 April 2021), 2017.

Santos, J., Rochinha, C., Liberato, M., Reyers, M., and Pinto, J.: Projected changes in wind energy potentials over Iberia, Renew. Energy, 75, 68–80, https://doi.org/10.1016/j.renene.2014.09.026, 2015.

Sathe, A., Gryning, S.-E., and Peña, A.: Comparison of the atmospheric stability and wind profiles at two wind farm sites over a long marine fetch in the North Sea, Wind Energy, 14, 767–780, https://doi.org/10.1002/we.456, 2011.

Schneemann, J., Rott, A., Dörenkämper, M., Steinfeld, G., and Kühn, M.: Cluster wakes impact on a far-distant offshore wind farm's power, Wind Energ. Sci., 5, 29–49, https://doi.org/10.5194/wes-5-29-2020, 2020.

Sheridan, L. M., Krishnamurthy, R., and Gaudet, B. J.: Assessment of model hub height wind speed performance using DOE lidar buoy data, Tech. rep., pNNL-30840, PNNL – Pacific Northwest National Lab., Richland, WA, USA, https://doi.org/10.2172/1779495, 2021.

Shields, M., Beiter, P., Nunemaker, J., Cooperman, A., and Duffy, P.: Impacts of turbine and plant upsizing on the levelized cost of energy for offshore wind, Appl. Energy, 298, 117189, https://doi.org/10.1016/j.apenergy.2021.117189, 2021.

Siedersleben, S. K., Platis, A., Lundquist, J. K., Djath, B., Lampert, A., Bärfuss, K., Cañadillas, B., Schulz-Stellenfleth, J., Bange, J., Neumann, T., and Emeis, S.: Turbulent kinetic energy over large offshore wind farms observed and simulated by the mesoscale model WRF (3.8.1), Geosci. Model Dev., 13, 249–268, https://doi.org/10.5194/gmd-13-249-2020, 2020.

Stevens, R. J., Gayme, D. F., and Meneveau, C.: Effects of turbine spacing on the power output of extended wind-farms, Wind Energy, 19, 359–370, https://doi.org/10.1002/we.1835, 2016.

Stull, R. B.: An introduction to boundary layer meteorology, in: vol. 13, Springer Science & Business Media, https://doi.org/10.1007/978-94-009-3027-8, 1988.

Tammelin, B., Vihma, T., Atlaskin, E., Badger, J., Fortelius, C., Gregow, H., Horttanainen, M., Hyvönen, R., Kilpinen, J., Latikka, J., Ljungberg, K., Mortensen, N. G., Niemelä, S., Ruosteenoja, K., Salonen, K., Suomi, I., and Venäläinen, A.: Production of the Finnish wind atlas, Wind Energy, 16, 19–35, https://doi.org/10.1002/we.517, 2013.

The Crown Estate: Marine Data Exchange, https://www.marinedataexchange.co.uk (last access: 22 March 2022), 2022.

Tiedtke, M.: A comprehensive mass flux scheme for cumulus parameterization in large-scale models, Monthly weather review, 117, 1779–1800, https://doi.org/10.1175/1520-0493(1989)117<1779:ACMFSF>2.0.CO;2, 1989.

van Stratum, B., Theeuwes, N., Barkmeijer, J., van Ulft, B., and Wijnant, I.: A One-Year-Long Evaluation of a Wind-Farm Parameterization in HARMONIE-AROME, J. Adv. Model. Earth Syst., 14, e2021MS002947, https://doi.org/10.1029/2021MS002947, 2022.

Vergara-Temprado, J., Ban, N., Panosetti, D., Schlemmer, L., and Schär, C.: Climate models permit convection at much coarser resolutions than previously considered, J. Climate, 33, 1915–1933, https://doi.org/10.1175/JCLI-D-19-0286.1, 2020.

Verhoef, A. and Stoffelen, A.: Validation of ASCAT 12.5-km winds, Tech. rep., reference: SAF/OSI/CDOP/KNMI/TEC/RP/147, https://knmi-scatterometer-website-prd.s3-eu-west-1.amazonaws.com/publications/validation_of_ascat_12.5km_winds_1.3.pdf (last access: 6 May 2021),, 2009.

Verkaik, J.: Documentatie Windmetingen In Nederland (in Dutch), Tech. rep., KNMI – Royal Netherlands Meteorological Institute – klimatologische dienst, https:

//www.researchgate.net/publication/266441846_Documentatie_Windmetingen_In_Nederland (last access: 6 June 2021), 2001.

Vigin, L.: shapefiles of the Belgian and Dunkirk offshore zones, RBINS – Royal Belgian Institute of Natural Science, https://www.bmdc.be/NODC/index.xhtml (last access: 19 January 2022), 2022.

Volker, P. J., Hahmann, A. N., Badger, J., and Jørgensen, H. E.: Prospects for generating electricity by large onshore and offshore wind farms, Environ. Res. Lett., 12, 034022, https://doi.org/10.1088/1748-9326/aa5d86, 2017.

Werkhoven, E. and Verhoef, J.: Offshore Meteorological Mast IJmuiden – Abstract of Instrumentation Report, Tech. rep., ECN-Wind Memo-12-010, Ministry of Economic Affairs, Agriculture and Innovation of The Netherlands, https://offshorewind-measurements.tno.nl/ (last access: 26 March 2022), 2012.

Westerhellweg, A., Neumann, T., and Riedel, V.: FINO1 mast correction, Vol. 21, DEWI-Magazin, 2012.

Wijnant, I., van den Brink, H., and Stepek, A.: North Sea wind climatology Part 1: a review of existing wind atlases, Tech. rep., technical report TR-342, KNMI – Royal Netherlands Meteorological Institute, https://cdn.knmi.nl/knmi/pdf/bibliotheek/knmipubTR/TR342.pdf (last access: 30 March 2021), 2014.

Wouters, D. and Verhoef, J.: Verification of Leosphere Windcube WLS7-577 at ECN part of TNO LiDAR Calibration Facility, for offshore measurements at Lichteiland Goeree, Tech. rep., TNO 2019 R10398, ECN, https://offshorewind-measurements.tno.nl/ (last access: 21 May 2021), 2019a.

Wouters, D. and Verhoef, J.: Verification of ZephIR 300 unit 315 at ECN part of TNO LiDAR Calibration Facility, for offshore measurements at Euro Platform, Tech. rep., TNO 2018 R10762, ECN, https://offshorewind-measurements.tno.nl/ (last access: 21 May 2021), 2019b.

Wouters, D. and Verhoef, J.: Verification of ZephIR 300 unit 563 at ECN part of TNO LiDAR Calibration Facility, for offshore measurements at K13-A production platform, Tech. rep., TNO 2018 R10850, ECN, https://offshorewind-measurements.tno.nl/ (last access: 21 May 2021), 2019c.